(4)

David Taylor Research Center

Bethesda, MD 20084–5000

Magnetohydrodynamic Liquid-Metal Flows in a Rectangular Channel with an Axial Magnetic Field, a Moving Conducting Wall and Free Surfaces

by
Gita Talmage and John S. Walker
University of Illinois at Urbana-Champaign
Urbana, Illinois

Samuel H. Brown and Neal A. Sondergaard
David Taylor Research Center
Annapolis, Maryland

Patricia E. Burt
United States Naval Academy
Annapolis, Maryland

DTIC
ELECTE
JAN 0 3 1990
S D

90 01 02 117

MAJOR DTRC TECHNICAL COMPONENTS

CODE 011 DIRECTOR OF TECHNOLOGY, PLANS AND ASSESSMENT

      12 SHIP SYSTEMS INTEGRATION DEPARTMENT

      14 SHIP ELECTROMAGNETIC SIGNATURES DEPARTMENT

      15 SHIP HYDROMECHANICS DEPARTMENT

      16 AVIATION DEPARTMENT

      17 SHIP STRUCTURES AND PROTECTION DEPARTMENT

      18 COMPUTATION, MATHEMATICS & LOGISTICS DEPARTMENT

      19 SHIP ACOUSTICS DEPARTMENT

      27 PROPULSION AND AUXILIARY SYSTEMS DEPARTMENT

      28 SHIP MATERIALS ENGINEERING DEPARTMENT

REPORT DOCUMENTATION PAGE

1a. REPORT SECURITY CLASSIFICATION				1b. RESTRICTIVE MARKINGS			
Unclassified							

2a. SECURITY CLASSIFICATION AUTHORITY	3. DISTRIBUTION/AVAILABILITY OF REPORT
	Approved for public release; distribution unlimited.
2b. DECLASSIFICATION/DOWNGRADING SCHEDULE	

4. PERFORMING ORGANIZATION REPORT NUMBER(S)	5. MONITORING ORGANIZATION REPORT NUMBER(S)
DTRC–89/019	

6a. NAME OF PERFORMING ORGANIZATION	6b. OFFICE SYMBOL (If applicable)	7a. NAME OF MONITORING ORGANIZATION
David Taylor Research Center	2712	

6c. ADDRESS (City, State, and ZIP Code)	7b. ADDRESS (City, State, and ZIP Code)
Bethesda, MD 20084–5067	

8a. NAME OF FUNDING/SPONSORING ORGANIZATION	8b. OFFICE SYMBOL (If applicable)	9. PROCUREMENT INSTRUMENT IDENTIFICATION NUMBER
Defense Nuclear Agency		

8c. ADDRESS (City, State, and ZIP Code)	10. SOURCE OF FUNDING NUMBERS			
	PROGRAM ELEMENT NO	PROJECT NO.	TASK NO	WORK UNIT ACCESSION NO
Washington, D.C. 20305–1000	63224C			1–1712–501

11. TITLE (Include Security Classification)
Magnetohydrodynamic Liquid-Metal Flows in a Rectangular Channel with an Axial Magnetic Field, a Moving Conducting Wall and Free Surfaces

12. PERSONAL AUTHOR(S)
Gita Talmage, John S. Walker, Samuel H. Brown, Neal A. Sondergaard, and Patricia E. Burt

13a. TYPE OF REPORT	13b. TIME COVERED	14. DATE OF REPORT (YEAR, MONTH, DAY)	15. PAGE COUNT
Final	FROM____ TO____	1989 November	71

16. SUPPLEMENTARY NOTATION
This work was performed in conjunction with the University of Illinois at Urbana-Champaign, Urbana, Illinois 61801

17.	COSATI CODES		18. SUBJECT TERMS (Continue on reverse if necessary and identify by block number)
FIELD	GROUP	SUB-GROUP	Liquid-metal flows; Magnetohydrodynamics; Rectangular channel; Moving wall; Magnetic induction .

19. ABSTRACT (Continue on reverse if necessary and identify by block number)

Fully developed, viscous liquid-metal velocity profiles and induced magnetic field contours were studied for Hartmann number of $M=2$ and 10 and for different load currents for a particular rectangular channel configuration (two-dimensional Couette flow). The rectangular channel was assumed to have a homogeneous external (axial) magnetic field parallel to the moving, perfectly conducting top wall and the stationary, perfectly conducting bottom wall. The two stationary side walls were also perfect conductors. The small gap between the moving wall and each side wall was an insulating, free surface. The method of weighted residuals was used to obtain truncated series solutions for the variables of interest. The heavy load currents across the channel were obtained by simulating an external potential to the conducting moving wall. The load currents in each case were opposed by the induced electric field. Since there is no pressure gradient, the flow along the channel is driven by the viscous effects of the moving wall and the Lorentz body force and is retarded by the stationary walls. In the case where no load current is applied across the channel, the current circulates in the channel. The circulation is driven by the generator that is due to the axial variation of velocity in an axial magnetic field.
(continued on reverse side)

20. DISTRIBUTION/AVAILABILITY OF ABSTRACT	21. ABSTRACT SECURITY CLASSIFICATION
☐ UNCLASSIFIED/UNLIMITED ☒ SAME AS RPT ☐ DTIC USERS	Unclassified

22a. NAME OF RESPONSIBLE INDIVIDUAL	22b. TELEPHONE (Include Area Code)	22c. OFFICE SYMBOL
Samuel H. Brown	(301)267-3458	Code 2712

Block 19 (continued)

The numerical data presented show that the radial gap and the free surface region represent electrical resistances in parallel between the perfectly conducting stationary wall and the perfectly conducting moving wall. The data also show that the resistance of the radial gap increases as M^2 while that of the free surface increases by M or $M^{1/2}$. Thus, as M increases, the division of current shifts to the free surface region and the current density in the radial gap decreases as M^{-1}. The theoretical magnetohydrodynamic model presented here was developed to provide data to help in the design of liquid-metal current collectors.

Data were computed for one-dimensional Couette flow with no pressure gradient in an external, homogeneous axial magnetic field. One-dimensional Couette flow has no end effects, and thus the data were compared with corresponding data for the two-dimensional Couette flow case to determine end effects. /

Accession For

NTIS CRA&I	☑
DTIC TAB	☐
Unannounced	☐
Justification	

By
Distribution /

Availability Codes

| Dist | Avail and/or Special |

A-1

CONTENTS

FIGURES

TABLES

NOMENCLATURE

$a = 3$ Nondimensional rectangular channel free surface length (see Fig. 2). Dimensional length equals $3L$.

$b = 10$ Half length of the nondimensional rectangular channel's perfectly conducting, moving wall (see Fig. 2). Dimensional length equals $10L$.

h Nondimensional current density stream function or induced magnetic field (see Eqs. 4.1 and 4.2)

$(*)$ A superscript $*$ on a variable denotes a dimensional quantity.

I^* Total dimensional load current across the channel

h_0 Nondimensional parameter representing the total dimensional current current I^* where $I^* = 2h_o U_o (\sigma M)^{1/2} (\Delta x^*)$.

$\vec{j}$ Nondimensional current density vector $= \dfrac{\vec{j}^*}{\sigma U_o B_o}$.

L Dimensional height of channel.

P Nondimensional pressure (scalar) $= \dfrac{P^*}{\sigma U_o B_o^2 L}$.

$\vec{V}$ Nondimensional fluid velocity $= \dfrac{\vec{V}^*}{U_o}$.

u x–component of nondimensional velocity.

j_y, j_z Nondimensional electric current density components in the y- and z-directions, respectively.

ϕ Nondimensional electric potential $= \dfrac{\phi^*}{U_o B_o L}$.

ϕ_0 Nondimensional electric potential between moving and stationary wall of rectangular channel.

$\vec{\nabla}$ Nondimensional gradient (vector) $= L \vec{\nabla}^*$.

(x^*, y^*, z^*) Dimensional Cartesian coordinates.

(x, y, z) Nondimensional Cartesian coordinates $= \left(\dfrac{x^*}{L}, \dfrac{y^*}{L}, \dfrac{z^*}{L} \right)$, (see Fig. 2).

$(\hat{x}, \hat{y}, \hat{z})$ Unit vectors in Cartesian coordinates (see Fig. 2).

Δx^* Dimensional length along rectangular channel $= L(\Delta x)$.

$\vec{B}_o$ Dimensional external, homogeneous, magnetic field $= B_o \hat{z}$.

σ Fluid electric conductivity.

ρ Fluid density.

μ_f Fluid viscosity.

N Interaction number, a nondimensional parameter $= \dfrac{\sigma B_o^2 L}{\rho U_o} =$ ratio of pondermotive force to inertial force.

M Hartmann number, a nondimensional parameter $= LB_o\sqrt{\dfrac{\sigma}{\mu_f}} =$ positive square root of the ratio of the pondermotive force to the viscous force.

R_m Magnetic Reynolds number, a nondimensional parameter $= U_o\,\sigma\mu L =$ ratio of induced magnetic field to external magnetic field.

U_o Dimensional velocity of perfectly conducting, moving wall of rectangular channel.

E Integral expression defined as a residual (see Eq. 18).

P_j Total nondimensional Joulean dissipation per unit nondimensional length in rectangular channel (see Eq. 24), $(P_j{}^* = \mu_f U_o{}^2 P_J)$

P_μ Total nondimensional viscous dissipation per unit nondimensional length in rectangular channel (see Eq. 23), $(P_\mu{}^* = \mu_f U_o{}^2 P_\mu)$

$(1D)$ A subscript $1D$ on a variable denotes the one-dimensional Couette problem. All variables without the subscript $1D$ denote the two-dimensional Couette problem (see section entitled "Comparison of Numerical Parameters for One-dimensional and Two-dimensional Flow").

ABSTRACT

Fully developed, viscous liquid-metal velocity profiles and induced magnetic field contours were studied for Hartmann numbers of M=2 and 10 and for different load currents for a particular rectangular channel configuration (two-dimensional Couette flow). The rectangular channel was assumed to have a homogeneous external (axial) magnetic field parallel to the moving, perfectly conducting top wall and the stationary, perfectly conducting bottom wall. The two stationary side walls were also perfect conductors. The small gap between the moving wall and each side wall was an insulating, free surface. The method of weighted residuals was used to obtain truncated series solutions for the variables of interest. The heavy load currents across the channel were obtained by simulating an external potential to the conducting moving wall. The load currents in each case were opposed by the induced electric field. Since there is no pressure gradient, the flow along the channel is driven by the viscous effects of the moving wall and the Lorentz body force and is retarded by the stationary walls. In the case where no load current is applied across the channel, the current circulates in the channel. The circulation is driven by the generator that is due to the axial variation of velocity in an axial magnetic field.

The numerical data presented show that the radial gap and the free surface region represent electrical resistances in parallel between the perfectly conducting stationary wall and the perfectly conducting moving wall. The data also show that the resistance of the radial gap increases as M^2 while that of the free surface increases by M or $M^{1/2}$. Thus, as M increases, the division of current shifts to the free surface region and the current density in the radial gap decreases as M^{-1}. The theoretical magnetohydrodynamic model presented here was developed to provide data to help in the design of liquid-metal current collectors.

Data were computed for one-dimensional Couette flow with no pressure gradient in an external, homogeneous axial magnetic field. One-dimensional Couette flow has no end effects, and thus the data were compared with corresponding data for the two-dimensional Couette flow case to determine end effects.

ADMINISTRATIVE INFORMATION

1

INTRODUCTION

A critical technology area in the development of homopolar generators and motors[1-6] is the mechanism for transporting current between the rotating and stationary components of the system. This sliding electric contact, or current collector device, must successfully operate in the very high current density, magnetic fields and speed regimes of a homopolar system. In addition, requirements of low power losses and long life time make traditional monolithic brushes, such as metal graphite, unattractive. However, liquid metals can provide all the proper operational characteristics as well as minimizing viscous and electrical power losses and maximizing the system lifetime. For instance, state of the art, continuous duty liquid metal current collectors have successfully transported electric current densities of 3×10^7 amp/m^2 in model devices. Although these results are highly encouraging, implementation in practical systems will require a considerable effort. Therefore, further improvements in current collector design will be guided by a thorough understanding of the fundamental principles of liquid metal flows transporting current in high-magnitude external magnetic fields. To this end, we have defined in this paper a magnetohydrodynamic theoretical problem in an attempt to extract some of the basic physics involved.

In contrast to the many studies[7-9] of fixed-wall magnetohydrodynamic duct flow driven principally by pressure gradients along the duct, previous work by the authors[10-15] has been directed toward solving simple models of collectors as two-dimensional rectangular ducts with moving walls, transport current, and magnetic fields of varying orientation driving the flow.[10-15]

In these studies, there was a velocity discontinuity at the intersection of the moving and fixed walls which, although physically impossible, was mathematically tractible and provided a number of fundamental insights.

The purpose of the present paper is to examine a more physically realistic model, which includes stress-free insulating gaps between the moving and fixed walls. As with the previous models, the moving and fixed conducting walls represent the rotor and stator of a current collector in a homopolar device while the two stress-free surfaces represent the spaces in between the rotor and stator filled with a liquid metal which allows device operation with relatively low friction (see Fig. 2). The problem with the moving perfectly conducting wall with no insulating free surfaces in the corners was worked by the authors and served as a basis for some of the theoretical work herein and is thus presented in Appendix A. The magnetic field is oriented parallel to the moving wall face, a geometry often found to minimize eddy currents in practical homopolar generators. The parameters of variation are applied external magnetic field strength, fluid electrical conductivity, density, viscosity, gap width, rotor axial length, axial gap width, and total current between stator and rotor. Two-dimensional results are presented for a number of cases for channel fluid velocity profile, induced magnetic field in the channel, and Joulean and viscous power losses, and these results are compared with similar one-dimensional solutions. The general analytical solutions for the fluid velocity and current density can serve as benchmarks for various numerical computations of similar problems. The values of parameters chosen for numerical calculations are typical of electrical contact parameters in generators or motors.

STATOR LIQUID METAL

ROTOR

COVER GAS

AXIS OF ROTATION

$\vec{B}_0$ AXIAL MAGNETIC FIELD
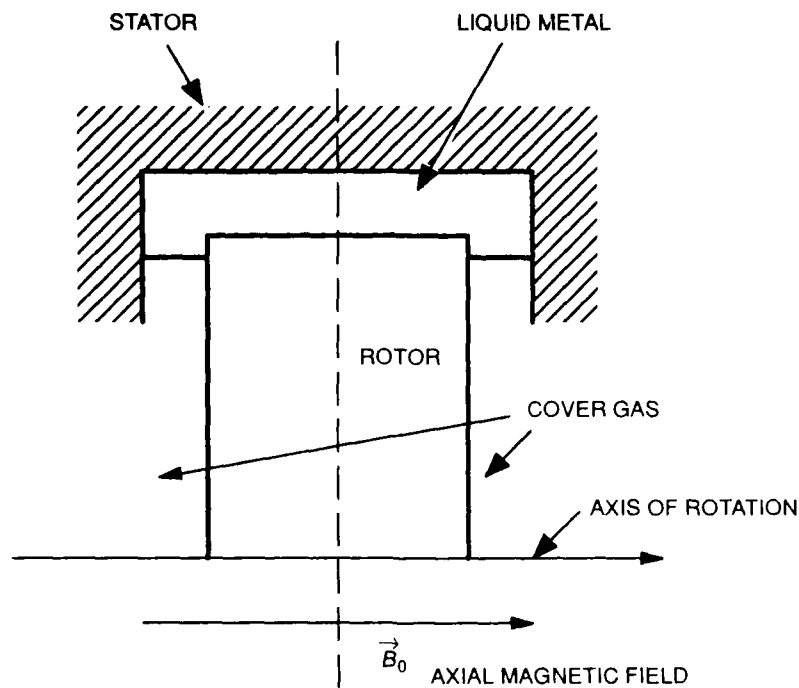
NOTE: TOP HALF OF COLLECTOR SHOWN

Fig. 1. Typical current collector configuration.

y x z

y

$\vec{B}_0$ AXIAL MAGNETIC FIELD

FREE SURFACE   MOVING PERFECT CONDUCTOR   FREE SURFACE $j_y = \dfrac{\partial u}{\partial y} = 0$

$y = L$

b   a

STATIONARY
PERFECT
CONDUCTOR

STATIONARY
PERFECT
CONDUCTORS

$u = 0$
$\varnothing = 0$

$u = 0$
$\varnothing = 0$

$y = 0$

$z = (a+b)L$ $z = 0$

$u = 0$
$\varnothing = 0$

z
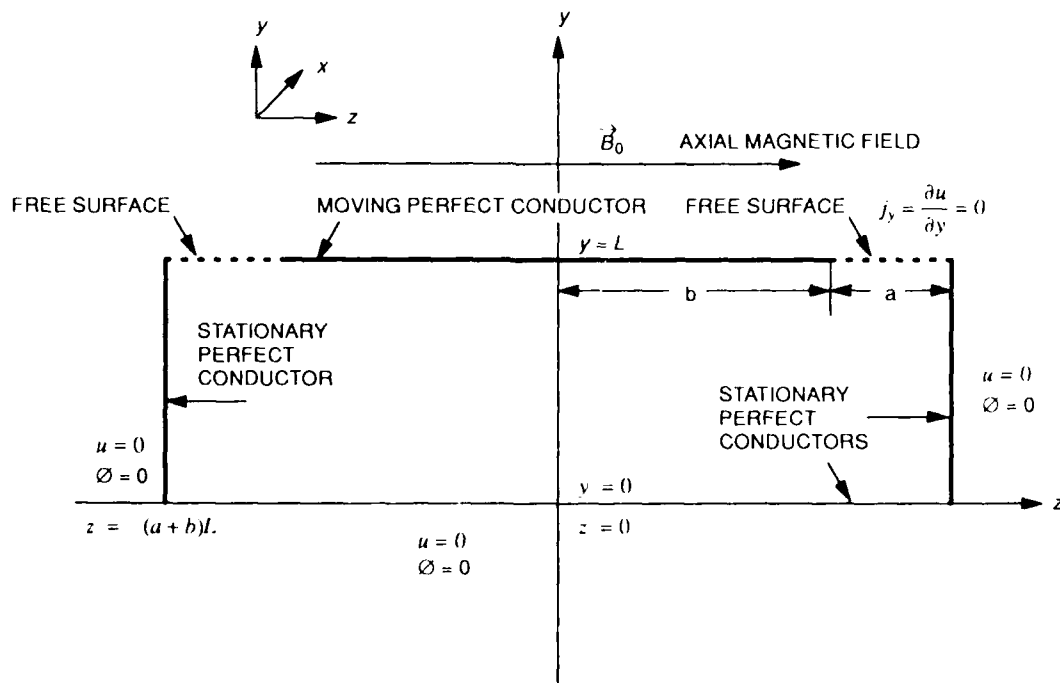
Fig. 2. Rectangular channel cross section.

3

NONDIMENSIONAL MAGNETOHYDRODYNAMICS EQUATIONS

The nondimensional magnetohydrodynamics equations for fully developed, incompressible laminar duct flow in an external axial magnetic field can be expressed[12,13] as

$$N^{-1}\left(\vec{V}\cdot\vec{\nabla}\right)\vec{V} = -\vec{\nabla}P + \vec{j}\times\hat{z} + M^{-2}\nabla^2\vec{V} , \tag{1.1}$$

$$\vec{j} = -\vec{\nabla}\phi + \vec{V}\times\hat{z} , \tag{1.2}$$

$$\vec{\nabla}\cdot\vec{V} = 0 , \tag{1.3}$$

$$\vec{\nabla}\cdot\vec{j} = 0 . \tag{1.4}$$

In Eq. (1.1), $N = \dfrac{\sigma B_o^2 L}{\rho U_o}$ represents the interaction parameter, the ratio of pondermotive

force to inertial force. $M = LB_o\sqrt{\dfrac{\sigma}{\mu_f}}$ is the Hartmann number, the positive square root of

the ratio of the pondermotive force to the viscous force. It is assumed during this work that the magnetic Reynolds number $R_m = U_o\,\sigma\mu L$ (ratio of induced magnetic field to external magnetic field) is much less than one. The nondimensional variables in Eqs. 1.1 to 1.4 are defined as

$\vec{V}$ = fluid velocity normalized by U_o

$$= \frac{\vec{V}^*}{U_o} \tag{2.1}$$

P = pressure normalized by $\sigma U_o B_o^2 L$

$$= \frac{P^*}{\sigma U_o B_o^2 L} \tag{2.2}$$

$\vec{j}$ = electric current density vector normalized by $\sigma U_o B_o$

$$= \frac{\vec{j}^*}{\sigma U_o B_o} \tag{2.3}$$

ϕ = electric potential normalized by $U_o B_o L$

$$= \frac{\phi^*}{U_o B_o L} \tag{2.4}$$

$\vec{\nabla}$ = gradient normalized by L

$$= L\vec{\nabla}^* \tag{2.5}$$

$\hat{x}, \hat{y}, \hat{z}$ = unit vectors in Cartesian coordinates (see Fig. 2). $\tag{2.6}$

The superscript (*) denotes dimensional variables. The x, y, and z coordinates are normalized by L. The magnitude B_o is the externally applied homogeneous magnetic field. U_o is the velocity of a moving wall in the rectangular channel. The variable L is the height of the channel. The characteristic fluid velocity U_o is the velocity of the moving wall in the

rectangular channel. The characteristic length L is the height of the channel. The liquid metal's material constants are electrical conductivity σ, density ρ, magnetic permeability μ and viscosity μ_f.

RECTANGULAR CHANNEL PROBLEM

MATHEMATICAL SOLUTION

The problem discussed in this paper consists of a rectangular channel (see Fig. 3) filled with a liquid metal in a uniform magnetic field B_o in the z-direction. The perfectly conducting top wall is assumed to move with velocity $u = U_o$. The moving wall extends from $z = -b$ to $z = +b$ at $y = 1$. At each top corner there is an insulating free surface in the left corner from $z = -(a + b)$ to $-b$ and in the right corner from $z = +b$ to $z = (a + b)$ at $y = 1$. The perfectly conducting bottom wall is stationary with velocity $u = 0$. The side walls are also perfect conductors with velocity $u = 0$.
The flow is assumed steady, incompressible, fully developed laminar flow in the

x-direction. The pressure gradient $\vec{\nabla}P$ is set equal to zero. Thus, there is no pressure gradient in the x-direction along the channel $\partial P / \partial x = 0$. The magnetic field is uniform and

axial, $\vec{B_o} = B_o \hat{z}$. No assumptions are made about the Hartmann number M. The interaction parameter N is assumed much greater than one in this problem. By symmetry considerations numerical results in the paper will be presented only for the right half channel $0 \le z \le (a + b)$ with $0 \le y \le 1$.

The generalized nondimensional magnetohydrodynamics equations Eqs. 1.1 to 1.4 can be transformed into the following vector component form

$$M^{-2}\left(\frac{\partial^2 u}{\partial y^2} + \frac{\partial^2 u}{\partial z^2}\right) = -j_y \ , \tag{3.1}$$

$$j_y = -\frac{\partial \phi}{\partial y} - u \ , \tag{3.2}$$

$$j_z = -\frac{\partial \phi}{\partial z} \ , \tag{3.3}$$

$$\frac{\partial j_y}{\partial y} + \frac{\partial j_z}{\partial z} = 0 \ . \tag{3.4}$$

Equation 3.1 is the x-component of the Navier Stokes equation. Equations 3.2 and 3.3 are the y- and z-components for the current density Eq. 1.2 and are referred to as Ohm's law. Equation 3.4 comes from Eq. 1.4 and is referred to as the conservation of charge. The continuity equation is automatically satisfied in Eq. 3.1 because the flow is uncompressible $\left(\vec{\nabla} \cdot \vec{u} = 0\right)$
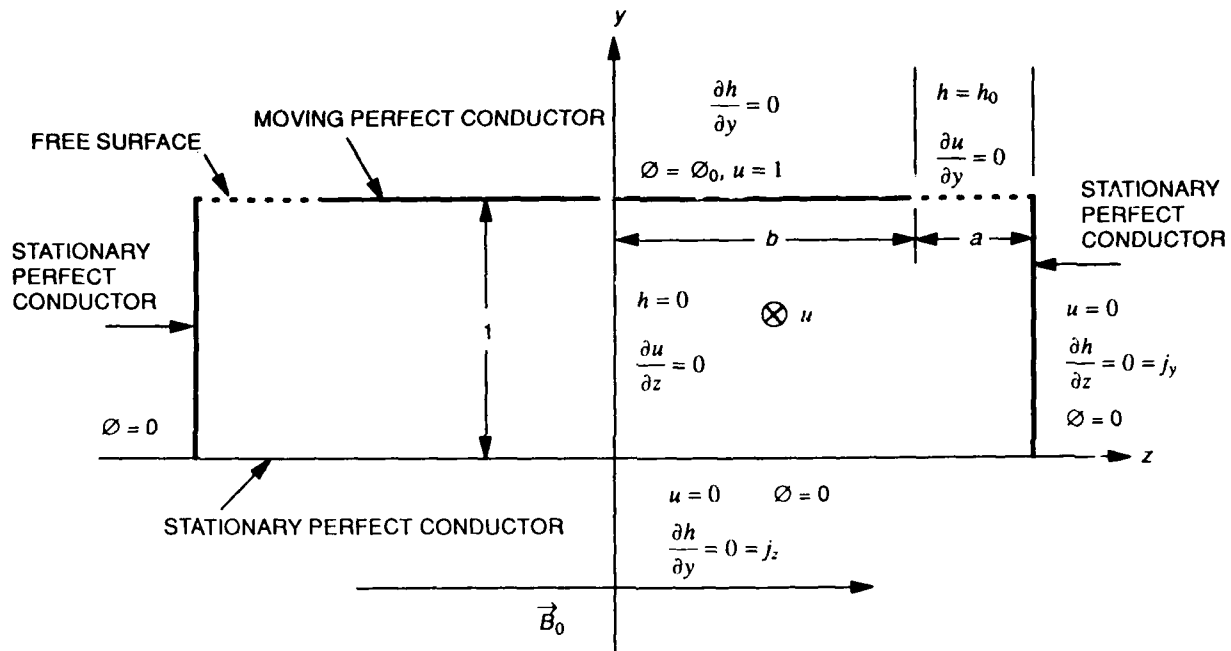
Fig. 3   Rectangular channel with moving wall.

These equations can be cast in terms of the electric current density stream function h, defined by

$$j_y = \frac{1}{M}\frac{\partial h}{\partial z} , \tag{4.1}$$

$$j_z = -\frac{1}{M}\frac{\partial h}{\partial y} . \tag{4.2}$$

Replacing the current densities j_y and j_z in the dimensionless governing equations and eliminating the electric potential ϕ from Ohm's law yields the following set of second-order, homogeneous partial differential equations

$$\frac{1}{M}\left[\frac{\partial^2 u}{\partial y^2} + \frac{\partial^2 u}{\partial z^2}\right] + \frac{\partial h}{\partial z} = 0 \tag{5.1}$$

$$\frac{1}{M}\left[\frac{\partial^2 h}{\partial y^2} + \frac{\partial^2 h}{\partial z^2}\right] + \frac{\partial u}{\partial z} = 0 \tag{5.2}$$

The following boundary conditions must be satisfied by these equations (see Fig. 3). Due to the symmetry of the problem only the right half of the rectangular channel is discussed. The same boundary conditions apply to the left side of the channel. At the moving perfectly conducting wall at $y = 1$ and $0 < z \leq b$ the dimensionless velocity is one

6

$(u = 1)$ and the z–component of the current density j_z is equal to zero $\left(\dfrac{\partial h(1,z)}{\partial y} = 0\right)$. Along

the free surface from $y = 1$ to $b < z < a + b$, the shear is zero $\left(\dfrac{\partial u(1,z)}{\partial y} = 0\right)$ and the

current density stream function $h(1,z)$ equals a constant h_0. Along the stationary perfectly conducting side wall from $0 \le y \le 1$ and $z = a + b$ the dimensionless velocity is zero

$(u = 0)$ and the y–component of the current density j_y equals zero $\left(\dfrac{\partial h(y,a+b)}{\partial z} = 0\right)$. At the

bottom stationary perfectly conducting wall from $0 \le z \le a + b$ at $y = 0$ the dimensionless velocity u is zero $(u = 0)$ and the z-component of the current density j_z

equals zero $\left(\dfrac{\partial h(0,z)}{\partial y} = 0\right)$. At the plane of symmetry, $\dfrac{\partial u}{\partial z} = 0$ and $h = 0$ from $0 \le y \le 1$

at $z = 0$.

The homogeneous, second-order partial differential Eqs. 5.1 and 5.2 are assumed to have solutions for $u(y,z)$ and $h(y,z)$ of the form

$$u(y,z) = \sum_{n=0}^{\infty} U_n(y) \, cos\left[\left(\frac{2n+1}{2}\right)\left(\frac{\pi z}{a+b}\right)\right] \; , \tag{6.1}$$

$$h(y,z) = \sum_{n=0}^{\infty} H_n(y) \, sin\left[\left(\frac{2n+1}{2}\right)\left(\frac{\pi z}{a+b}\right)\right] \; , \tag{6.2}$$

which satisfy the boundary conditions at $z = 0$ and $z = a + b$.

Substituting series expressions 6.1 and 6.2 for $u(y,z)$ and $h(y,z)$ respectively, into the simultaneous partial differential Eqs. 5.1 and 5.2 and solving for $H_n(y)$ results in the following ordinary differential equation for $H_n(y)$:

$$\frac{d^4 H_n(y)}{dy^4} - 2\delta_n^2 \frac{d^2 H_n(y)}{dy^2} + \left(\delta_n^4 + \delta_n^2 M^2\right) H_n(y) = 0 \; , \tag{7}$$

where $\quad \delta_n = \left[\left(\dfrac{2n+1}{2}\right)\dfrac{\pi}{(a+b))}\right]$.

$H_n(y)$ is assumed to have a general solution of the form[10]

$$H_n(y) = coshPy + DsinhPy \; . \tag{8}$$

Substituting Eq. 8 into Eq. 7 gives the following algebraic equation for P

$$P^4 - 2\delta_n^2 P^2 + \delta_n^2\left(\delta_n^2 + M^2\right) = 0 \; , \tag{9.1}$$

where $\quad P_{1,2} = \sqrt{\delta_n^2 \pm i\delta_n M} \;$. $\tag{9.2}$

Expressing P_1 and P_2 in terms of real and imaginary parts[10], we have

$$P_1 = m_r + im_i \tag{10.1}$$

$$P_2 = m_r - im_i . \tag{10.2}$$

where

$$m_r = \sqrt{2}\, \delta_n \left[\left(1 + M^2 \delta_n^{-2}\right)^{1/2} + 1\right]^{1/2} , \tag{10.3}$$

and

$$m_i = \sqrt{2}\, \delta_n \left[\left(1 + M^2 \delta_n^{-2}\right)^{1/2} - 1\right]^{1/2} . \tag{10.4}$$

Thus $H_n(y)$ has the following general solution

$$H_n(y) = A_{n1} \cosh(P_1 y) + A_{n2} \cosh(P_2 y) + A_{n3} \sinh(P_1 y) + A_{n4} \sinh(P_2 y) , \tag{11.1}$$

or more simply

$$
\begin{aligned}
H_n(y) = & (A_{n1} + A_{n2}) \cosh(m_r y) \cos(m_i y) \\
& + (A_{n3} + A_{n4}) \sinh(m_r y) \cos(m_i y) \\
& + i (A_{n3} - A_{n4}) \cosh(m_r y) \sin(m_i y) \\
& + i (A_{n1} - A_{n2}) \sinh(m_r y) \sin(m_i y) ,
\end{aligned}
\tag{11.2}
$$

where

$$
\begin{aligned}
a_{n1} &= (A_{n1} + A_{n2}) , \\
a_{n2} &= (A_{n3} + A_{n4}) , \\
a_{n3} &= i (A_{n3} - A_{n4}) , \\
a_{n4} &= i (A_{n1} - A_{n2}) .
\end{aligned}
\tag{11.3}
$$

$U_n(y)$ can be determined from the equation (see Eq. 5.2)

$$\frac{1}{M}\left[\frac{d^2 H_n(y)}{dy^2} - \delta_n^2 H_n(y)\right] - \delta_n U_n(y) = 0 \tag{12}$$

by substituting Eq. 11.1 for $H_n(y)$. Thus $U_n(y)$ is determined to have the form

$$U_n(y) = A_{n1}\, i\cosh(P_1 y) - A_{n2}\, i\cosh(P_2 y) + A_{n3}\, i\sinh(P_1 y) - A_{n4}\, i\sinh(P_2 y) , \tag{13.1}$$

which can be expressed more simply as

$$
\begin{aligned}
U_n(y) = & -(A_{n1} + A_{n2}) \sinh(m_r y) \sin(m_i y) \\
& + i (A_{n1} - A_{n2}) \cosh(m_r y) \cos(m_i y) \\
& + i (A_{n3} - A_{n4}) \sinh(m_r y) \cos(m_i y) \\
& - i (A_{n3} + A_{n4}) \cosh(m_r y) \sin(m_i y) ,
\end{aligned}
\tag{13.2}
$$

where

$$
\begin{aligned}
-(A_{n1} + A_{n2}) &= -a_{n1} , \\
i (A_{n1} - A_{n2}) &= a_{n4} , \\
i (A_{n3} - A_{n4}) &= a_{n3} , \\
-(A_{n3} + A_{n4}) &= -a_{n2} .
\end{aligned}
\tag{13.3}
$$

8

When the boundary conditions at $y = 0$ are applied $\left(\dfrac{dH_n(y)}{dy} = 0 \text{ and } U_n(y) = 0 \right)$ to Eqs. 6.1 and 6.2, we obtain

$$a_{n3} = -\frac{m_r}{m_i} a_{n2} \quad \text{and} \quad a_{n4} = 0 \ . \tag{14}$$

Therefore, the expressions for $H_n(y)$ and $U_n(y)$ are

$$
\begin{aligned}
H_n(y) = a_{n1} &\cosh(m_r y)\cos(m_i y) \\
&+ a_{n2}\left[\sinh(m_r y)\cos(m_i y) - \frac{m_r}{m_i}\cosh(m_r y)\sin(m_i y) \right]
\end{aligned}
\tag{15.1}
$$

and

$$
\begin{aligned}
U_n(y) = -a_{n1} &\sinh(m_r y)\sin(m_i y) \\
&- a_{n2}\left[\cosh(m_r y)\sin(m_i y) + \frac{m_r}{m_i}\sinh(m_r y)\cos(m_i y) \right] \ ,
\end{aligned}
\tag{15.2}
$$

where

$$m_r = \sqrt{2}\ \delta_n \left[\left(1 + M^2\delta_n^{-2}\right)^{1/2} + 1 \right]^{1/2} \ , \tag{15.3}$$

$$m_i = \sqrt{2}\ \delta_n \left[\left(1 + M^2\delta_n^{-2}\right)^{1/2} - 1 \right]^{1/2} \ , \text{ and} \tag{15.4}$$

$$\delta_n = \left[\left(\frac{2n+1}{2}\right)\frac{\pi}{(a+b)} \right] \ .$$

Since the current densities j_y and j_z are even and odd functions of z, respectively, h is an odd function of z, if the constant value of h at $z = 0$ is chosen as zero. The boundary condition $j_y = 0$ at the free surface indicates that $h(y,z)$ is a constant along the free surface. The constant h_o denotes this value and *represents half the total dimensionless current from the stationary walls to the moving wall.*

The total dimensionless current from the stationary wall to the moving wall along the nondimensional length of the channel Δx is

$$I = 2(\Delta x) \int_0^b j_y(1,z)\, dz = 2\,(\Delta x)\, M^{-1} h_o \ , \tag{16.1}$$

where the dimensional current is expressed as

$$I^* = 2 h_o U_o (\sigma\mu_f)^{1/2} (\Delta x^*) \ , \text{ and } \Delta x^* = L(\Delta x^*) \ . \tag{16.2}$$

Once we obtain the computer solutions for $u(y,z)$ and $h(y,z)$ for given values of the parameters a, b, M and h_o, we can compute the potential difference between the moving wall and stationary walls needed to drive this total current.

$$\phi_o = -\int_0^1 \left[u(y,z) + M^{-1}\frac{\partial h(y,z)}{\partial z} \right] dy \quad \text{for} \quad 0 \le z \le b \ . \tag{17}$$

The dimensional potential difference is then

$$\phi_o^* = U_o B_o L \, \phi_o \; .$$

If h_o has the same value for a range of values of B_o, it represents a constant total electric current from the stationary wall to the moving wall for all these field strengths. On the other hand, if ϕ_o has the same value for a range of values of B_o, it represents a dimensional potential difference which is proportional to B_o.

A positive h_o represents a total current from the stationary, perfectly conducting bottom wall to the moving, perfectly conducting top wall. A negative h_o represents total current flowing in the opposite direction. Here, we assume that the rotor moves in the positive x-direction and that the axial magnetic field is in the positive z-direction. In a motor, the electromagnetic (EM) body force due to the load current and applied magnetic field is in the same direction as the rotor's motion. Since positive h_o gives an EM body force in the positive x-direction, results for positive h_o correspond to current collectors in motors. In a generator, the EM body force is in the opposite direction to the rotor's motion, which is the case for negative h_o. Therefore, the results for negative h_o correspond to current collectors in generators.

METHOD OF WEIGHTED RESIDUALS

From the boundary conditions at the moving wall and at the free surface, we determine the coefficients a_{n1} and a_{n2} by defining a residual

$$E = \int_0^b \left\{ \left[\sum_{n=0}^{\infty} \frac{dH_n(1)}{dy} \sin(\delta_n z) \right]^2 + \left[1 - \sum_{n=0}^{\infty} U_n(1) \cos(\delta_n z) \right]^2 \right\} dz$$

$$+ \int_b^{a+b} \left\{ \left[h_o - \sum_{n=0}^{\infty} H_n(1) \sin(\delta_n z) \right]^2 + \left[\sum_{n=0}^{\infty} \frac{dU_n(1)}{dy} \cos(\delta_n z) \right]^2 \right\} dz \; , \tag{18}$$

where

$$u(y,z) = \sum_{n=0}^{\infty} U_n(y) \cos\left[\left(\frac{2n+1}{2} \right) \left(\frac{\pi z}{a+b} \right) \right] \; ,$$

$$h(y,z) = \sum_{n=0}^{\infty} H_n(y) \sin\left[\left(\frac{2n+1}{2} \right) \left(\frac{\pi z}{a+b} \right) \right] \; ,$$

and

$$j_z = -\frac{1}{M} \sum_{n=0}^{\infty} \frac{dH_n(y)}{dy} \sin\left[\left(\frac{2n+1}{2}\right)\left(\frac{\pi z}{a+b}\right)\right] ,$$

$$\frac{\partial u(y,z)}{\partial y} = \sum_{n=0}^{\infty} \frac{dU_n(y)}{dy} \cos\left[\left(\frac{2n+1}{2}\right)\left(\frac{\pi z}{a+b}\right)\right] .$$

In this equation we have used the notion of convergence as *mean square convergence*. The first integral from 0 to b represents the convergence of the appropriate series to the boundary conditions along the moving, perfectly conducting wall. The first squared bracket in the first integral represents the convergence to $j_z = -\frac{1}{M}\frac{\partial h}{\partial y} = 0$.

The second squared bracket in the second integral represents the convergence of the velocity series to 1 along the moving wall from $z = 0$ is equal to b. The first squared term in the second integral represents the convergence of the current density stream function or induced magnetic field to h_o along the free surface from z equals b to $a + b$. The second squared bracket represents the convergence of the y partial derivative of the velocity to zero along the free surface from b to $a + b$.

The residual must be minimized with respect to the coefficients

$$\frac{\partial E}{\partial a_{\ell 1}} = 0 \quad \text{and} \quad \frac{\partial E}{\partial a_{\ell 2}} = 0 \quad \text{for } \ell = 0, 1, 2, \dots N , \tag{19}$$

with the series truncated at $n = N$. The result is $2N$ simultaneous linear, algebraic equations with the $2N$ unknowns

$$a_{11}, a_{21}, \dots a_{N1} ,$$
$$a_{12}, a_{22}, \dots a_{N2} . \tag{20}$$

For a specific set of values for a, b, M, h_o, and N, we solve the simultaneous equations for the $2N$ unknown coefficients. The series solutions for $u(y,z)$ and $h(y,z)$ now give the values of $u(y,z)$ and $h(y,z)$ throughout the liquid metal. In addition, the following relationship holds for the electric potential

$$\phi(y,z) = -M^{-1} \sum_{n=0}^{\infty} \frac{dH_n(y)}{dy} \delta_n^{-1} \cos(\delta_n z) . \tag{21}$$

RESULTS AND DISCUSSION

Graphical data are presented for the nondimensional velocity $u(y,z)$ and nondimensional current density stream function or induced magnetic field $h(y,z)$ for the magnetohydrodynamic channel with a moving perfectly conducting top wall having two free surfaces at the top corners (see Fig. 4). The channel parameters were chosen to illustrate variations of several key features that are typical for current collectors in motors

PERFECTLY CONDUCTING MOVING WALL AT
VELOCITY U_0, ELECTRIC POTENTIAL $= B_0 L \emptyset_0$ FREE SURFACE
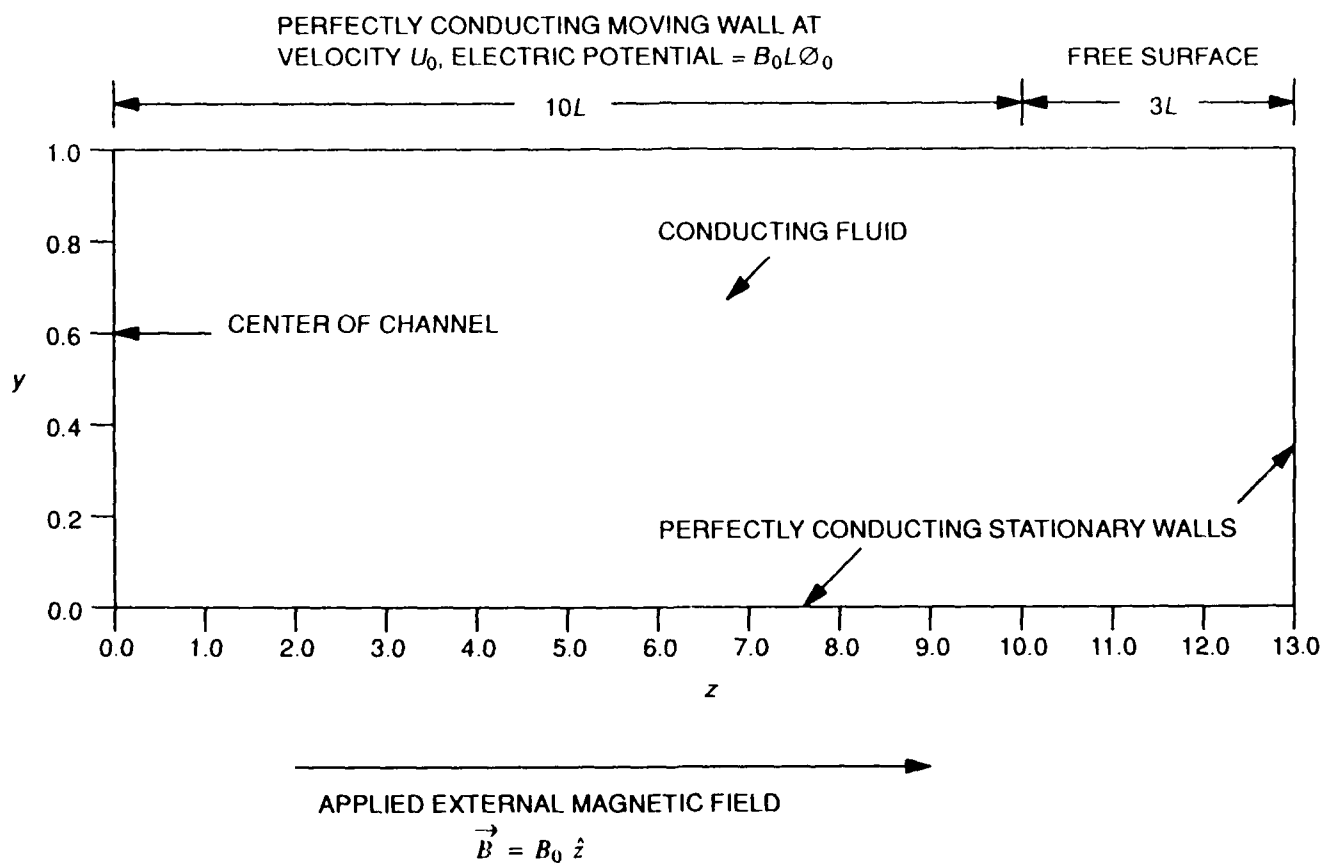
Fig. 4.   Coordinates for Contour plots.

12

and generators. The radial gap was chosen as length L, each axial free surface gap as $3L$, and the length of the moving wall as $20L$. The stationary walls and moving walls were chosen to be perfect conductors. These lengths were nondimensionalized with respect to L. The applied magnetic field was varied through the Hartmann number $M = B_o L \sqrt{\sigma/\mu_f}$.

Typical values for liquid metal current collectors in homopolar motors would be $M = 2$ to 50. Although in the discussion that follows the dependence of various quantities on variations of the Hartmann number has been interpreted in terms of applied magnetic field variations, the discussion is equally applicable to constant applied magnetic field and variations of other parameters that make up the Hartmann number. These include the distance between the top and bottom conducting walls and the fluid's electrical conductivity and viscosity. In this work the nondimensional pressure gradient was set equal to zero. Thus the fluid motion is due only to the drag of the moving wall and the $\vec{j} \times \vec{B_o}$ body force. Only the right half of the channel was drawn for each figure presented herein since the calculated value of the velocity is symmetrical and since the induced magnetic field is anti-symmetrical with respect to z.

The total current from the stationary to the moving wall (stator to rotor) along the length of the channel x is given by

$$I^* = 2\left(\Delta x^*\right) \sigma U_o B_o L\, h_o M^{-1} \tag{22.1}$$

$$I^* = 2h_o U_o (\sigma \mu_f)^{1/2} \left(\Delta x^*\right) , \tag{22.2}$$

where

I^* = total dimensional current,
U_o = velocity of moving wall,
σ = conductivity of fluid,
μ_f = viscosity of fluid,
h_o = parameter representing the total current,
$(\Delta x^*) = (\Delta x)\, L$ = dimensional longitudinal length along channel.

The total nondimensional viscous dissipation per unit nondimensional length in the channel is calculated from

$$P_\mu = \int_{-(a+b)}^{(a+b)} \int_0^1 \left[\left(\frac{\partial u}{\partial y}\right)^2 + \left(\frac{\partial u}{\partial z}\right)^2 \right] dy\, dz , \tag{23}$$

where $P_\mu^* = \mu_f U_o^2\, P_\mu$, and the superscript (*) represents a dimensional quantity. Also, the

13

total nondimensional Joulean dissipation per nondimensional unit length in the channel is calculated from

$$P_j = M^2 \int_{-(a+b)}^{(a+b)} \int_0^1 \left[j_y^2 + j_z^2 \right] dy \, dz \; ,$$

(24)

where $P_j^* = \mu_f U_o^2 \, P_j$.

Data were calculated numerically on the computer for half the nondimensional length of the moving wall $b = 10$ and the free surface nondimensional length $a = 3$. The Hartmann number cases studied were $M = 2$ and 10. The total current between the moving and stationary walls was represented by $h_o = 0, \pm 20, \pm 40, \pm 60, \pm 80, \pm 100$. A positive h_o represents the total current moving from the stationary conducting wall to the moving conducting wall, and a negative h_o represents current from the moving conducting wall to the stationary conducting wall. The quantity h_o was chosen to represent typical load currents carried by current collectors in generators or motors. The higher positive and negative h_o values correspond to very high load currents. Due to symmetry considerations only one half of the channel is shown (i.e., right side of channel). The y-axis has been stretched by a factor of 5 in the contour plots $0 \le y \le 1$ and the z-axis runs from 0 to 13.

Due to the contour routine utilized to plot the contours, the singularity at the top corner of the moving wall has been smeared across two elements, one of which lies on the free surface. Therefore, current lines that appear to enter the free surface actually enter the moving wall, so that current densities at the moving wall are larger than those shown in the contour plots.

Figure 5a presents composite contour plots of nondimensional velocity $u(y,z)$, and contour plots of current density stream function (induced magnetic field) $h(y,z) \times 1000$ in the right hand side of the channel at Hartmann number $M = 2$ and $h_o = 0$. The velocity contours representing flow in the positive x-direction are represented by solid lines. Later in the report, velocity contours representing flow in the negative x-direction are represented by dashed lines. The induced magnetic field contour lines are represented by dashed lines with dots and arrows showing the direction of current density flow. When $h_o = 0$ there is no net current flow between the moving, perfectly conducting top wall and the stationary, perfectly conducting bottom wall. The analogous one-dimensional Couette flow problem (Appendix B) in a constant, homogeneous axial magnetic field with no nondimensional pressure gradient would give the nondimensional velocity $u(y) = y$, the external applied nondimensional potential $\phi_o = -0.5$, and the y-component of the nondimensional current density $j_y = 0$. In Fig. 5a for the region $0 \le z \le 9$ and $0 \le y \le 1$ we have approximately the simple Couette flow solution $u(y) = y$. For the region $10 \le z \le 13$ and $0 \le y \le 1$ the stress-free surface does not drive the fluid, and the stationary, perfectly conducting sidewall retards the fluid. The fluid that flows in this region moves because of its viscous interaction with the simple Couette flow between the moving top wall and stationary bottom wall. The flow pattern extends from approximately $z \le 9$ to $z \le 12$.

14

The induced magnetic field acts as a stream function for the current density and therefore expresses the fact that the direction of the tangent to a streamline is the direction of the current density. The current density at each point of the fluid is determined by the Ohm's law relationship $\vec{j} = -\vec{\nabla}\phi + \vec{u} \times \hat{z}$. An axial variation of $u(y,z)$ acts as a generator in an axial magnetic field. This will drive an external circulation of current. In the figure there is a large axial velocity gradient between $z = 9.5$ and $z = 11.5$. Since the flow is in the positive x-direction, the current density circulation is counterclockwise. As the current density circulates, the Lorentz body force tries to minimize the axial variation of the nondimensional velocity $u(y,z)$.

The axial lines of the current density circulation are inside the perfect contours because this represents a lower resistance than the liquid metal. There are downward current density lines for $0 \le z \le 9.5$ and upward current density lines from $9.5 \le z \le 13$. The upward current density lines must converge to the edge of the perfectly conducting moving wall at $y = 1$, $z = 10$ because of the insulating electrical properties of the free surface.

If the problem is viewed in another way, the externally applied potential $\phi_o = \phi(y = 1,z)$ for $-b \le z \le b$ must produce an electric field at each point of the fluid that balances some global average of $\vec{u} \times \hat{z}$ throughout the fluid so that there is no net current. If there were pure Couette flow, then $\phi_o = -0.5$ (see Appendix B). However, the fluid near $z = 13$ is moving at $u < y$, so $|\phi_o| < 0.5$. For $0 \le z \le 9.5$, the flow approximates pure Couette flow; thus $\vec{u} \times \hat{z} = -u\,\hat{y}$ is larger in magnitude than $E_y = \dfrac{\partial \phi}{\partial y} > 0$, so current density lines are downward. For $z > 9.5$, $\vec{u} \times \hat{z}$ is very small, so $E_y > u$ and current density lines are upward. The current density decelerates flow for $0 \le z \le 9.5$ and accelerates flow for $9.5 \le z \le 13$, but for $M = 2$ the Lorentz force is too small in magnitude to significantly alter $u(y,z)$.

Figure 5b presents composite contour plots of nondimensional velocity $u(y,z)$ and contour plots of current density stream function (induced magnetic field) $h(y,z) \times 1000$ in the right hand side of the channel at Hartmann number $M = 10$ and $h_o = 0$. The Lorentz body force acting on the fluid for $M = 10$, $h_o = 0$ is much greater than for $M = 2$, $h_o = 0$ (Figs. 5a and 5b). For the case where $M = 10$, the flow profile is altered and the axial velocity gradient is reduced, in contrast to the $M = 2$ case. Figure 5b indicates that the nondimensional velocity profile for $9.5 \le z \le 13$ has been increased slightly relative to that for $M = 2$. We need to remember that the vertical scale is stretched by a factor of 5. The effect of the moving wall on the fluid flow is extended well beyond the end of the moving wall. Correspondingly the velocity for $0 \le z \le 9$ has been reduced below that for Couette flow. For the current density stream function there are several important features to recognize. For $M = 2$, $h_o = 0$ and $9.5 \le z \le 13$, virtually all of the current density lines move from the stationary wall at $y = 0$ and converge to the end of the moving wall. For $M = 10$, a large number of current density lines leave the sidewall at $z = 13$ for
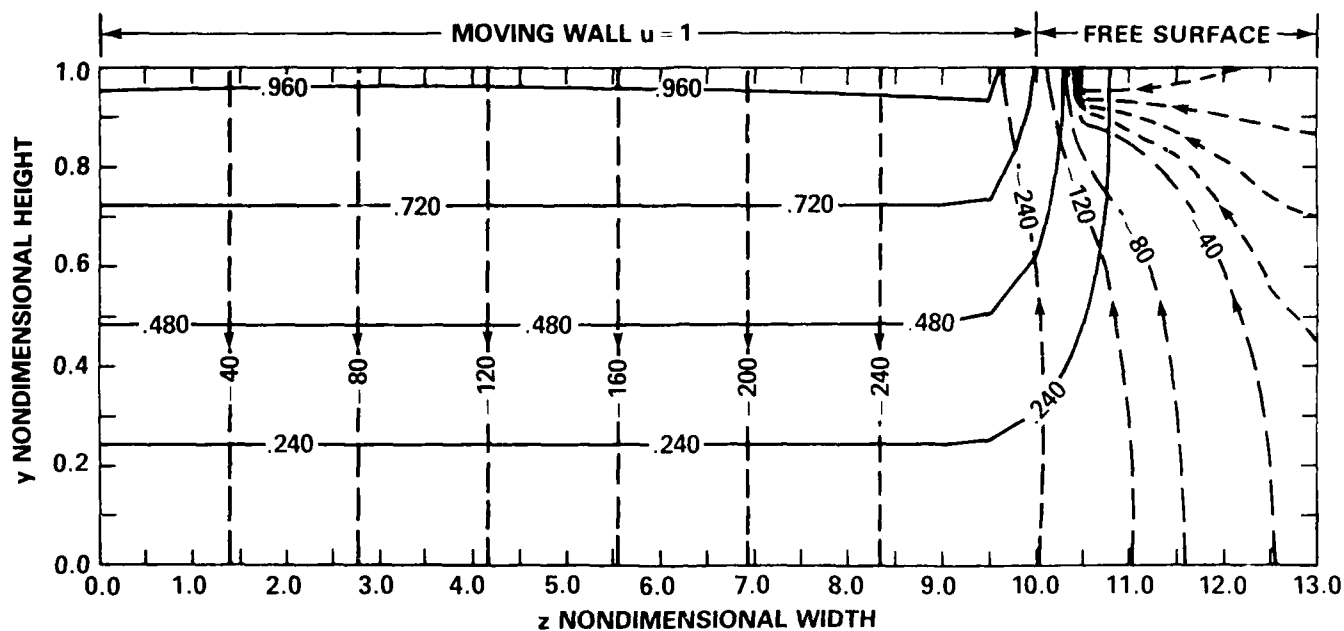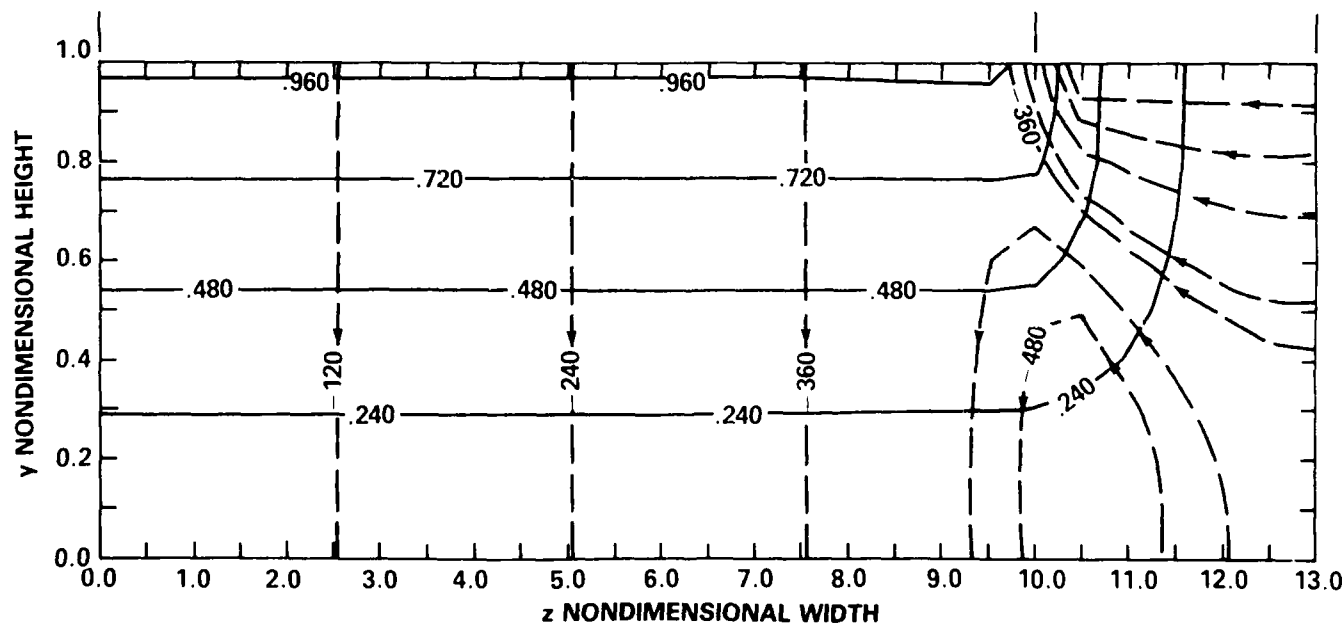
Fig. 5a. $M = 2$, $h_o = 0$

Fig. 5b. $M = 10$, $h_o = 0$

Fig. 5.   Nondimensional velocity contours $u(y,z)$ and nondimensional current density stream function $h(y,z) \times 1000$ for Hartmann numbers $M = 2$ and 10, and $h_o = 0$.

$0.25 \leq z \leq 1$. There are several ways to view this. The solution for one-dimensional Couette flow (presented in Appendix B) showed that a current across the magnetic field lines produces a velocity change which in turn opposes the current density. This leads to an effective resistance to the current density j_y which is given by

$$R_{eff} = R\left(1 + \frac{M^2}{12}\right) .$$

(25)

On the other hand, current density lines along magnetic field lines produce no body force $\vec{j} \times \vec{B}_o$, so these lines do not alter the flow or generate any increase in the effective resistance. Therefore, j_z always sees a resistance R, while j_y sees the effective resistance $R = R_{eff}$. For the case $M = 2$, $h_o = 0$, there is a small difference between the resistances for j_y and j_z, so both current densities see approximately the same resistance in the fluid. The distance from the stationary, perfectly conducting wall at $y = 0$ to the moving, perfectly conducting wall at $y = 1$ is of length L, but the approximate length from the stationary, perfectly conducting side wall at $z = 13$ to the moving wall is $3L$, so the current density path of least resistance is from the bottom to the moving wall. For the case $M = 10$, the effective resistance $R_{eff} = 9.33R$, so that the path from the sidewall to the moving wall has a lower resistance than that from the stationary bottom wall to the moving top wall. Of course, the current density cannot be only the j_z-component, because as it reaches the moving wall it must turn into the j_y-component to enter the moving wall. However, the current density lines have only a short distance to travel in the y-direction.

An $M^{-1/2}$ thick free surface boundary layer would predict that the current lines would be a series of parabolas converging to a current sink at the edge of the moving wall and the current density lines in Fig. 5b have precisely this parabolic shape. The $M^{-1/2}$ layer would have an appropriate actual thickness of $H^{1/2}M^{-1/2}$ where H is the dimensionless height of the layer along a magnetic line.

A second feature of Fig. 5b is the recirculation of the current density lines near $z = 10.5$, $y = 0$. In spite of the Lorentz body force effects, the fluid near $z = 13$, $y = 0$ remains at small velocity because of the no-slip condition on the two walls at the corner. Therefore, there is a local battery action at this corner. One part of the circulation is short-circuited through the stationary bottom wall, but the other part of the path closes through the liquid. There would be a higher resistance in a path to the perfectly conducting moving wall than in the path just inside the liquid.

Figures 6a through 6c present composite contour plots of nondimensional velocity $u(y,z)$ and current density stream function or induced magnetic field $h(y,z)$ for Hartmann number $M = 2$ and $h_o = 20$, 60 and 100. The stream function contours are represented by dotted lines with arrows. The velocity profile contours in the positive x-direction are represented by solid lines. The positive values of h_o represent relatively strong net current moving from the stationary, perfectly conducting bottom wall to the moving, perfectly conducting top wall. In each h_o case for $M = 2$ there are essentially two current paths available. In the first path current can flow across the relatively narrow gap between the top moving wall and the bottom stationary wall. However, the large positive y-component of the nondimensional current density j_y accelerates the flow, and then the induced electric field opposes the current, increasing the effective resistance by a small amount. The
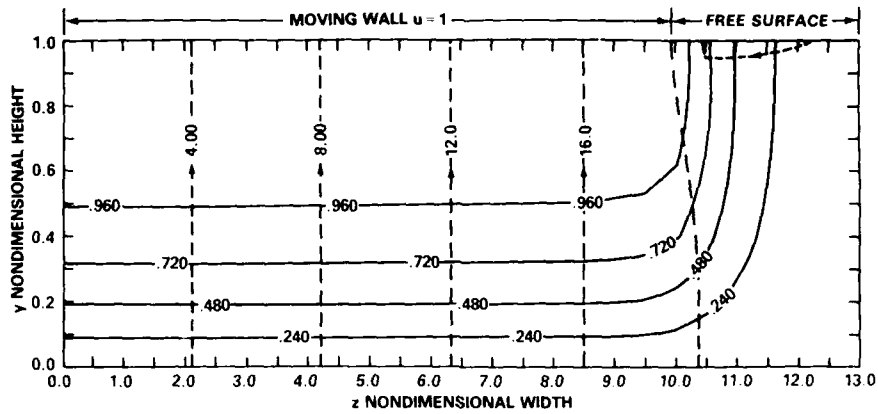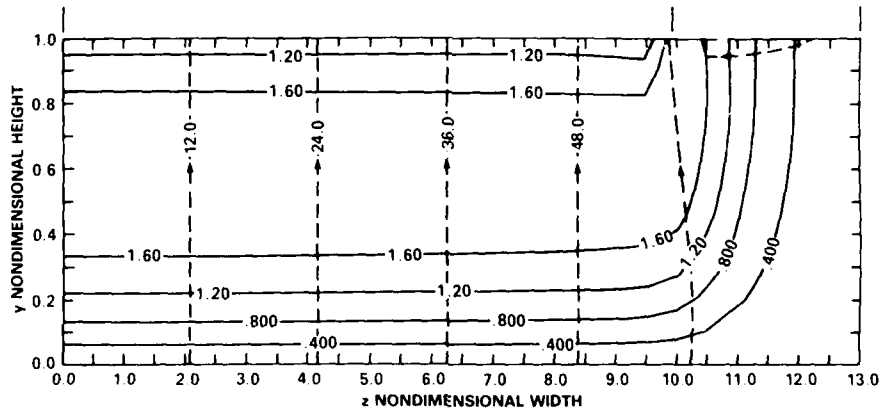
17

Fig. 6a. $M = 2$, $h_O = 20$

Fig. 6b. $M = 2$, $h_O = 60$

Fig. 6c. $M = 2$, $h_O = 100$

Fig. 6. Nondimensional velocity contours $u(y,z)$ and nondimensional current density stream function $h(y,z)$ for Hartmann number $M = 2$ and $h_O = 20$, 60, and 100.

18

second current path is along the magnetic field lines near the free surface and then into the edge of the moving wall. This has a longer path than the first process, approximately $3L$. The current density lines along the field lines do not produce a flow acceleration, thus this phenomenon decreases the effective resistance. However, the final parts of the current density paths involve a very large nondimensional current density j_y near the edge of the top, moving wall which locally accelerates the flow and which produces an increased effective resistance for this small region. The effective resistance of the end of this moving wall end region probably varies as some power of $M^{1/2}$ or M. The resistance across the gap increases as M^2. Therefore, an increase of M will cause a progressive shift of the current from the radial gap of length L to the region near the free surface. The larger the transport current the faster the fluid moves in the channel if the other parameters stay the same.

The nondimensional positive velocity profiles $u(y,z)$ for the two-dimensional model when $M = 2$ in the region $0 \leq z \leq 10$ and $0 \leq y \leq 1$ approximate, but are slightly less than the corresponding nondimensional, one-dimensional velocity profiles for the Couette model for $M = 2$ and $h_o = 20$, 60, and 100. Appropriate values of the nondimensional velocity $u(y) = 0.25$, 0.50, and 0.75) and u_{max} for one-dimensional Couette flow with an axial magnetic field and no pressure gradient $\partial P/\partial x$ are presented in Table 1 for $M = 2$ for comparison. The nondimensional velocity profiles are similar for the two-dimensional and one-dimensional model because current end effects are small in the two-dimensional model at a low Hartmann number of $M = 2$. That is, all the two-dimensional figures for $h_o = 20$ to 100 show all induced current density contour lines in the region $0 \leq z \leq 10.5$ for $M = 2$ from the stationary, perfectly conducting wall to the moving, perfectly conducting wall except for one current density contour across the free surface shown in all figures except Fig. 6c. In all figures for $M = 2$, as positive h_o increases, the induced magnetic field contour lines generally increase in magnitude and the nondimensional velocity contour lines also generally increase in magnitude.

Figures 7a through 7c represent the composite contour plots of nondimensional velocity $u(y,z)$ in the positive x-direction and nondimensional induced magnetic field for $M = 10$ and $h_o = 20$, 60, and 100. The positive values of h_o represent relatively strong net current between the stationary, perfectly conducting bottom wall and the moving, perfectly conducting top wall. The two-dimensional, nondimensional velocity profiles $u(y,z)$ for the region $0 \leq z \leq 10$ for $0 \leq y \leq 1$, are in general significantly less than the corresponding one-dimensional, nondimensional velocity profiles $u(y)$ of simple Couette flow in an axial magnetic field for $M = 10$ and $h_o = 20$ to 100. Appropriate values of the nondimensional velocity $u(y = .25, .50,$ and $.75)$ and u_{max} for one-dimensional Couette flow for $M = 10$ are shown in Table 1. As the Hartmann number M was increased from 2 to 10 in this set of computed data, the axial magnetic field was increased, which results in the figures for $M = 10$ showing many more induced magnetic field contour lines than the figures for $M = 2$ from the perfectly conducting, stationary right side wall to the tip of the perfectly conducting moving wall. The induced magnetic field contour lines for $M = 2$ for the region $0 \leq z \leq 10$ and $0 \leq y \leq 1$ are the same magnitude as the corresponding contour lines for $M = 10$, except that in the $M = 2$ case the lines are sometimes shifted slightly to the left. Thus, there is a slight decrease of current across the gap of length L

Fig. 7a. $M = 10$, $h_O = 20$
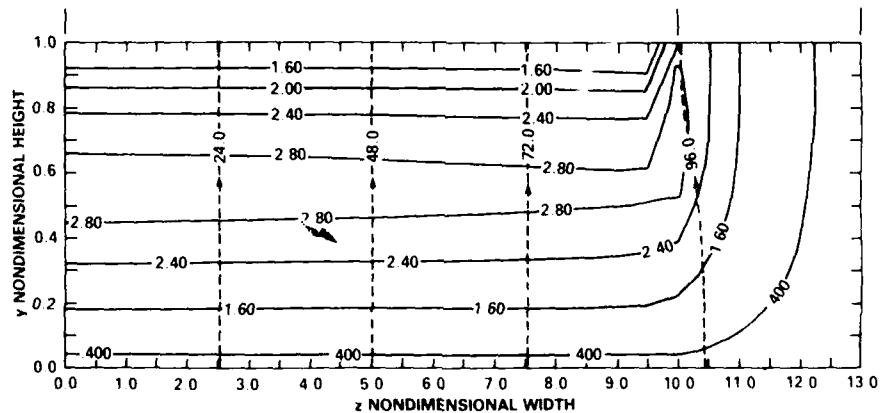

Fig. 7b. $M = 10$, $h_O = 60$

Fig. 7c. $M = 10$, $h_O = 100$

Fig. 7. Nondimensional velocity contours $u(y,z)$ and nondimensional current density stream function $h(y,z)$ for Hartmann number $M = 10$ and $h_O = 20$, 60, and 100.

20

Table 1. One-dimensional Couette flow values for axial magnetic field.

Hartmann No.	h_o	$u(.75)$	$u(.50)$	$u(.25)$	u_{max}	y_{max}
	20	1.13	1.00	0.63	1.13	0.75
	40	1.51	1.50	1.01	1.57	0.63
M = 2	60	1.89	2.00	1.39	2.04	0.58
	80	2.27	2.50	1.77	2.53	0.56
	100	2.65	3.00	2.15	3.03	0.55
	20	2.65	3.00	2.15	3.03	0.55
	40	4.55	5.50	4.05	5.51	0.53
M = 10	60	6.40	8.00	5.95	8.01	0.52
	80	8.35	10.50	7.85	10.50	0.51
	100	10.25	13.00	9.75	13.05	0.51

from the bottom conducting wall to the top moving conducting wall when M goes from 2 to 10 as would be expected from previous arguments. The nondimensional velocity profiles for the $M = 10$ case are generally of a much higher order of magnitude than the corresponding nondimensional velocity profiles for the $M = 2$ case because of the much increased $\vec{j} \times \vec{B}_o$ body force in the fluid. The opposing induced electric field $\sigma\left(\vec{V} \times \vec{B}_o\right)$ is much larger in the $M = 10$ case than the $M = 2$ case.

These sets of data for $M = 2$ and $M = 10$ for $h_o = 20$, 60, and 100 support the concept that the radial gap and the free surface region represent electrical resistances in parallel between the stationary walls and the moving wall. It also shows that the resistance of the radial gap increases as M^2 while that of the free surface region increases as M or $M^{1/2}$. Thus as M increases, the division of current shifts to the free surface region and the current density in the radial gap decreases as M^{-1}. We have already justified the idea that the radial gap resistance varies as M^2. The resistance of the free surface region is less clear. In the limit as $M \to \infty$, this region becomes a parabolic one. Figure 8 shows high Hartmann number regions at tip of the moving wall. All current must pass through the $O\ (M^{-1}) \times O\ (M^{-1})$ corner region at the edge of the moving wall. However, from this theoretical development, it is not clear whether the free surface layer with $M^{-1/2}$ thickness or the corner region with M^{-1} thickness is the dominant resistance.
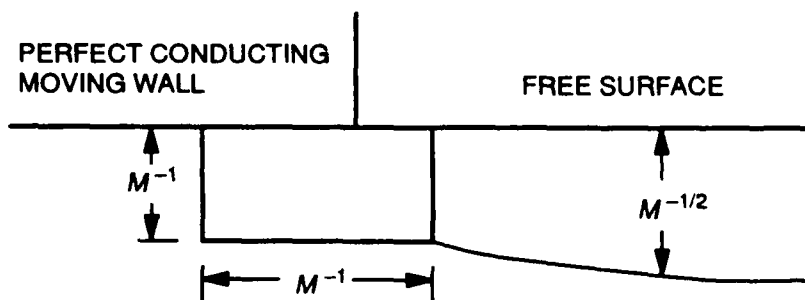
Fig. 8. High Hartmann number regions at tip of moving wall.

Figures 9a through 9c present the composite contour plots of nondimensional velocity $u(y,z)$ and nondimensional induced magnetic field $h(y,z)$ for $M = 2$ and $h_o = -20, -60$, and -100. The dashed lines with dots show velocity profiles in the negative direction. The solid lines are velocity profiles in the positive x-direction as in previous contour plots. The induced magnetic field contour plots are dashed lines with arrows. The negative values of h_o represent relatively strong net current from the moving, perfectly conducting top wall to the stationary, perfectly conducting bottom wall. In each negative h_o case there are two current paths available as discussed previously. In the first case current can flow directly from the moving wall to the stationary wall. However, the large negative y-component of the nondimensional current density j_y accelerates the flow in the negative x-direction and the induced electric field opposes the current, increasing the effective resistance across the channel by a small amount. The velocity of the fluid is in the positive x-direction close to the moving wall because of viscous action between the moving wall
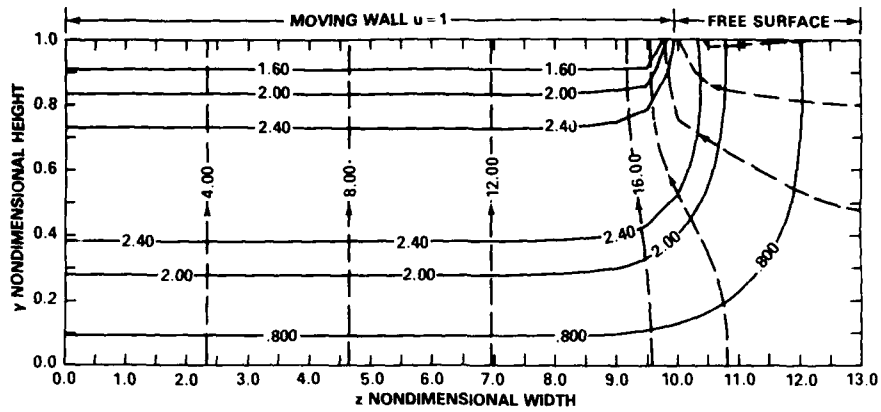
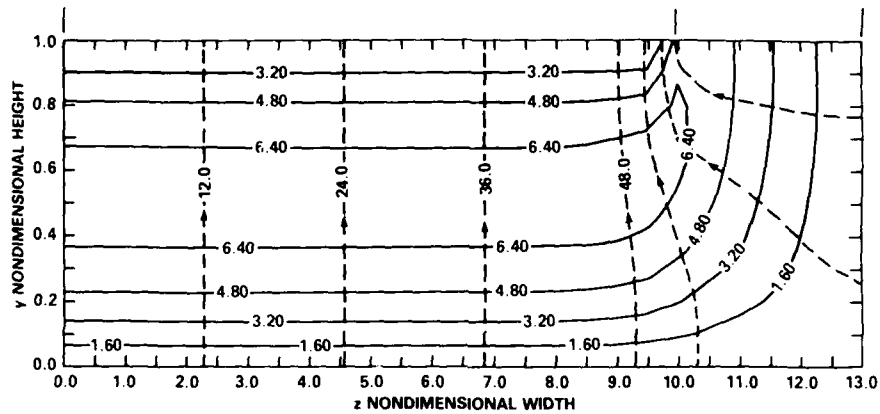22

Fig. 9a. $M = 2$, $h_0 = -20$
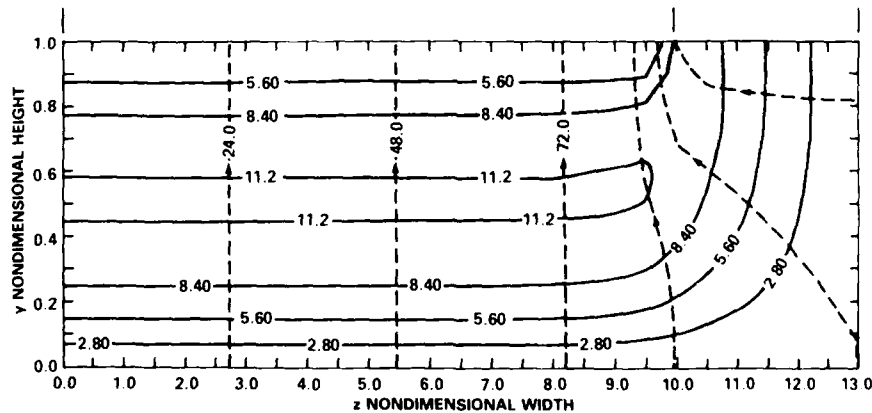

Fig. 9b. $M = 2$, $h_0 = -60$

Fig. 9c. $M = 2$, $h_0 = -100$

Fig. 9. Nondimensional velocity contours $u(y,z)$ and nondimensional current density stream function $h(y,z)$ for Hartmann number $M = 2$ and $h_0 = -20$, -60, and -100.

and the fluid. The second current path is out of the edge of the moving wall and along the magnetic field lines near the free surface. As previously discussed, a shift of M from $M = 2$ to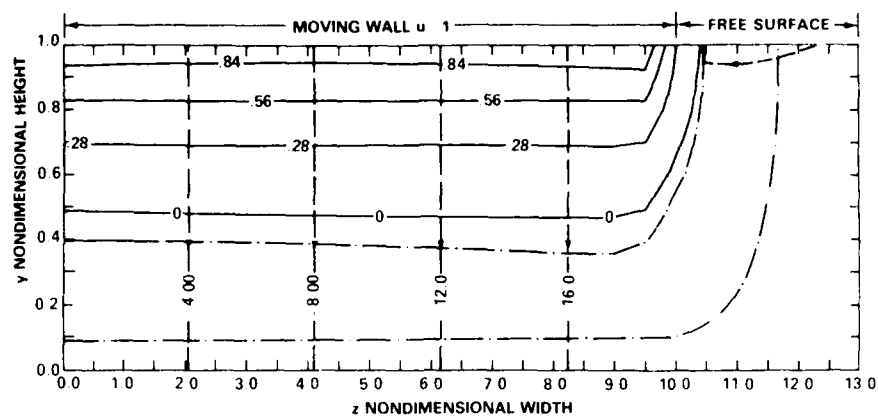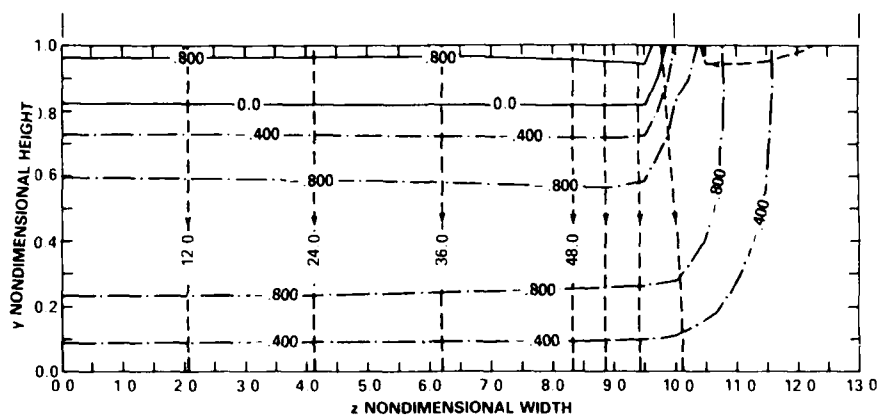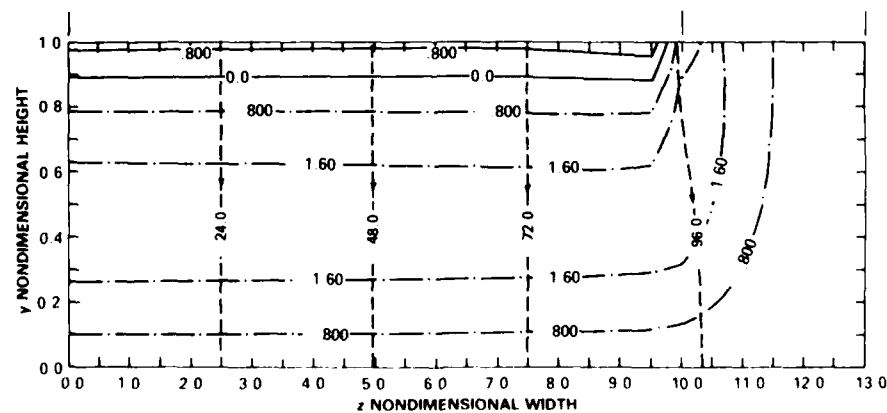 $M = 10$ will cause a progressive shift of the current from the radial gap of length L to the region near the free surface. Figures 10a through 10c present contour plots for $M = 10$ and $h_o = -20$, -60, and -100.

The nondimensional fluid velocity profiles for $M = 2$ and $M = 10$ for negative h_o values show in general positive flow, in the positive x-direction, in the region of the channel near the moving wall because of irreversible, viscous friction effects between the wall and the fluid. Away from the close proximity of the moving wall the fluid velocity profiles are negative, in the minus x-direction, and approach zero in the vicinity of the bottom stationary wall. The fluid in the region between $10 \leq z \leq 13$ and $0 \leq y \leq 1$ in general moves in the negative x-direction because of $\vec{j} \times \vec{B}_o$ body forces caused by the currents leaving the side wall to the tip of the moving wall interacting with the axial magnetic field $\vec{B}_o$, and/or the viscous interaction with the fluid near the center region of the channel moving in the minus x-direction. The nondimensional fluid velocity moves much faster in the negative x-direction when M is changed from 2 to 10 because of the increased $\vec{j} \times \vec{B}_o$ body forces.

The nondimensional induced magnetic field contours for $M = 2$ and $M = 10$ are very similar in magnitude and position for the same negative h_o except in the side region $10 \leq z \leq 13$ and $0 \leq y \leq 1$. As M increases from $M = 2$ to 10 for the same negative h_o contour lines of $h(y,z)$ leave the right side wall and approach the tip of the top moving wall. In each figure of $h(y,z)$ for $M = 2$ there is one contour line near the free surface that leaves the stationary wall and moves to the tip of the moving wall.

Comparing Figs. 5a through 10c, it is evident that the results for $M = 2$, 10 and $h_o = \pm 20, \pm 40, \pm 60, \pm 80$, and ± 100 are not symmetrical about $h_o = 0$ for the same M value. For $h_o = 0$, $j_y < 0$ for $0 \leq z \leq 9.5$ and $j_y > 0$ for $9.5 \leq z \leq 13$. As h_o increases from 0 to 100, we are adding a positive j_y everywhere. Thus, the original and added current density cancel for $0 \leq z \leq 9.5$ and reinforce for $9.5 \leq z \leq 13$. As h_o becomes negative from 0 to -100, we are adding a negative j_y everywhere. Thus the original and added current density reinforce for $0 \leq z \leq 9.5$ and cancel for $9.5 \leq z \leq 13$. As a result the value of $|j_y|$ for $0 \leq z \leq 9.5$ is larger for $h_o = -20$, than for $h_o = +20$, and the same M. Similarily, the current densities near the free surface are smaller for $h_o = -20$ than for $h_o = +20$ and the same M.

For both $h_o = \pm 20$, there is a shift of current density from the radial gap to the free surface region as M increases from 2 to 10. However, this shift is not as strong for a given change in M for $h_o = -20$, as it is for $h_o = +20$, because the potential difference must overcome the tendency for current to flow from the stationary to the moving wall near the free surface.

These same general principles apply for the higher h_o values at the same M value. Table 2 shows for comparison the values calculated for simple one-dimensional, nondimensional Couette flow in an axial magnetic field with no nondimensional pressure gradient.
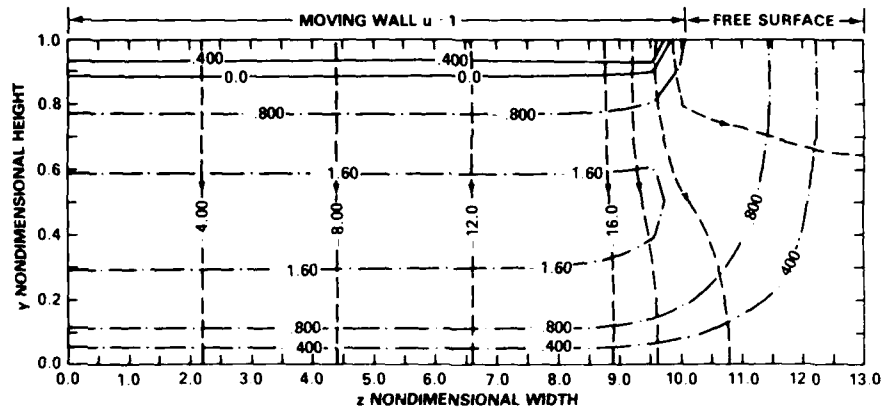
Fig. 10a. $M = 10$, $h_0 = -20$
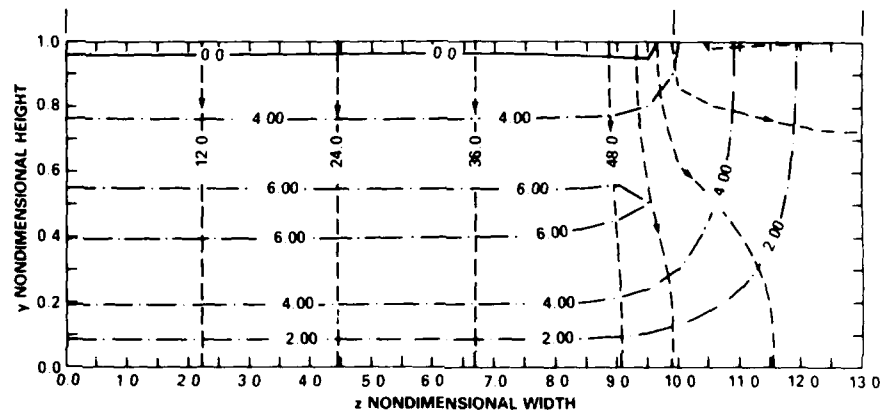
Fig. 10b. $M = 10$, $h_0 = -60$
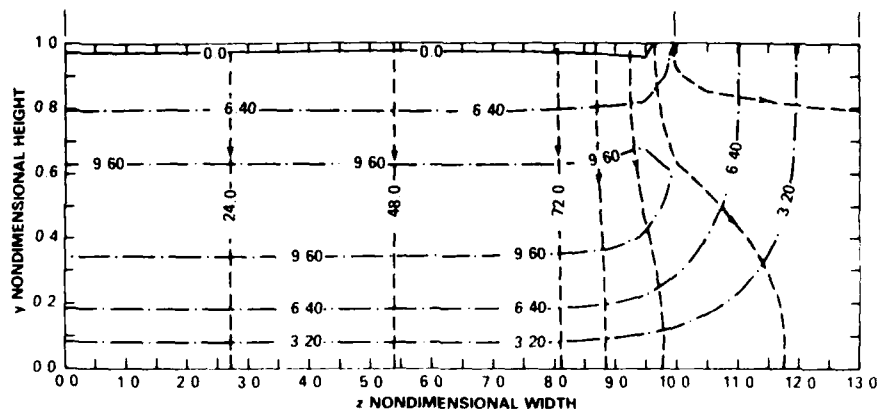
Fig. 10c. $M = 10$, $h_0 = -100$

Fig. 10. Nondimensional velocity contours $u(y,z)$ and nondimensional current density stream function $h(y,z)$ for Hartmann number $M = 10$ and $h_0 = -20$, -60, and -100.

Table 2. One-dimensional Couette flow values for axial magnetic field

Hartmann No.	h_o	$u(.75)$	$u(.50)$	$u(.25)$	u_{min}	y_{min}
	-20	+0.37	0.0	-0.13	-0.13	0.25
	-40	-0.01	-0.50	-0.51	-0.57	0.38
$M = 2$	-60	-0.39	-1.00	-0.89	-1.04	0.42
	-80	-0.77	-1.50	-1.27	-1.53	0.44
	-100	-1.15	-2.00	-1.65	-2.03	0.45
	-20	-1.15	-2.00	-1.65	-2.03	0.45
	-40	-3.05	-4.50	-3.65	-4.51	0.48
$M = 10$	-60	-4.95	-7.00	-5.55	-7.01	0.48
	-80	-6.85	-9.50	-7.35	-9.51	0.49
	-100	-8.75	-12.00	-9.25	-12.01	0.49

For reference, Appendix C presents much more detailed contour plots for Figs. 5 through 10. The figures are not presented as composite plots of the contours for nondimensional velocity and nondimensional current density stream function, as they are here, but as single plots for each case.

COMPARISON OF NUMERICAL PARAMETERS FOR ONE-DIMENSIONAL AND TWO-DIMENSIONAL FLOW

Tables 3 to 7 are presented for various numerical parameters for both one-dimensional (see Appendix B) and two-dimensional Couette flow in an external homogeneous axial magnetic field $\vec{B}_o$ with no pressure gradient along the channel $\partial P / \partial x = 0$.

For the two-dimensional case the nondimensional length of the perfectly conducting, moving wall from the center of the wall to the end is $b = 10$, and the nondimensional free surface length is $a = 3$, (see Fig. 2). For the one-dimensional case the perfectly conducting moving wall nondimensional length from the center of the wall to the end is $b = 10$. *We have compared the two cases, both having the moving wall of nondimensional length* b = 10, *to determine the end effects in the two-dimensional case.* The one-dimensional case has no end effects.

Each of Tables 3 to 7 is for a specific Hartmann number M (where M can run through the values 2, 4, 6, 8 and 10) and extends through a range of h_o values where $h_o = -100$, $-80, -60, -40, -20, 0, 20, 40, 60, 80, 100$. The quantity h_o is a measure of the load current (see Eq. 16.2). The symbol in each table for ϕ_o represents the two-dimensional, nondimensional potential at the perfectly conducting moving wall $\phi_o = \phi(y = 1, z)$ for $-b \le y \le b$. The value ϕ_{o1D} is the corresponding one-dimensional, nondimensional potential. The symbol P_J is the nondimensional Joulean dissipation per unit nondimensional length (Δx) in the channel for the two-dimensional case. P_{J1D} is the corresponding nondimensional Joulean dissipation in the one-dimensional case. The symbol P_μ is the nondimensional viscous dissipation in the two-dimensional case per unit nondimensional length, and $P_{\mu 1D}$ is the corresponding one-dimensional case.

Comparison of the numerical data for the one-dimensional and two-dimensional cases in Tables 3 to 7 leads to the following conclusions. For every instance, the relationship $|\phi_o| < |\phi_{o1D}|$ holds for the nondimensional potentials in the two cases. The one-dimensional solution assumes that all current flows across the magnetic field lines and thus is a current path with a large resistance. In the two-dimensional case, a fraction of the current flows along the magnetic field lines near the free surface and enters the moving wall near the edge at $z = b$. This path has a lower resistance so that the overall potential difference is smaller than the one-dimensional case. Also, the fraction of the total current near the free surface increases as M increases so $|\phi_{o1D} - \phi_o|$ increases as M increases.

Nondimensional Joulean power losses for no load current $h_o = 0$ are $P_{J1D} = 0$ for the one-dimensional case for $M = 2, 4, 6, 8$ and 10. For the same values of M, P_J extends from 0.28 through -2.74 for the two-dimensional case. In the two-dimensional case, the weak nondimensional Joulean power losses are from the weak eddy current when there is

Table 3. Numerical data for Hartmann number $M = 2$

M	h_o	ϕ_o	ϕ_{o1D}	P_J	P_{J1D}	P_μ	$P_{\mu1D}$
2	-100	5.962	6.167	1,802.1	2,000	650.9	686.7
2	- 80	4.674	4.833	1,153.5	1,280	424.1	446.7
2	- 60	3.385	3.500	o49.1	720	247.7	260.0
2	- 40	2.097	2.167	288.7	320	121.7	126.7
2	- 20	0.808	0.833	72.44	80	46.01	46.67
2	0	-0.481	-0.500	0.2793	0	20.71	20.0
2	20	1.769	-1.833	72.23	80	45.77	46.67
2	40	-3.058	-3.167	288.3	320	121.2	126.7
2	60	-4.346	-4.500	648.4	720	247.0	260.0
2	80	-5.635	-5.833	1,152.7	1,280	423.2	446.7
2	100	-6.924	-7.167	1,801.1	2,000	649.7	686.7

Table 4. Numerical data for Hartmann number $M = 4$

M	h_o	ϕ_o	ϕ_{o1D}	P_J	P_{J1D}	P_μ	$P_{\mu1D}$
4	-100	5.072	5.333	1,830.2	2,000	2,488.6	2,686.7
4	- 80	3.962	4.167	1,170.8	1,280	1,601.3	1,726.7
4	- 60	2.852	3.000	658.2	720	910.9	980.0
4	- 40	1.742	1.833	292.3	320	417.3	446.7
4	- 20	0.632	0.667	73.11	80	120.7	126.7
4	0	-0.478	-0.500	0.719	0	20.92	20.0
4	20	-1.587	-1.667	75.07	80	118.0	126.7
4	40	-2.697	-2.833	296.2	320	412.1	446.7
4	60	-3.807	-4.000	664.0	720	903.0	980.0
4	80	-4.917	-5.167	1,178.6	1,280	1,590.8	1,726.7
4	100	-6.027	-6.333	1,840.0	2,000	2,475.5	2,686.7

Table 5. Numerical data for Hartmann number, $M = 6$

M	h_o	ϕ_o	ϕ_o1D	P_J	P_{J1D}	P_μ	$P_{\mu1D}$
6	-100	5.743	6.167	1,945.4	2,000	5,394.2	6,020
6	- 80	4.500	4.833	1,242.2	1,280	3,463.6	3,860
6	- 60	3.257	3.500	696.1	720	1,961.0	2,180
6	- 40	2.014	2.167	307.3	320	886.4	980
6	- 20	0.771	0.833	75.68	80	239.8	260
6	0	-0.472	-0.500	1.257	0	21.164	20
6	20	-1.715	-1.833	84.04	80	230.6	260
6	40	-2.958	-3.167	324.0	320	868.0	980
6	60	-4.201	-4.500	721.2	720	1,933.4	2,180
6	80	-5.444	-5.833	1,275.6	1,280	3,426.8	3,860
6	100	-6.687	-7.167	1,987.2	2,000	5,348.2	6,020

Table 6. Numerical data for Hartmann number $M = 8$

M	h_o	ϕ_o	ϕ_o1D	P_J	P_{J1D}	P_μ	$P_{\mu1D}$
8	-100	6.735	7.417	2239.9	2000	9162.8	10,686.7
8	- 80	5.295	5.833	1426.1	1280	5880.4	6846.7
8	- 60	3.855	4.250	795.5	720	3325.0	3860.0
8	- 40	2.415	2.667	347.9	320	1496.8	1726.7
8	- 20	0.975	1.083	83.38	80	395.5	446.7
8	0	-0.465	-0.500	1.940	0	21.397	20.0
8	20	-1.905	-2.083	103.58	80	374.3	446.7
8	40	-3.345	-3.667	388.3	320	1454.3	1726.7
8	60	-4.785	-5.250	856.1	720	3261.4	3860.0
8	80	-6.225	-6.833	1506.9	1280	5795.5	6846.7
8	100	-7.665	-8.417	2340.9	2000	9056.7	10,686.7

Table 7. Numerical data for Hartmann number $M = 10$

M	h_o	ϕ_o	ϕ_{o1D}	P_J	P_{J1D}	P_μ	$P_{\mu1D}$
10	-100	7.788	8.833	2,816.6	2,000	13,552.4	16,686.7
10	- 80	6.139	6.967	1,788.3	1,280	8,697.1	10,686.7
10	- 60	4.490	5.100	992.8	720	4,916.3	6,020.0
10	- 40	2.842	3.233	430.1	320	2,210.2	2,686.7
10	- 20	1.193	1.367	100.1	80	578.6	686.7
10	0	-0.456	-0.500	2.736	0	2,1.650	20.0
10	20	-2.104	-2.367	138.2	80	539.3	686.7
10	40	-3.753	-4.233	506.4	320	2,131.5	2,686.7
10	60	-5.401	-6.100	1,107.3	720	4,798.2	6,020.0
10	80	-7.050	-7.967	1,941.0	1,280	8,539.6	10,686.7
10	100	-8.699	-9.833	3,007.4	2,000	13,355.6	16,686.7

no load current. For a load current, $h_o \neq 0$ when $M = 2$, 4 and 6, the following relationship is found to be true: $P_J < P_{J1D}$. The one-dimensional solution assumes $0 \leq |z| \leq b$, but in the two-dimensional case $0 \leq |z| \leq a + b$, which allows currents to fringe into the end regions giving a smaller average y-component current density j_y and smaller P_J. For $h_o \neq 0$ and $M = 8$ and 10, the relationship $P_{J1D} < P_J$ is found to hold. In the two-dimensional case a progressively larger fraction of current is concentrated near the free surface and rotor edge. As $|j|$ becomes locally large $j_y^2 + j_z^2$ becomes very large and this extra contribution is much larger than the reduction elsewhere in the channel.

For the nondimensional viscous dissipation when the load current is not zero $h_o \neq 0$, the relationship $P_\mu < P_{\mu 1D}$ is found to hold. The one-dimensional velocity consists of the linear velocity y plus a parabola driven by the body force $j_y B_o$. In $P_{\mu 1D}$ (Appendix B, Eq. B-11) the $2b$ is due to the linear velocity $u = y$ and $M^2 h_o^2 / 6b$ is due to the parabola. In the two-dimensional case as M increases, an increasing fraction of the current flows along the field lines near the free surface. This current produces no velocity except near the moving wall edge where it must cross field lines to enter the wall. Thus in the two-dimensional case, the parabola near $z = 0$ is much smaller than in the one-dimensional case, and P_μ is concentrated near the edge of the moving wall.

The one-dimensional variables calculated and presented in this section were derived in Appendix B, but are presented here for continuity of presentation. The nondimensional y-component of current density is

$$j_{y1D} = \frac{h_o}{Mb} \quad ,$$

(26)

and the nondimensional Joulean power loss per unit nondimensional length is given by

$$P_{J1D} = \frac{2h_o^2}{b} \quad .$$

(27)

The nondimensional velocity is

$$u_{1D} = y + \left(\frac{Mh_o}{2b}\right) y (1 - y) \quad ,$$

(28)

and the nondimensional viscous power loss per unit nondimensional length is given by

$$P_{\mu 1D} = 2b + \frac{M^2 h_o^2}{6b} \quad .$$

(29)

The nondimensional potential in the channel has the following form

$$\phi_{1D} = -\frac{y^2}{2} - \left(\frac{Mh_o}{2b}\right)\left(\frac{y^2}{2} - \frac{y^3}{3}\right) - \left(\frac{h_o}{Mb}\right) y \quad ,$$

(30)

and the nondimensional potential at the moving wall is

$$\phi_{o1D} = -\frac{1}{2} - \left(\frac{h_o}{b}\right)\left(\frac{1}{M} + \frac{M}{12}\right) \quad , \quad \text{where } (\phi_{1D}(y = 1) = \phi_{o1D}).$$

(31)

(Note: all the variables in these equations were defined earlier in the report.)

31

CONCLUSIONS

Numerical data were presented for the nondimensional velocity profiles $u(y,z)$ and nondimensional induced magnetic field $h(y,z)$ for an incompressible conducting fluid in a two-dimensional magnetohydrodynamic channel in an axial homogeneous, external magnetic field (Couette flow). The top wall of the channel was a moving, perfectly conducting wall with insulating free surfaces in both top corners. The bottom stationary wall and the right and left stationary sidewalls were also perfect conductors. A current load was simulated between the top and bottom conducting walls by applying an external potential to the top wall. Three cases for Hartmann numbers $M = 2$ and 10 were studied for a load current moving from bottom to top wall ($h_o = 20, 60, 100$), top to bottom wall ($h_o = -20, -60, -100$) and no load current ($h_o = 0$). The data were calculated for a rectangular channel where the radial gap was chosen as length L, each axial free surface gap as $3L$, and the length of the moving wall as $20L$. In this work the nondimensional pressure gradient $\partial P/\partial x$ was set equal to zero. Thus, the fluid motion was due only to the drag of the moving wall and the Lorentz body force.

These three sets of data supported the concept that the radial gap and the free surface region represent electrical resistances in parallel between the stationary, perfectly conducting walls and the moving, perfectly conducting wall. The data also showed that the resistance of the radial gap increases as M^2 while that of the free surface region increases by approximately $M^{1/2}$. Thus as M increases, the division of current shifts to the free surface region and the current density in the radial gap decreases as M^{-1}.

Numerical data for one-dimensional Couette flow with no pressure gradient in an axial magnetic field having no end effects were presented and compared with numerical data for two-dimensional Couette flow.

On the basis of the theory and the range of data computed, a number of conclusions can be drawn:

1. For every case studied the absolute value of the nondimensional potential at the perfectly conducting moving wall of the two-dimensional case $|\phi_o|$ is less than the corresponding nondimensional potential $|\phi_{o1D}|$ in the one-dimensional case. The fraction of the total current near the free surface in the two-dimensional case increases as M increases, so $|\phi_{o1D} - \phi_o|$ increases as M increases.

2. For the range of data computed, with no load current across the channel, $h_o = 0$, the nondimensional Joulean power losses per nondimensional length P_{J1D} in the one-dimensional case are zero. The corresponding Joulean losses per nondimensional length P_J for the two-dimensional case extend from 0.28 at $M = 2$ to 2.74 for $M = 10$. The power losses in the two-dimensional case are caused by the weak eddy currents. For load currents across the channel, the power relationship $P_J < P_{J1D}$ holds when $h_o \neq 0$: for $M = 2, 4$ and 6 and $P_{J1D} < P_J$ holds for $M = 8$ and 10.

3. It was found that the nondimensional viscous dissipation per nondimensional length P_μ is always less than the corresponding one-dimensional case for the range of data computed.

These results show that it is necessary to model the magnetohydrodynamic flow in a current collector by a two-dimensional model, as opposed to a one-dimensional model, to obtain a fundamental understanding of the flow profile, current density distribution in the liquid metal, and viscous and Joulean power losses.

APPENDIX A
MATHEMATICAL SOLUTION FOR RECTANGULAR CHANNEL WITH FOUR PERFECTLY CONDUCTING CONNECTED WALLS, ONE A MOVING WALL

The problem discussed herein consists of a rectangular channel in a homogeneous, external, transverse magnetic field $\vec{B_o}$ with four thin perfectly conducting walls (see Fig. A-1). The perfectly conducting wall at the top of the figure is assumed to move with a velocity $u = u(z = z_o)$. It should be carefully noted that the coordinate system is in a different position in regard to the rectangular channel than is the coordinate system in the text of this report.

The mathematical problem developed in this Appendix formed a basis for some of the theoretical development of the more complex model presented in the text of the report. The major fault of the mathematical model presented herein is that the four perfectly conducting walls are connected so that there are no insulating, free surface gaps between the perfectly conducting moving wall and the perfectly conducting left and right side stationary walls as are in the rectangular channel mathematical model presented in the text of the report. Thus in the model in this Appendix, it is impossible to apply an external potential ϕ_o to the moving walls of the channel. This results in a severe limitation to the mathematical model since current collectors carry a heavy load current.

We were able to obtain series solutions for the flow velocity, induced magnetic field, total current, and voltages in the channel. These solutions are presented in the Appendix to provide a continuity and theoretical background to the development of the theoretical mathematical model presented in the text of the report. Numerical computer results for the problem herein were not obtained.

The mathematical problem is made more tractable by transforming the two dimensional, steady, incompressible, viscous magnetohydrodynamic flow partial differential equations into nondimensional form using the notation of the Hughes and Young.[10] They worked the similar rectangular channel problem where all four connected, perfectly conducting walls are stationary.

The nondimensional variables are defined as

$$k = \frac{z_o}{y_o} \qquad\qquad u^* = \frac{u\,\mu_f}{y_o^2 \left(\partial P / \partial x\right)} \tag{A-1.1}$$

$$y^* = \frac{y}{y_o} \qquad\qquad H^* = \frac{H_x}{y_o^2 \left(\partial P / \partial x\right)\sqrt{\sigma / \mu_f}} \tag{A-1.2}$$

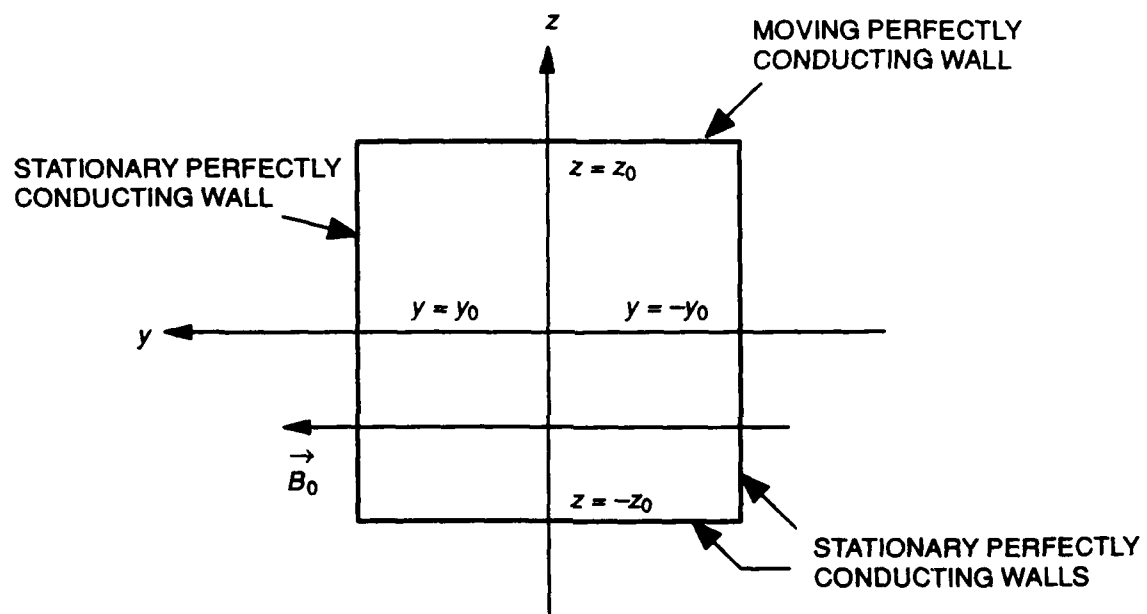$$z^* = \frac{z}{z_o} \qquad\qquad M = y_o B_o \sqrt{\sigma / \mu_f} \tag{A-1.3}$$

34

Fig. A-1. Channel with four perfectly conducting walls.

35

where the dimensional variables (without superscript *) have the following meaning:

y_o = one half width of channel, (A-1.4)

z_o = one half height of channel, (A-1.5)

k = z_o/y_o = aspect ratio, (A-1.6)

μ_f = viscosity of fluid in channel, (A-1.7)

$\partial P/\partial x$ = constant pressure gradient in x-direction, A-1.8)

σ = conductivity of fluid, (A-1.9)

B_o = magnitude of the homogeneous external magnetic field, A-1.10)

u = dimensional fluid velocity, (A-1.11)

H_x = dimensional induced magnetic field. (A-1.12)

The nondimensional magnetohydrodynamic equations for $u^*(y^*,z^*)$ and $h^*(y^*,z^*)$ are

$$\frac{\partial^2 H_x^*}{\partial y^{*2}} + \frac{\partial^2 H_x^*}{\partial z^{*2}} + M\frac{\partial u^*}{\partial y^*} = 0 \qquad (A\text{-}2.1)$$

and

$$\frac{\partial^2 u^*}{\partial y^{*2}} + \frac{\partial^2 u^*}{\partial z^{*2}} + M\frac{\partial H_x^*}{\partial y^*} = 1 \ , \qquad (A\text{-}2.2)$$

where the appropriate boundary values must be satisfied. The well-known assumed nondimensional solutions have the following form [10]:

$$u^* = \mathop{u^*}_{k\to\infty} + \sum_{n=0}^{\infty} u_n^*(z^*)\cos\lambda_n^* y^* \qquad (A\text{-}3.1)$$

$$H_x^* = \mathop{H_x^*}_{k\to\infty} + \sum_{n=0}^{\infty} H_n^*(z^*)\sin\lambda_n^* y^* \ , \qquad (A\text{-}3.2)$$

where

$$u_n^*(z^*) = C_1 \sinh P_1^* z^* + C_2 \cosh P_2^* z^* + C_3 \sinh P_1^* z^* + C_4 \cosh P_2^* z^* \ , \qquad (A\text{-}3.3)$$

$$P_1^*, P_2^* = \sqrt{\lambda_n^{*2} \pm j\lambda_n^* M}$$

$$= \sqrt{\frac{\lambda_n^*}{2}}\left(\sqrt{\sqrt{M^2 + \lambda_n^{*2}} + \lambda_n^*} \pm j\sqrt{\sqrt{M^2 + \lambda_n^{*2}} - \lambda_n^*}\right) \qquad (A\text{-}3.4)$$

$$P_1^*, P_2^* = r_n^* \pm j\, s_n^* \qquad (A\text{-}3.5)$$

$$\lambda_n^* = \frac{(2n+1)\pi}{2} \qquad (A\text{-}3.6)$$

$$\mathop{u^*}_{k\to\infty} = \frac{1}{M^2}\left(\frac{\cosh My^*}{\cosh M} - 1\right) \qquad (A\text{-}3.7)$$

$$\mathop{H_x^*}_{k\to\infty} = \frac{1}{M}\left(y^* - \frac{\sinh My^*}{M\cosh M}\right) \qquad (A\text{-}3.8)$$

The particular solutions, $u^*_{k \to \infty}$ and $H^*_{x_{k \to \infty}}$, are the solution to the flow problem between two perfect conducting infinite plates. Equations A-3.1 and A-3.2, transform Eqs. A-2.1 and A-2.2 into ordinary differential equations.

The solution for u_n^* is assumed unsymmetrical with respect to z^* and was thus expressed as a combination of even and odd functions

$$u_n^* = C_1 \cosh\left(r_n^* + js_n^*\right)z^* + C_2 \cosh\left(r_n^* - js_n^*\right)z^* +$$
$$C_3 \sinh\left(r_n^* + js_n^*\right)z^* + C_4 \sinh\left(r_n^* - js_n^*\right)z^* \ , \qquad \text{(A-4.1)}$$

or simply as

$$u_n^*(z^*) = A_n \sinh\left(r_n^* z^*\right)\sin\left(s_n^* z^*\right) + B_n \cosh\left(r_n^* z^*\right)\cos\left(s_n^* z^*\right) +$$
$$C_n \sinh\left(r_n^* z^*\right)\cos\left(s_n^* z^*\right) + D_n \cosh\left(r_n^* z^*\right)\sin\left(s_n^* z^*\right) \qquad \text{(A-4.2)}$$

where
$$A_n = j\left(C_1 - C_2\right) \ ,$$
$$B_n = \left(C_1 + C_2\right) \ ,$$
$$C_n = \left(C_3 + C_4\right) \ ,$$
$$D_n = j\left(C_3 - C_4\right) \ . \qquad \text{(A-4.3)}$$

The solution for $H_n^*(z^*)$ is also assumed unsymmetrical with respect to z^* and was expressed as

$$H_n^*(z^*) = \frac{1}{M\lambda_n^*}\left[\left(P_1^{*2} - \lambda_n^{*2}\right)C_1 \cosh P_1^* z^* + \left(P_2^{*2} - \lambda_n^{*2}\right)C_2 \cosh P_2^* z^* \right.$$
$$\left. + \left(P_1^{*2} - \lambda_n^{*2}\right)C_1 \cosh P_1^* z^* + \left(P_2^{*2} - \lambda_n^{*2}\right)C_2 \cosh P_2^* z^*\right] \qquad \text{(A-5.1)}$$

$$H_n^*(z^*) = \left[j\,C_1 \cosh P_1^* z^* - j\,C_2 \cosh P_2^* z^* + j\,C_3 \sinh P_1^* z^* - j\,C_4 \sinh P_2^* z^*\right] \qquad \text{(A-5.2)}$$

where
$$P_1^{*2} - \lambda_n^{*2} = j\left(\lambda_n^* M\right), \quad \text{and} \quad P_2^{*2} - \lambda_n^{*2} = -j\left(\lambda_n^* M\right) \ , \qquad \text{(A-5.3)}$$

or more simply as

$$H_n^*(z^*) = L_n \sinh\left(r_n^* z^*\right)\sin\left(s_n^* z^*\right) - A_n \cosh\left(r_n^* z^*\right)\cos\left(s_n^* z^*\right)$$
$$+ C_n \cosh\left(r_n^* z^*\right)\sin\left(s_n^* z^*\right) - D_n \sinh\left(r_n^* z^*\right)\cos\left(s_n^* z^*\right) \qquad \text{(A-5.4)}$$

The following boundary conditions must be satisfied for this specific problem

$$1 = u^*_{z^* \to \infty} + \sum_{n=0}^{\infty} u_n'(z^* = k)\cos\lambda_n^* y^* \ , \qquad \text{(A-6.1)}$$

$$0 = \underset{z^* \to \infty}{u^*} + \sum_{n=0}^{\infty} u_n^*(z^* = -k) \cos\lambda_n^* y^* \ , \tag{A-6.2}$$

$$0 = \frac{\partial H^*(y^*, z^* = k)}{\partial z^*} = -\sum_{n=0}^{\infty} \lambda_n^* \frac{dH_n(z^* = k)}{dz^*} \cos\lambda_n^* y^* \ , \tag{A-6.3}$$

$$0 = \frac{\partial H^*(y^*, z^* = -k)}{\partial z^*} = -\sum_{n=0}^{\infty} \lambda_n^* \frac{dH_n(z^* = -k)}{dz^*} \cos\lambda_n^* y^* \ . \tag{A-6.4}$$

Equations A-6.1 and A-6.2 show the no-slip boundary conditions on the conducting fluid that must be satisfied along the moving wall at $z^* = k$ and the stationary wall at $z^* = -k$. Equations A-6.3 and A-6.4 show that the y-component of the current density must be zero along these perfectly conducting walls at $z^* = k$ and $-k$, since it is well known that for a perfect conductor the tangential component of the current density must be zero or infinite currents will flow in the conductor.

The form of the mathematical solution for $u^*(y^*, z^*)$ and $j_z^*(y^*, z^*)$ guarantees that

$$u^*(y^* = \pm 1, z^*) = 0, \quad \text{and} \tag{A-7.1}$$

$$j_z(y^* = \pm 1, z^*) = 0 \tag{A-7.2}$$

on both the left and right wall. Substitution of the expressions for $\underset{k \to \infty}{u^*}$, $\underset{k \to \infty}{u_n^*}$, H_x^*, and H_n^*, derived previously in this report, into the boundary conditions of Eqs. A-6.1 to A-6.4 determines the coefficients, which are

$$A_n = E_n \left[r_n^* \cosh\left(r_n^* k\right) \sin\left(s_n^* k\right) + s_n^* \sinh\left(r_n^* k\right) \cos\left(s_n^* k\right) \right] \ , \tag{A-8.1}$$

$$B_n = E_n \left[r_n^* \sinh\left(r_n^* k\right) \cos\left(s_n^* k\right) - s_n^* \cosh\left(r_n^* k\right) \sin\left(s_n^* k\right) \right] \ , \tag{A-8.2}$$

$$C_n = F_n \left[r_n^* \cosh\left(r_n^* k\right) \cos\left(s_n^* k\right) - s_n^* \sinh\left(r_n^* k\right) \sin\left(s_n^* k\right) \right] \ , \tag{A-8.3}$$

$$D_n = F_n \left[r_n^* \sinh\left(r_n^* k\right) \sin\left(s_n^* k\right) + s_n^* \cosh\left(r_n^* k\right) \cos\left(s_n^* k\right) \right] \ , \tag{A-8.4}$$

where

$$E_n = \frac{2(-1)^n \left(2 + M^2 + \lambda_n^{*2}\right)}{\lambda_n^* \left(M^2 + \lambda_n^{*2}\right) \left[r_n^* \sinh\left(2r_n^* k\right) - s_n^* \sin\left(2s_n^* k\right)\right]} \ ,$$

$$F_n = \frac{2(-1)^n}{\lambda_n^* \left[r_n^* \sinh\left(2r_n^* k\right) + s_n^* \sin\left(2s_n^* k\right)\right]} \ .$$

APPENDIX B
ONE–DIMENSIONAL COUETTE FLOW
WITH AN AXIAL MAGNETIC FIELD,
APPLIED EXTERNAL POTENTIAL, AND NO PRESSURE GRADIENT

The problem discussed herein is not commonly reported in the literature, and is presented here for continuity of presentation. One-dimensional Couette flow with an externally applied potential in a constant homogeneous axial magnetic field and no pressure gradient is shown in Fig. B-1. The nondimensional externally applied potential of the moving, perfectly conducting infinite plate is ϕ_0, and the nondimensional potential of the stationary, perfectly conducting infinite plate is zero ($\phi = 0$). The axial, constant, homogeneous externally applied magnetic field $\vec{B}$ is in the z-direction. The conductivity and viscosity of the liquid metal are σ and μ_f, respectively. The nondimensional velocity of the liquid metal $u(y)$ is in the x-direction. There are no plate end effects on the fluid flow since the plates are of infinite length (i.e. $\dfrac{\partial}{\partial z} = 0$, and $j_z = 0$).
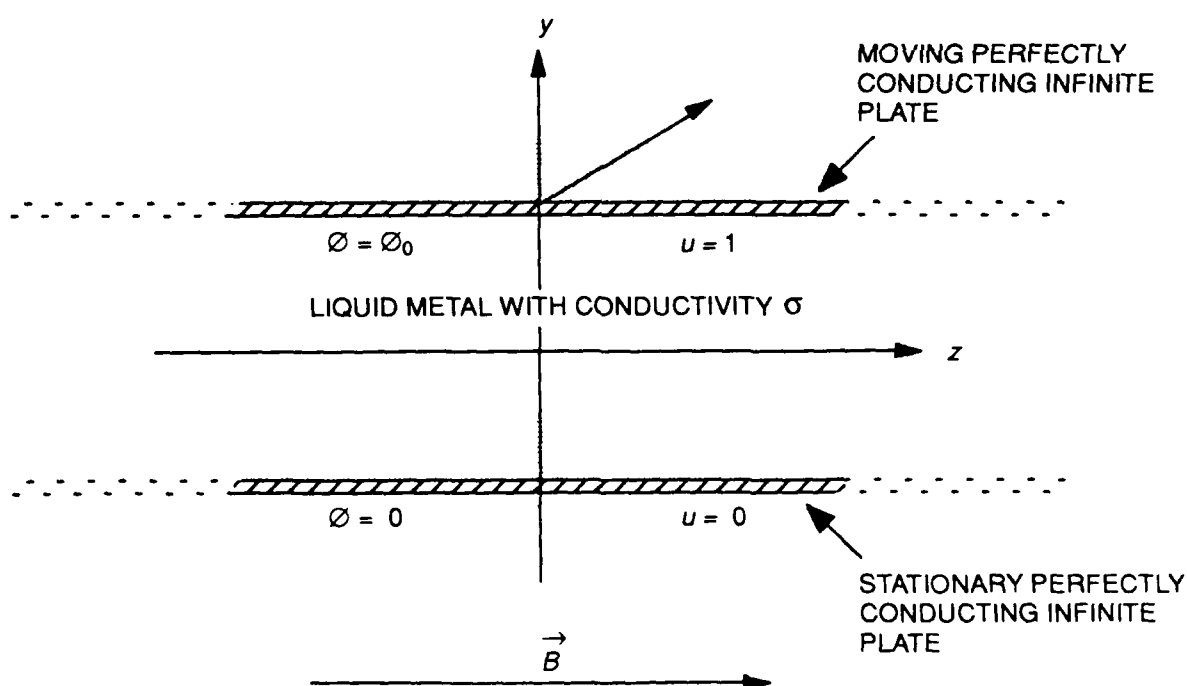
Fig. B-1.   One-dimensional Couette flow with an axial magnetic field

The numerical data calculated for the variables of interest for one-dimensional Couette flow presented here will be compared with the corresponding numerical data for the two-

dimensional Couette flow presented in the text of the report. End effects are important in the two-dimensional Couette flow because of the gaps between the moving, perfectly conducting finite top plate and the perfectly conducting side walls. The two gaps are insulating, stress-free, free surfaces. In the one-dimensional Couette flow, end effects are not incorporated in the derivation. Therefore, it would be expected that the two sets of data should be similar only at low Hartmann numbers M.

Referring to the two-dimensional magnetohydrodynamic equations in the text of the report, the governing system of nondimensional ordinary differential equations for one-dimensional Couette flow with a constant, homogeneous axial magnetic field is

$$M^{-2}\frac{d^2 u(y)}{dy^2} + j_y(y) = 0 , \tag{B-1.1}$$

$$j_y(y) = \frac{-d\phi(y)}{dy} - u(y) , \tag{B-1.2}$$

$$\frac{d j_y(y)}{dy} = 0 \tag{B-1.3}$$

The boundary conditions for the nondimensional velocity u and nondimensional potential ϕ for the moving, perfectly conducting top wall are

$$u(y=1) = 1 , \qquad\qquad \phi(y=1) = \phi_o , \tag{B-2.1}$$

and the stationary, perfectly conducting bottom wall are

$$u(y=0) = 0 , \qquad\qquad \phi(y=0) = 0 . \tag{B-2.2}$$

The z-component of the current density j_z is equal to zero ($j_z = 0$).

From Eqs. B-1.2 and B-1.3, it is noted that

$$\frac{d^2\phi(y)}{dy^2} = -\frac{du(y)}{dy} . \tag{B-2.3}$$

The mathematical solutions to the above Couette problem for the liquid metal nondimensional velocity $u(y)$ the nondimensional potential in the fluid $\phi(y)$, and the y-component of the nondimensional current density j_y are

$$u(y) = y - \frac{3(2\phi_o + 1)y(1 - y)}{1 + 12M^{-2}} , \tag{B-4.1}$$

$$\phi(y) = -\frac{y^2}{2} - \left(\frac{Mh_o}{2b}\right)\left(\frac{y^2}{2} - \frac{y^3}{3}\right) - \left(\frac{h_o}{Mb}\right)y , , \tag{B-4.2}$$

$$j_y = -\left(\frac{12\phi_o + 6}{12 + M^2}\right) , \tag{B-4.3}$$

where h_o is defined in Eq. B-7.

A magnetic stream function can be defined by $h(z)$ where $h(z)$ is a linear function of z (i.e. constant multiplied by z). The j_y and j_z can be expressed as

$$j_y = -\frac{6(2\phi_o + 1)}{M^2 + 12} = M^{-1}\frac{\partial h(z)}{\partial z} = \frac{h_o}{Mb} \; , \tag{B-5.1}$$

$$j_z = 0 = M^{-1}\frac{\partial h(z)}{\partial y} \; . \tag{B-5.2}$$

Then $h(z)$ has the following form

$$h_z = -\frac{6(2\phi_o + 1)z}{M + 12M^{-1}} \; . \tag{B-6}$$

The total dimensionless current from the stationary wall to the moving wall is

$$I = 2(\Delta x)\int_0^b j_y(1,z)\,dz = 2(\Delta x)\,M^{-1}h_o \; . \tag{B-7}$$

Therefore h_o can be expressed as

$$h(z) = -\frac{6(2\phi_o + 1)z}{M + 12M^{-1}} \; . \tag{B-8}$$

where b is the length of a finite plate in the z–direction from the center. From Eq. B-8 the nondimensional potential of the top plate $\phi_o(y = 1) = \phi_o$ is

$$\phi_o = -\frac{1}{2} - \frac{h_o}{12b}(M + 12M^{-1}) \; . \tag{B-9}$$

The nondimensional velocity $u(y)$ in terms of h_o is

$$u(y) = y + \frac{Mh_o}{2b}\,y(1 - y) \; , \tag{B-10}$$

Using Eq. B-10, the total viscous dissipation per nondimensional unit length in the x–direction for plates of length $2b$ is

$$P_{\mu\,1D} = \int_{-b}^{b}\int_0^1 \left(\frac{du(y)}{dy}\right)^2 dy\,dz = 2b + \frac{M^2 h_o^2}{6b} \; , \tag{B-11}$$

where $P_{\mu\,1D} = \dfrac{P_{\mu\,1D}^{*}}{\mu_f U_o^2}$.

Also using Eq. B-5, the total Joulean dissipation per nondimensional unit length in the x–direction for plates of length $2b$ is

$$P_{j\,1D} = M^2 \int_{-b}^{b} \int_{0}^{1} j_y^2 \, dy \, dz = \frac{2h_o^2}{b} \, , \tag{B-12}$$

where $P_{j\,1D} = \dfrac{P_{j\,1D}^*}{\mu_f U_o^2}$.

and the superscript (*) represents a dimensional quantity.

To understand the relationship between the nondimensional applied external potential at the moving wall ϕ_o and h_o for the one-dimensional Couette solution, we must remember that a constant h_o represents a constant total current, but a constant $\phi(y = 1) = \phi_o$ represents a potential difference that increases linearly with B_o,

$$\phi_o^* = U_o B_o L \phi_o \tag{B-13}$$

$$h_o = \frac{I^*}{2U_o \sqrt{\sigma \mu_f} \, (\Delta x^*)} \, ,$$

where I^* = total dimensional current from stator to rotor over rotor length $2bL$. The supercript (*) represents a dimensional quantity. The dimensional applied potential to the moving wall ϕ_o^* is

$$\phi_o^* = -\tfrac{1}{2} \, U_o B_o L - \frac{I^*}{2b\left(\Delta x^*\right)\sigma}\left(1 + \frac{M^2}{12}\right) \, . \tag{B-14}$$

Here $-\tfrac{1}{2} \, U_o B_o L$ is the potential difference needed to balance the average of $\vec{u} \times \vec{B}_o$ if u is simple Couette flow, which it is for $I^* = 0$ in the one–dimensional solution.

The resistance of the stagnant liquid metal for plates of length $2bL$ is

$$R^* = \frac{1}{2b\left(\Delta x^*\right)\sigma} \, . \tag{B-15}$$

When $M \ll 1$, the current does not change the velocity profile, so

$$\phi_o^* + \tfrac{1}{2} \, U_o B_o L = -I^* R^* \, . \tag{B-16}$$

42

As the Hartmann number M increases, the electric current produces a body force $j_y^* B_o \hat{x}$ which accelerates the flow so that u deviates from the simple Couette flow $(u(y) = y)$. The change in velocity always produces an induced electric field $-u^* B_o \hat{y}$, which opposes the current. If $j_y > 0$, then $-u^* B_o \hat{y}$ is negative; if $j_y < 0$, then $-u^* B_o \hat{y}$ is positive. Therefore the moving wall and the stationary wall see a resistance which is more than that of stagnant liquid metal

$$R_{eff}^* = R^* \left(1 + \frac{M^2}{12}\right) .$$ (B-17)

We will see that R_{eff}^* actually increases roughly as M because of end currents in the two-dimensional Couette problem in the text of the report. The expression for the nondimensional velocity

$$u(y) = y + \frac{M h_o}{2b} y(1 - y)$$ (B-18)

consists of the linear Couette term y, plus a parabolic term. The maximum and minimum points for $u(y)$, u_m are given by

$$u_m = \frac{1}{2} \left[1 + \frac{b}{M h_o} + \frac{M h_o}{4b}\right] ,$$ (B-19.1)

where $y_m = \frac{1}{2} + \frac{b}{M h_o}$ (B-19.2)

and $\quad M \geq -\frac{2b}{h_o}$ for $h_o < 0$, $M \geq \frac{2b}{h_o}$ for $h_o > 0$. (B-19.3)

where the subscript m represents a maximum or minumum point. For $h_o < 0$, M must have a certain minimum value before a negative velocity will occur. For $h_o > 0$, M must have a minimum before u_{max} is greater than 1. Two typical plots of $u(y)$ versus y are shown in Fig. B-2 for $h_o > 0$ and $h_o < 0$. The values of M are high enough in both cases for a maximum u_{max} for $h_o > 0$, and minimum u_{min} for $h_o < 0$.

Typical values of Couette flow in an axial magnetic field with no pressure gradient $\partial P / \partial x$ are presented in Tables B-1 and B-2. Figure B-3 presents two non-dimensional velocity profiles $u(y)$ versus nondimensional distance between infinite plates y for one-dimensional Couette flow for $h_o = \pm 10$ and Hartmann number $M = 1$. In this case, the Hartmann number M is so low that there are no maximum or minimum points on the profiles.

43
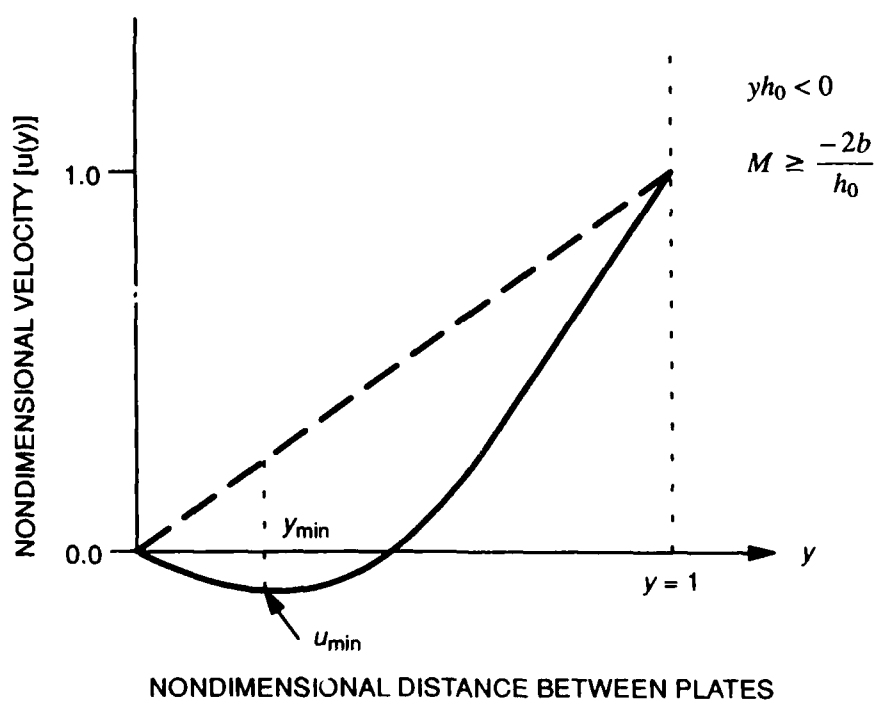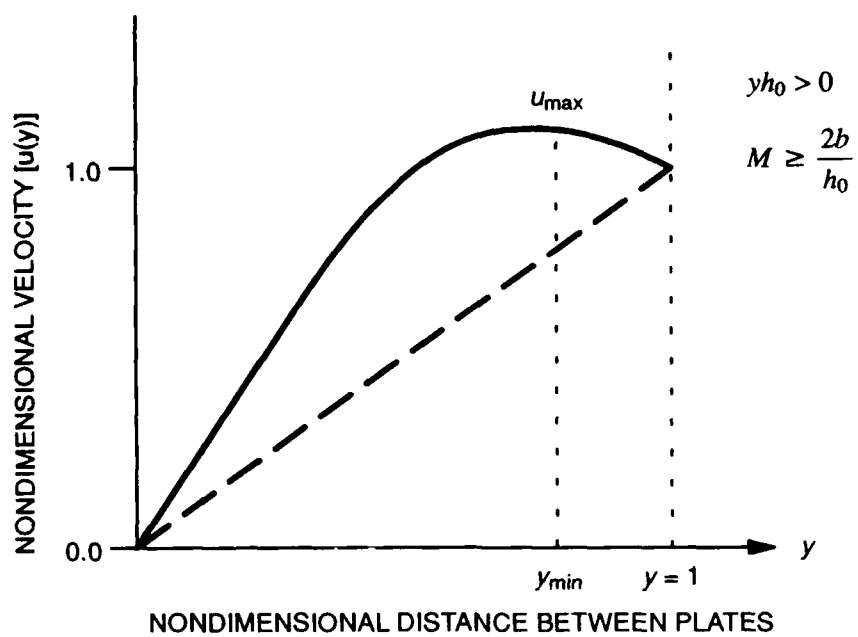
Fig. B-2. Typical nondimensional velocity profiles for $h_0 > 0$ and $h_0 < 0$.

Table B-1. One–dimensional Couette flow velocity for $b = 10$

M	$h_0 = +10$		$h_0 = -10$	
	y_{max}	u_{max}	y_{min}	u_{min}
10	0.600	1.800	0.400	-0.800
20	0.550	3.025	0.450	-2.025
30	0.533	4.267	0.467	-3.267
40	0.525	5.513	0.475	-4.513
50	0.520	6.760	0.480	-5.760

Table B–2. One–dimensional Couette flow electric potential for $b = 10$.

M	ϕ_0 for $h_0 = 0$	ϕ_0 for $h_0 = +10$	ϕ_0 for $h_0 = -10$
01	-0.5	-1.5833	0.583
10	-0.5	-1.4333	0.4333
20	-0.5	-2.2167	1.2167
30	-0.5	-3.0333	2.0333
40	-0.5	-3.8583	2.8583
50	-0.5	-4.6867	3.6867
3.464	-0.5	-1.077	0.077
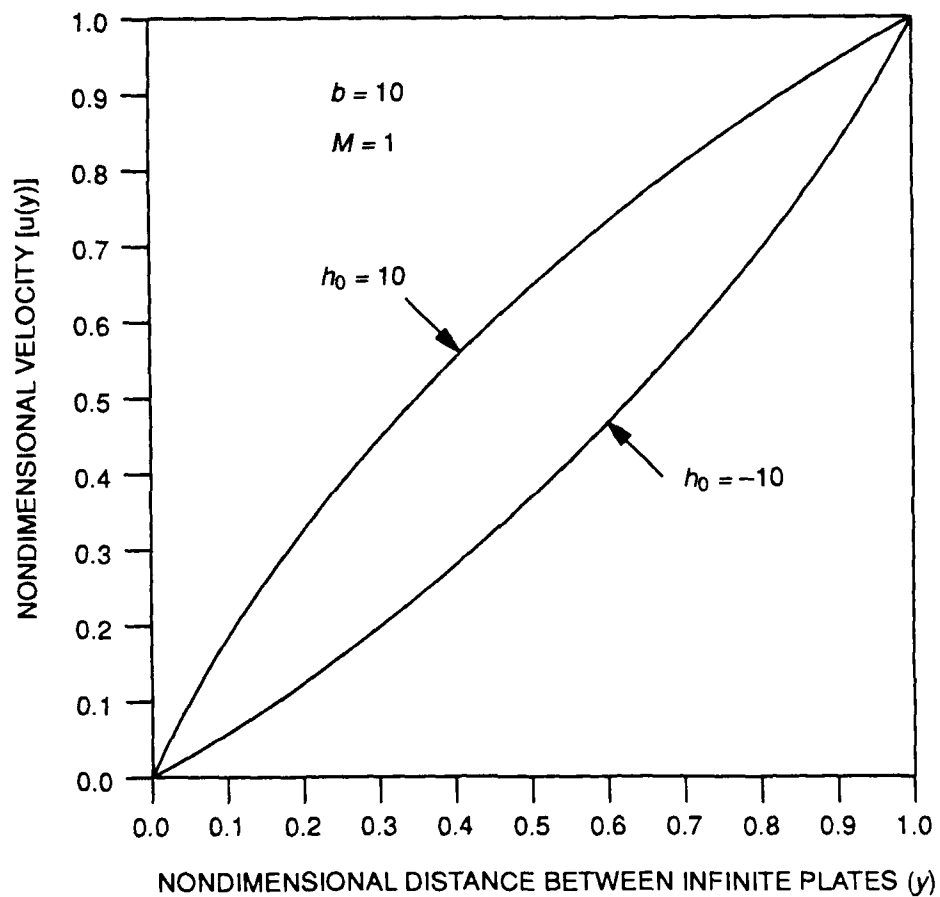
Fig. B-3. Nondimensional velocity $u(y)$ from one-dimensional theory
for $h_o = \pm 10$ and Hartmann number $M = 1$

APPENDIX C
COMPLEX CONTOUR PLOTS

This Appendix presents the complex contour plot of the nondimensional velocity profile for a specific M and h_o at the top of each page. At the bottom of the page is the corresponding contour plot of the current density stream function. The plots are sorted according to the following 5 groups:

➤ Figures C-1A – C-2b $\qquad$ $M = 2$, $\qquad$ $h_o = 0$
$\qquad\qquad\qquad\qquad\qquad\qquad\qquad$ $M = 10$, $\qquad$ $h_o = 0$

➤ Figures C-3a – C-7b $\qquad$ $M = 2$, $\qquad$ $h_c = \quad 20$
$\qquad\qquad\qquad\qquad\qquad\qquad\qquad$ $M = 2$, $\qquad$ $h_o = \quad 40$
$\qquad\qquad\qquad\qquad\qquad\qquad\qquad$ $M = 2$, $\qquad$ $h_o = \quad 60$
$\qquad\qquad\qquad\qquad\qquad\qquad\qquad$ $M = 2$, $\qquad$ $h_o = \quad 80$
$\qquad\qquad\qquad\qquad\qquad\qquad\qquad$ $M = 2$, $\qquad$ $h_o = \quad 100$

➤ Figures C-8a – C-12b $\qquad$ $M = 10$, $\qquad$ $h_o = \quad 20$
$\qquad\qquad\qquad\qquad\qquad\qquad\qquad$ $M = 10$, $\qquad$ $h_o = \quad 40$
$\qquad\qquad\qquad\qquad\qquad\qquad\qquad$ $M = 10$, $\qquad$ $h_o = \quad 60$
$\qquad\qquad\qquad\qquad\qquad\qquad\qquad$ $M = 10$, $\qquad$ $h_o = \quad 80$
$\qquad\qquad\qquad\qquad\qquad\qquad\qquad$ $M = 10$, $\qquad$ $h_o = \quad 100$

➤ Figures C-13a – C-17b $\qquad$ $M = 2$, $\qquad$ $h_o = \quad -20$
$\qquad\qquad\qquad\qquad\qquad\qquad\qquad$ $M = 2$, $\qquad$ $h_o = \quad -40$
$\qquad\qquad\qquad\qquad\qquad\qquad\qquad$ $M = 2$, $\qquad$ $h_o = \quad -60$
$\qquad\qquad\qquad\qquad\qquad\qquad\qquad$ $M = 2$, $\qquad$ $h_o = \quad -80$
$\qquad\qquad\qquad\qquad\qquad\qquad\qquad$ $M = 2$, $\qquad$ $h_o = \quad -100$

➤ Figures C-18a – C-22b $\qquad$ $M = 10$, $\qquad$ $h_o = \quad -20$
$\qquad\qquad\qquad\qquad\qquad\qquad\qquad$ $M = 10$, $\qquad$ $h_o = \quad -40$
$\qquad\qquad\qquad\qquad\qquad\qquad\qquad$ $M = 10$, $\qquad$ $h_o = \quad -60$
$\qquad\qquad\qquad\qquad\qquad\qquad\qquad$ $M = 10$, $\qquad$ $h_o = \quad -80$
$\qquad\qquad\qquad\qquad\qquad\qquad\qquad$ $M = 10$, $\qquad$ $h_o = \quad -100.$

The symbol M represents the Hartmann number, and h_o is a measure of the load current across the rectangular channel.
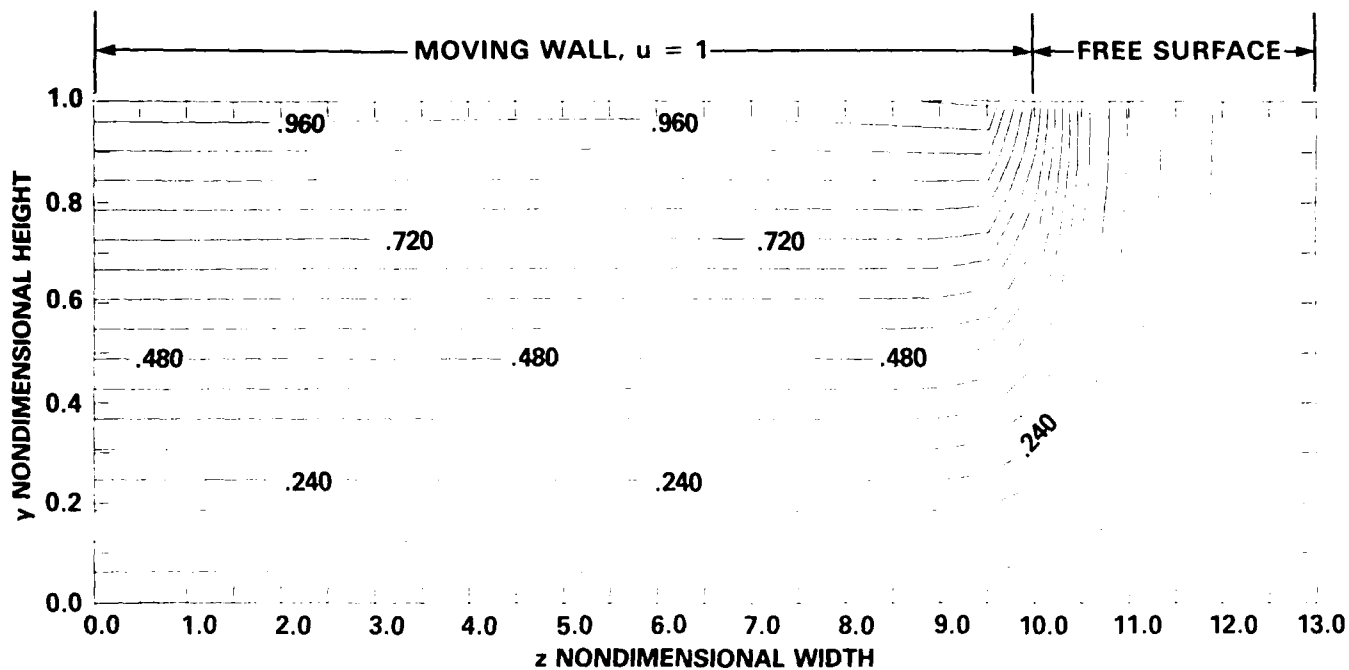
Fig. C-1a. Nondimensional velocity contours $u(y,z)$ for Hartmann number $M = 2$ and $h_0 = 0$.
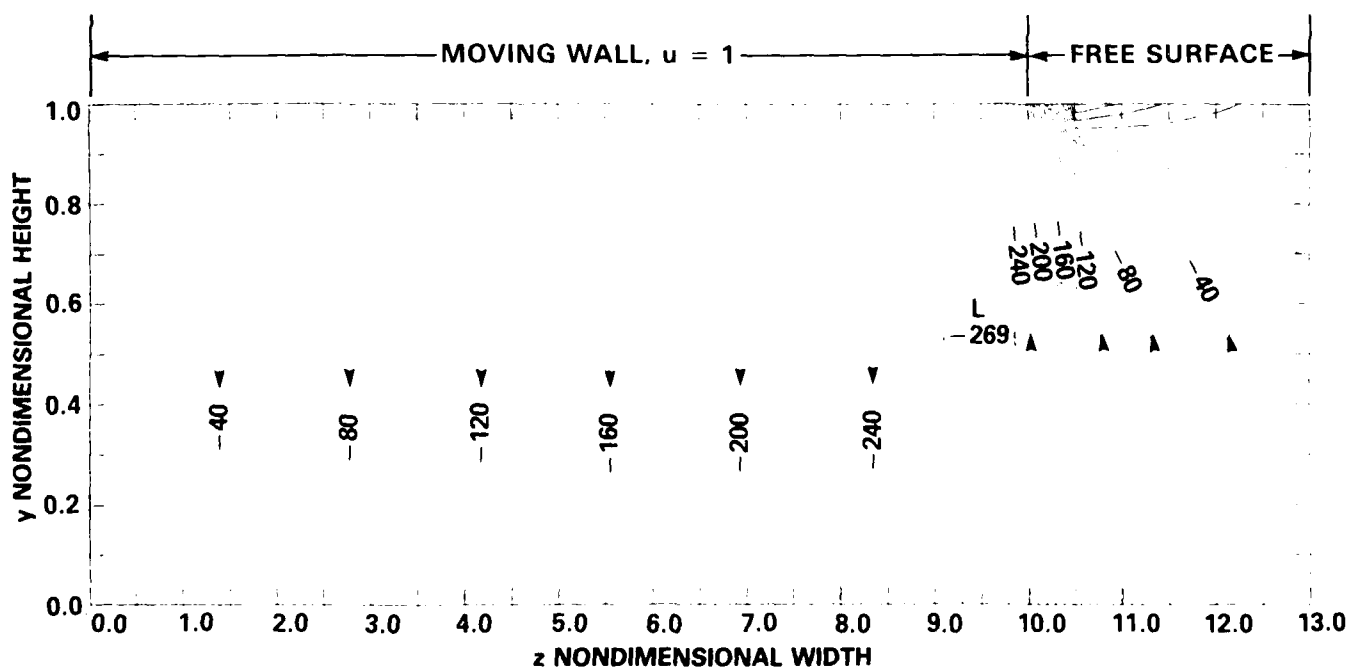
Fig. C-1b. Nondimensional current density stream function contours $h(y,z) \times 10^3$ for Hartmann number $M = 2$ and $h_0 = 0$.

48
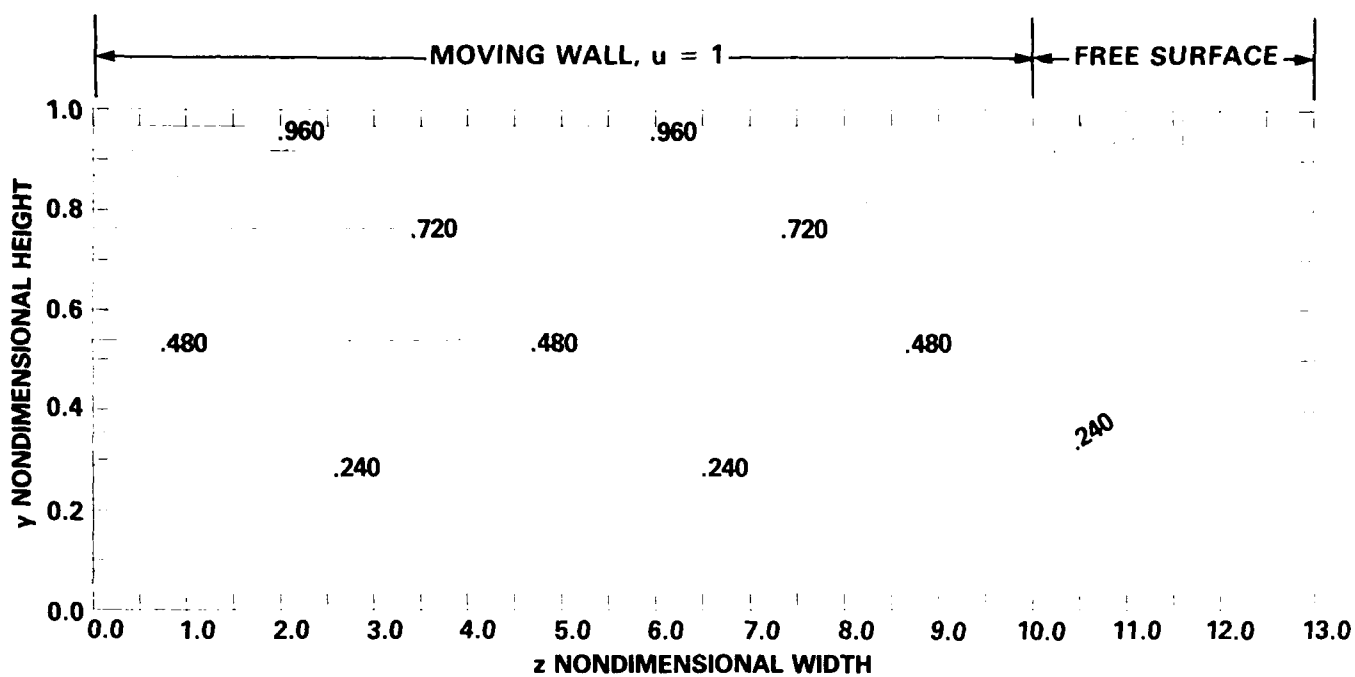
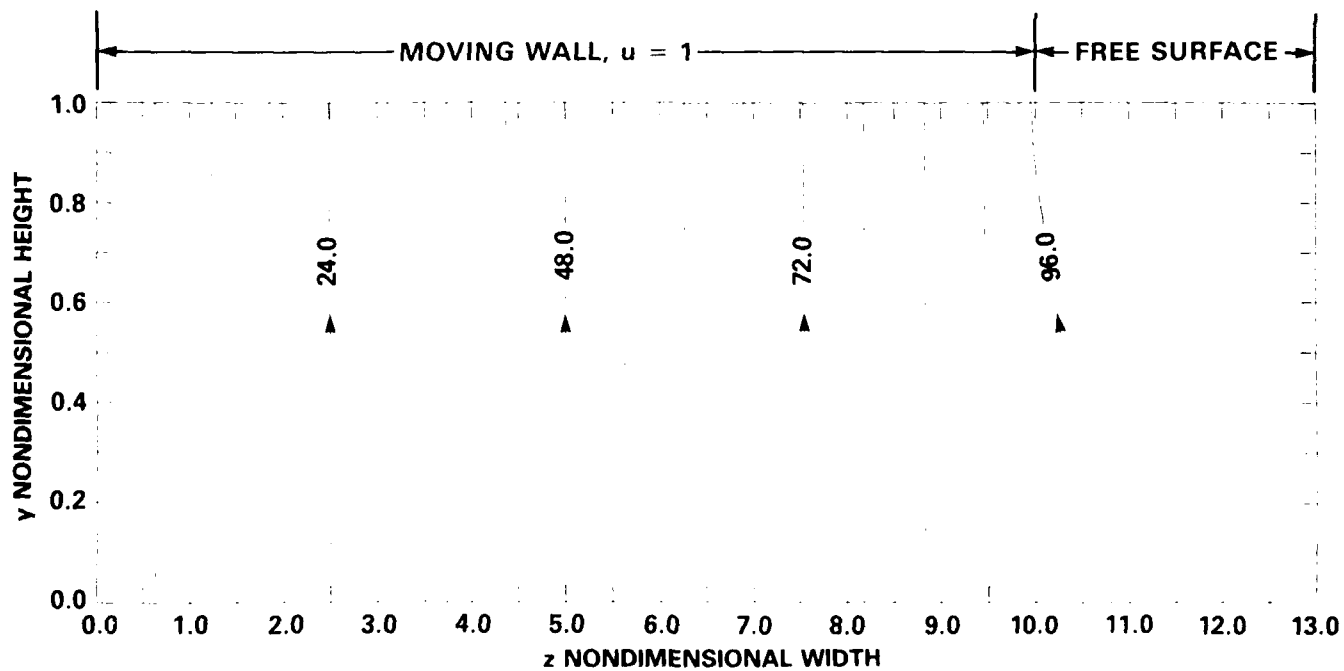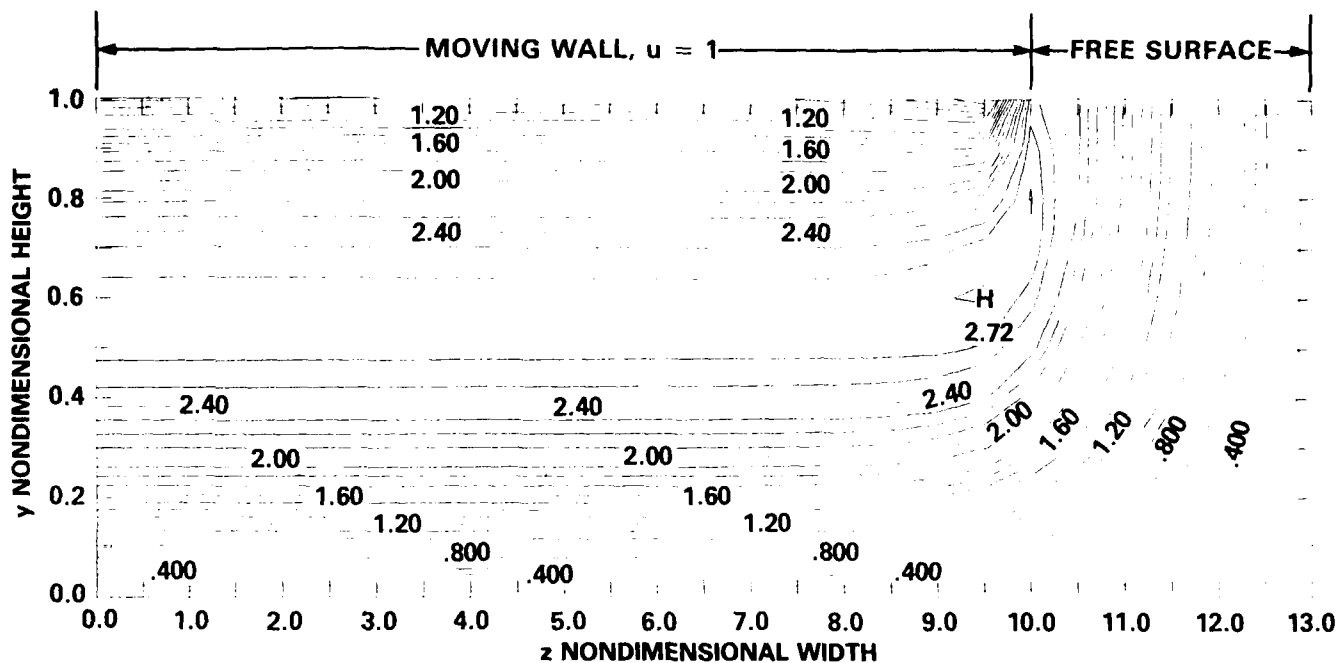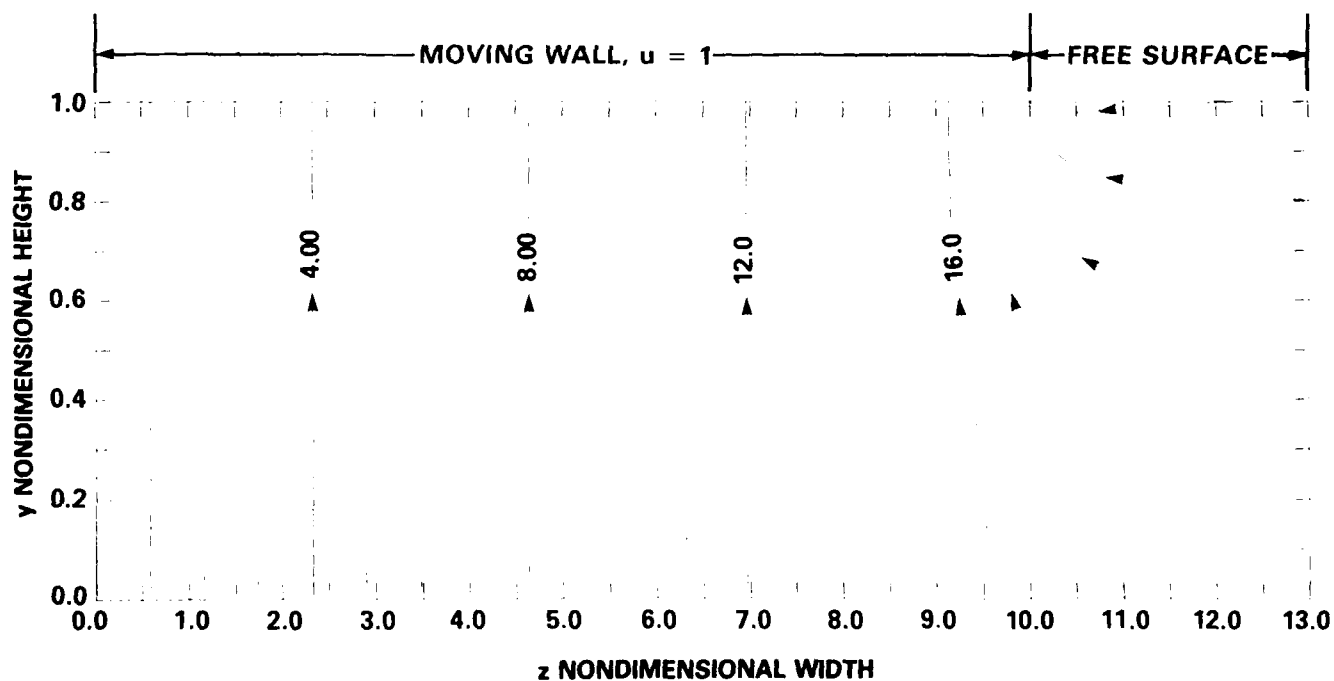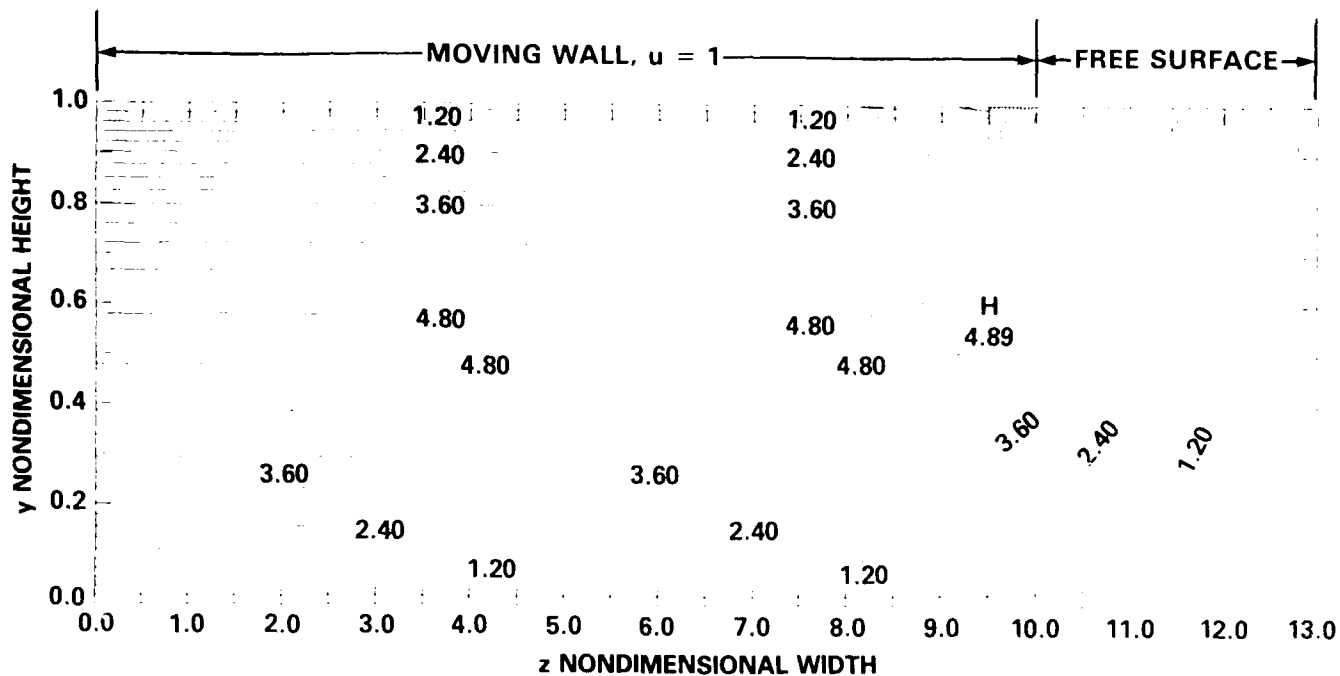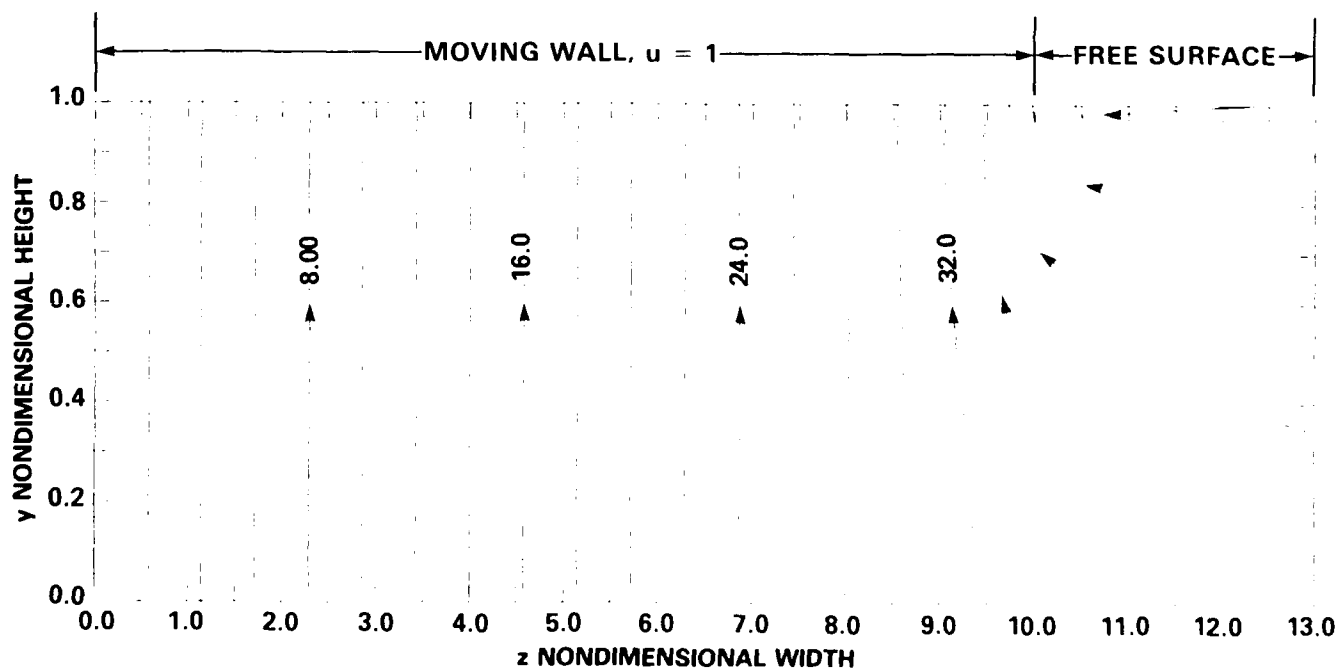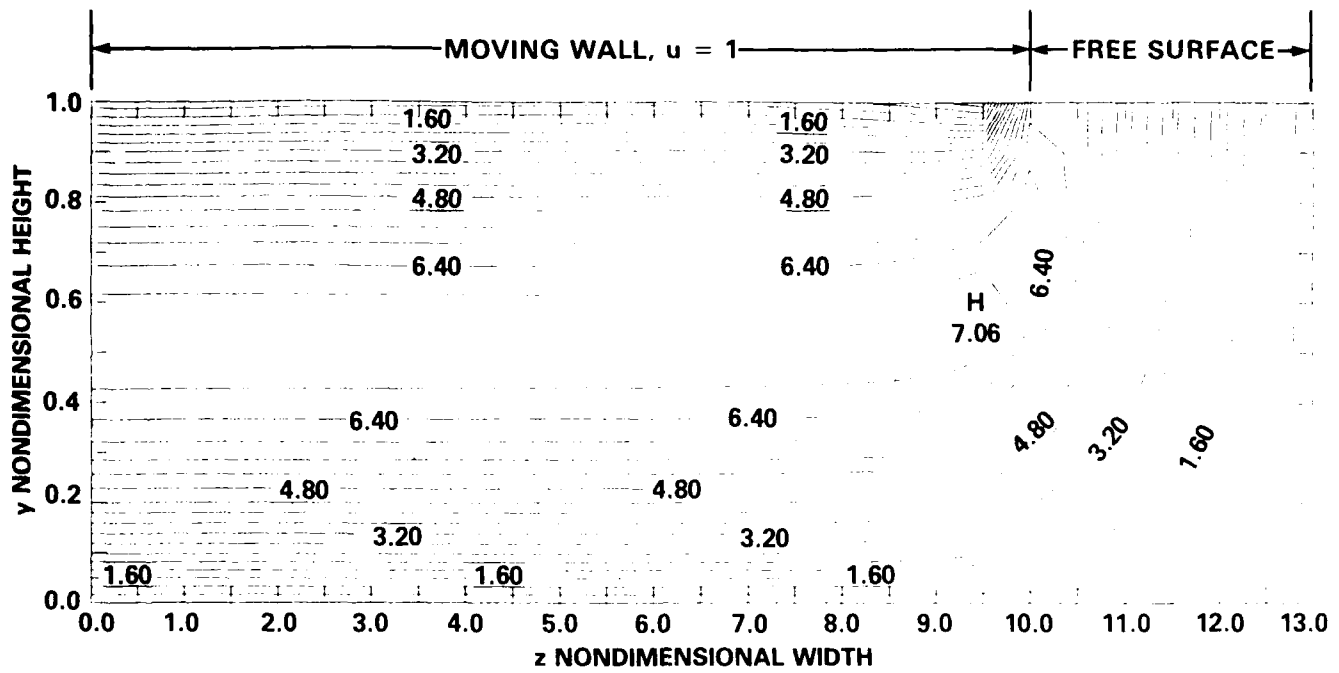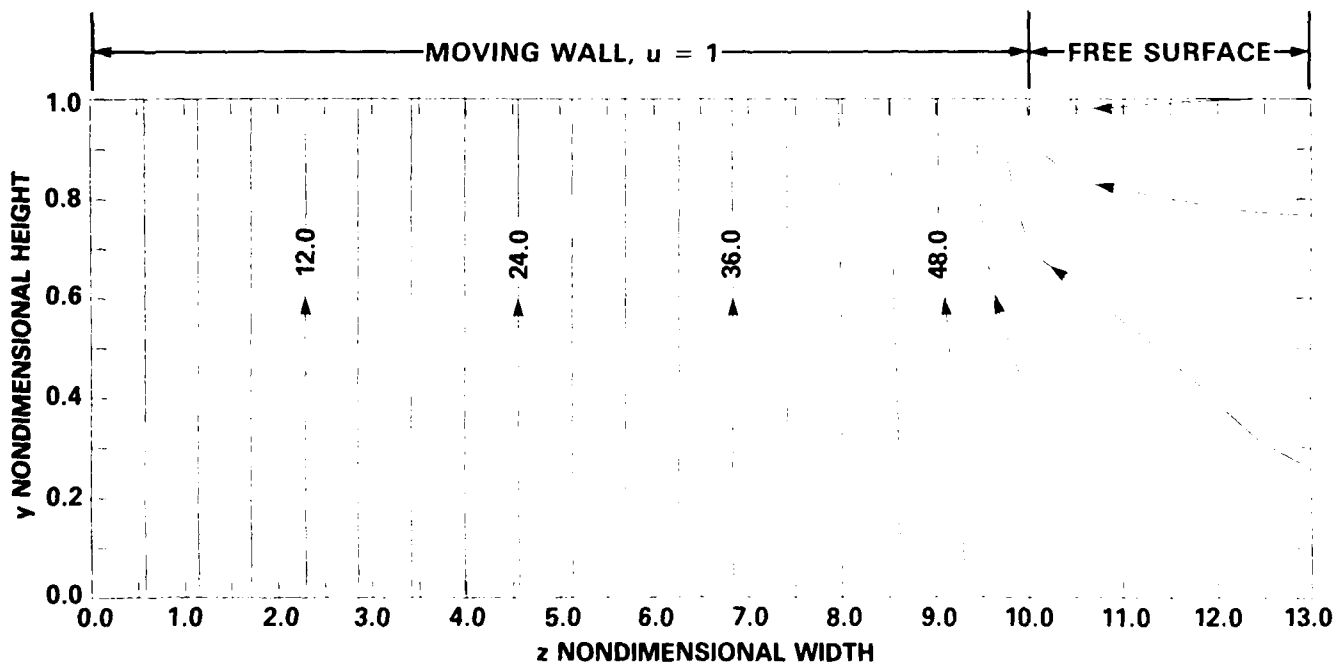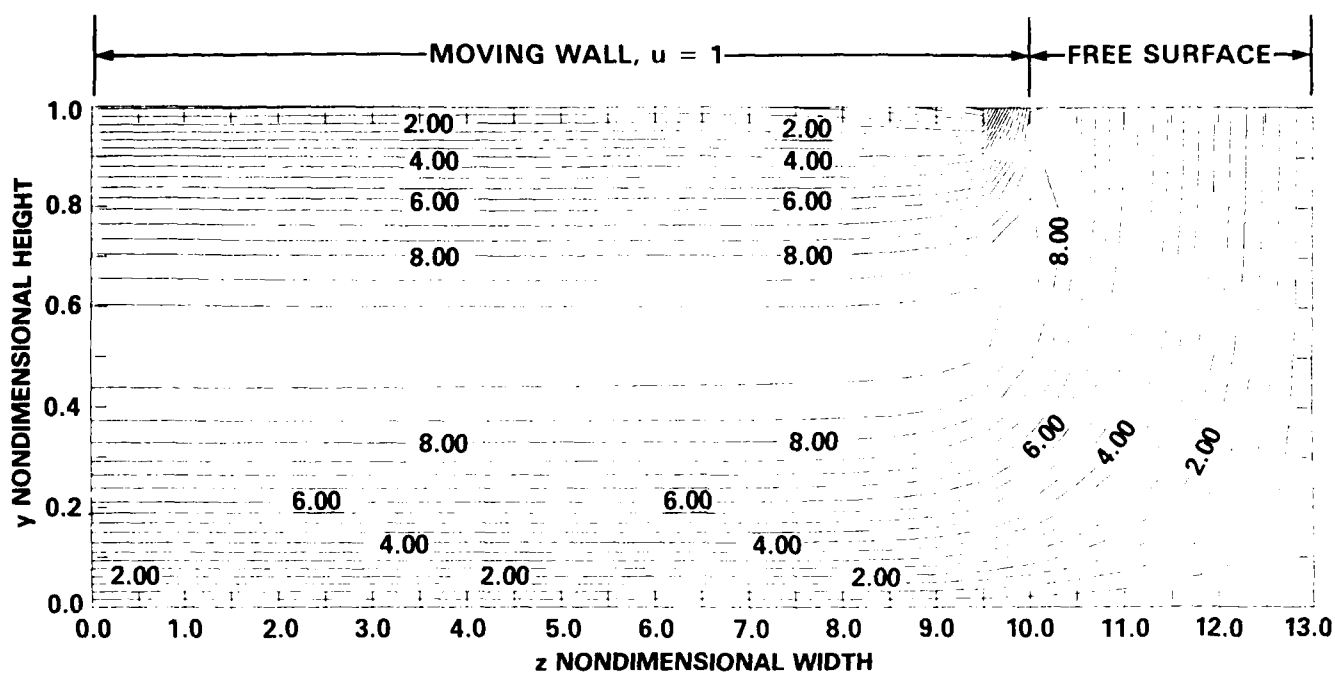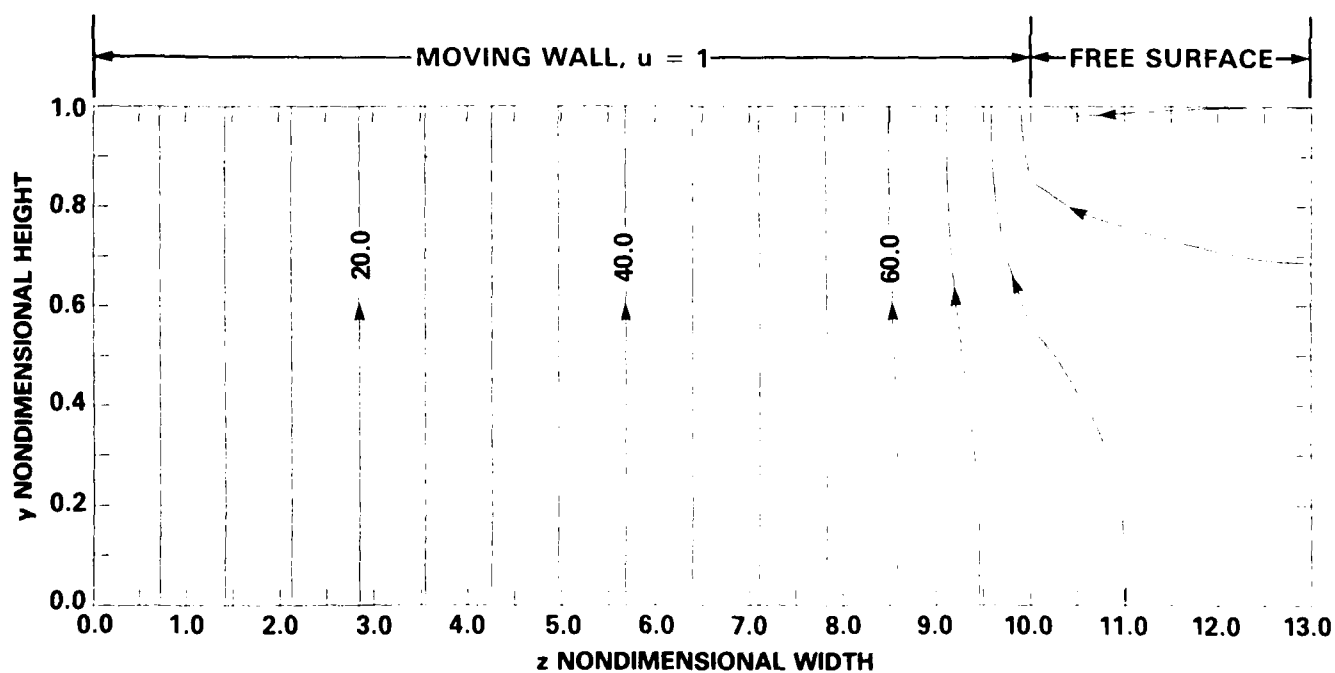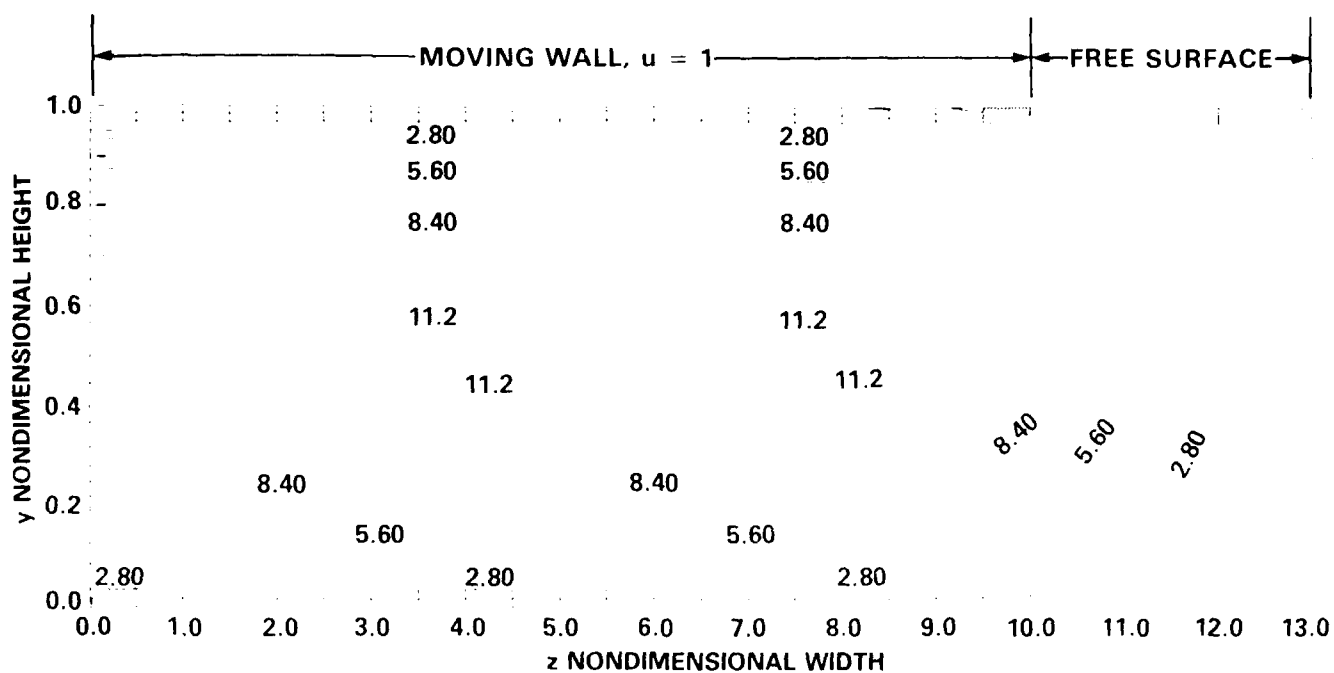Fig. C-2a. Nondimensional velocity contours $u(y,z)$ for Hartmann number $M = 10$ and $h_o = 0$.
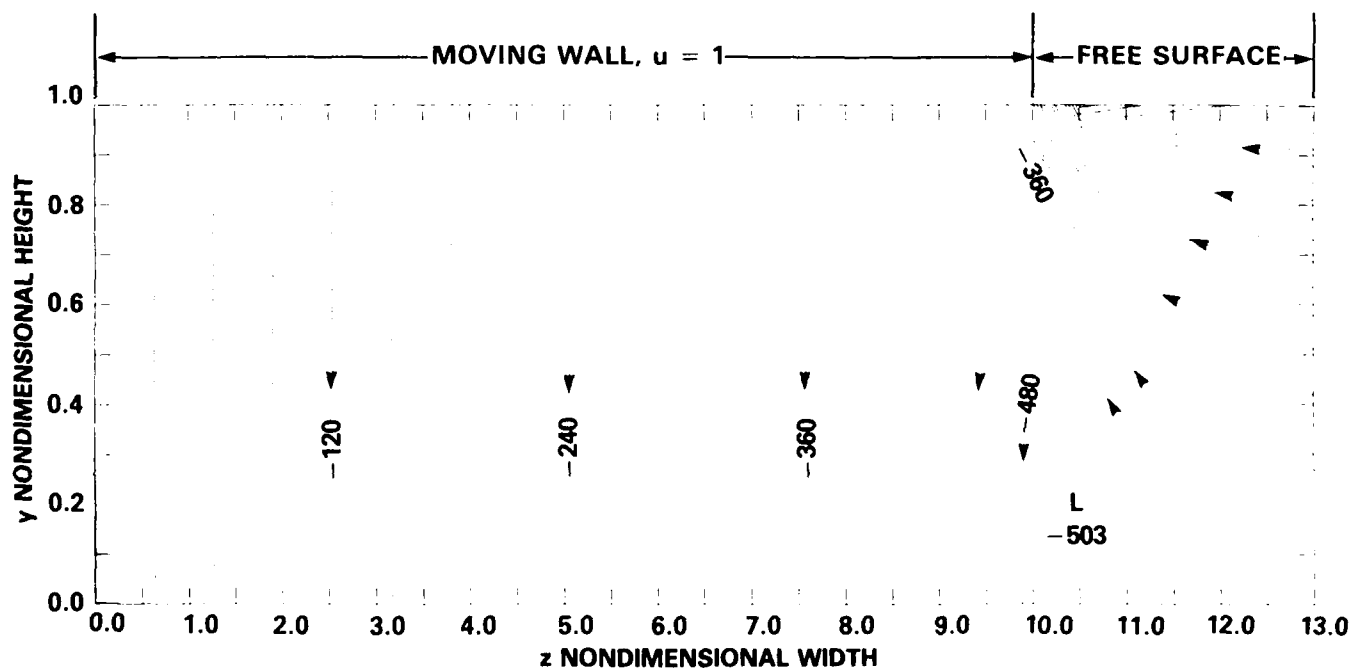
Fig. C-2b. Nondimensional current density stream function contours $h(y,z) \times 10^3$ for Hartmann number $M = 10$ and $h_o = 0$.
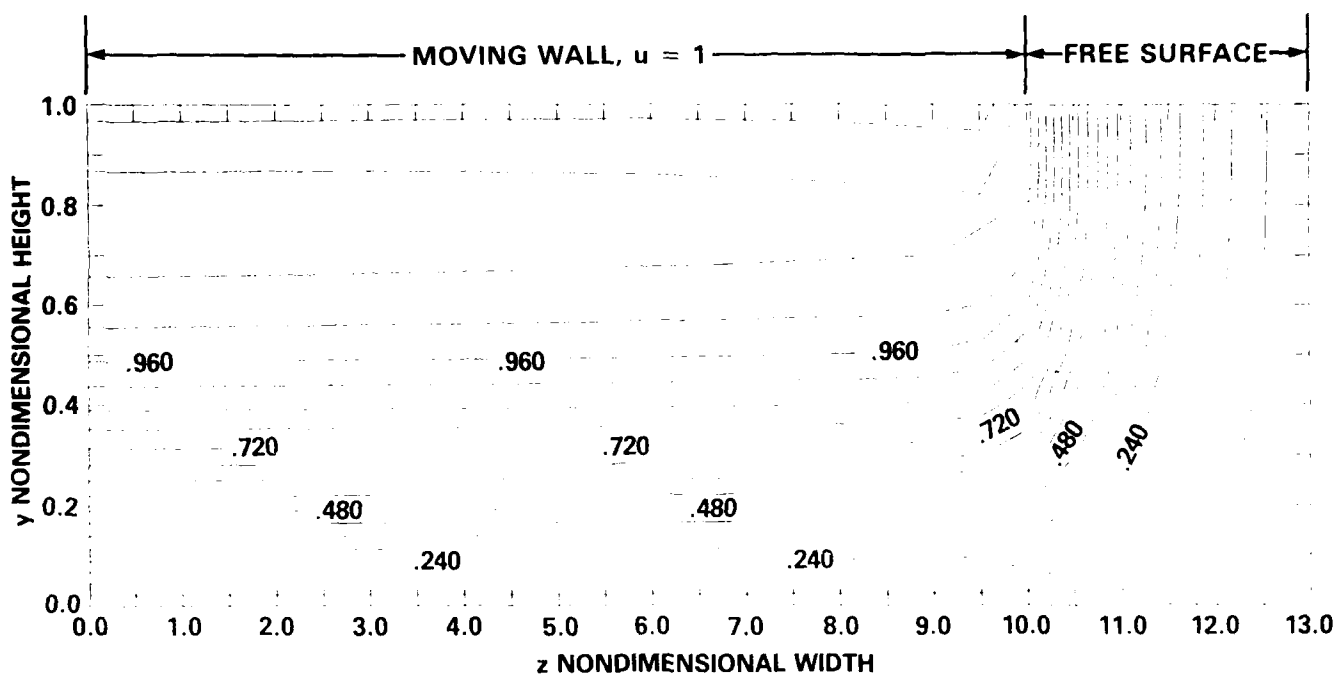
Fig. C-3a. Nondimensional velocity contours $u(y,z)$ for
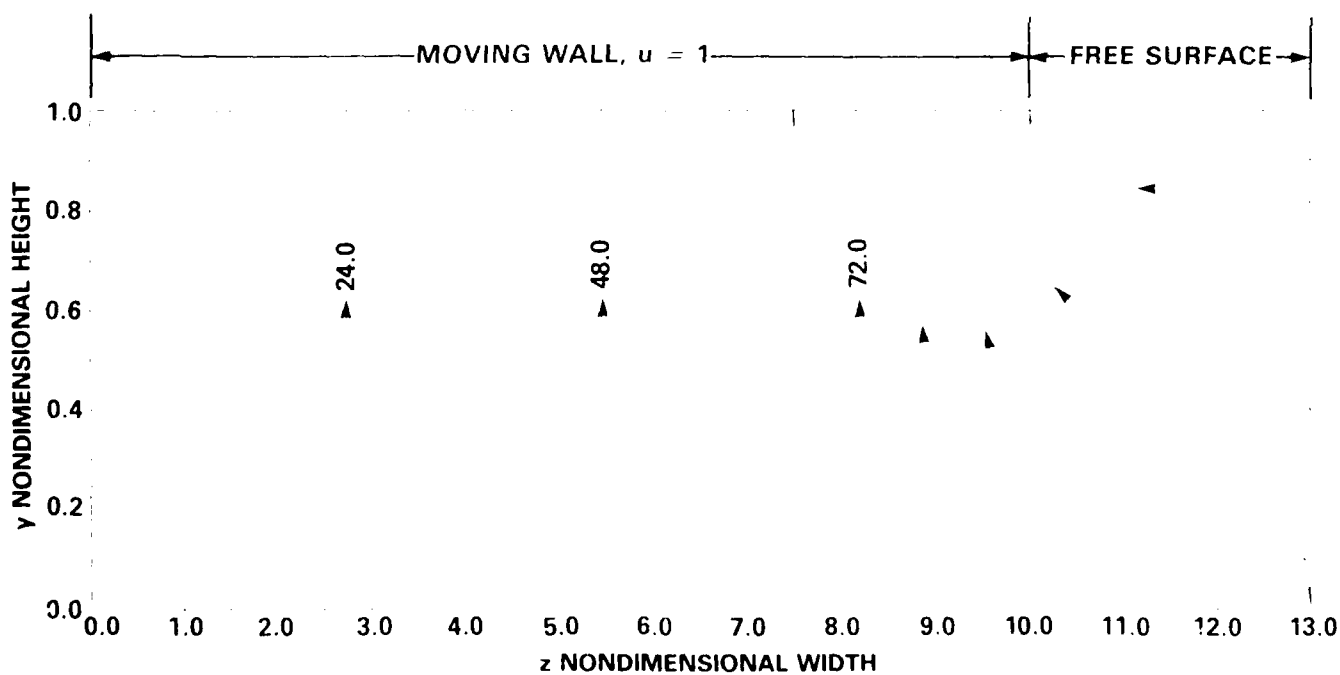Hartmann number $M = 2$ and $h_0 = 20$.
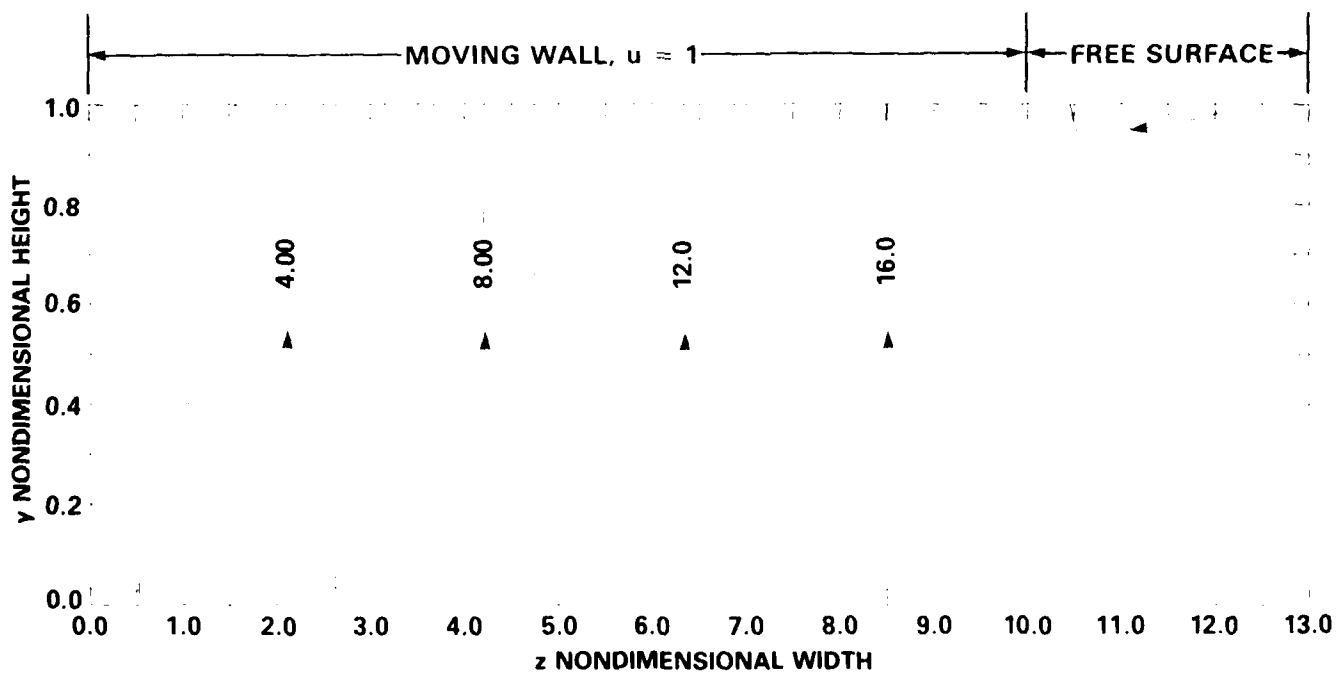
Fig. C-3b. Nondimensional current density stream function contours
$h(y,z)$ for Hartmann number $M = 2$ and $h_0 = 20$.
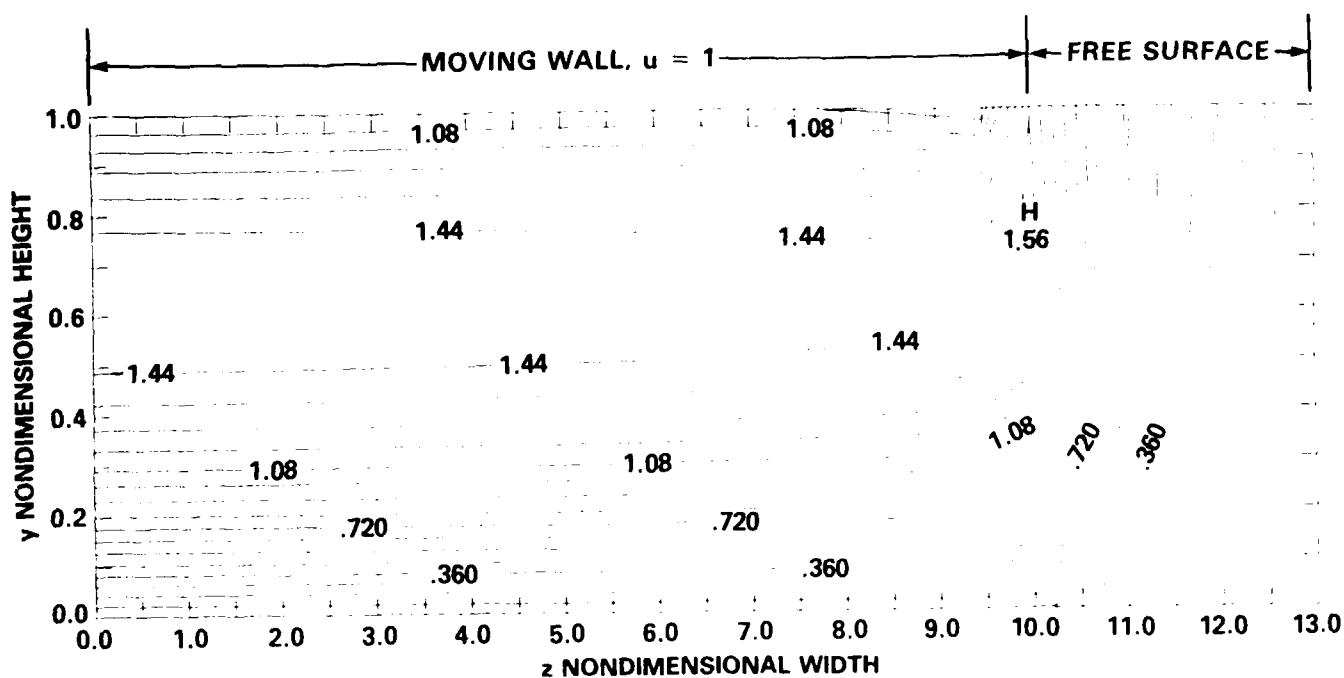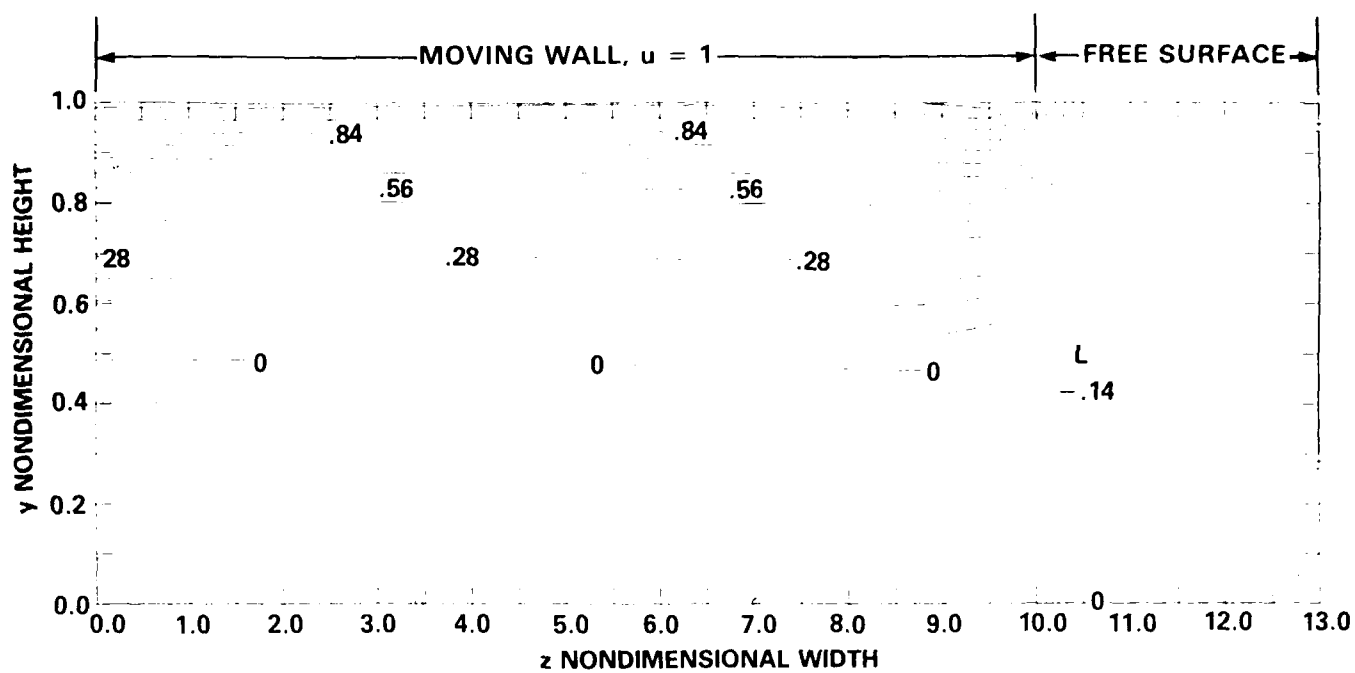
Fig. C-4a. Nondimensional velocity contours $u(y,z)$ for
Hartmann number $M = 2$ and $h_0 = 40$.
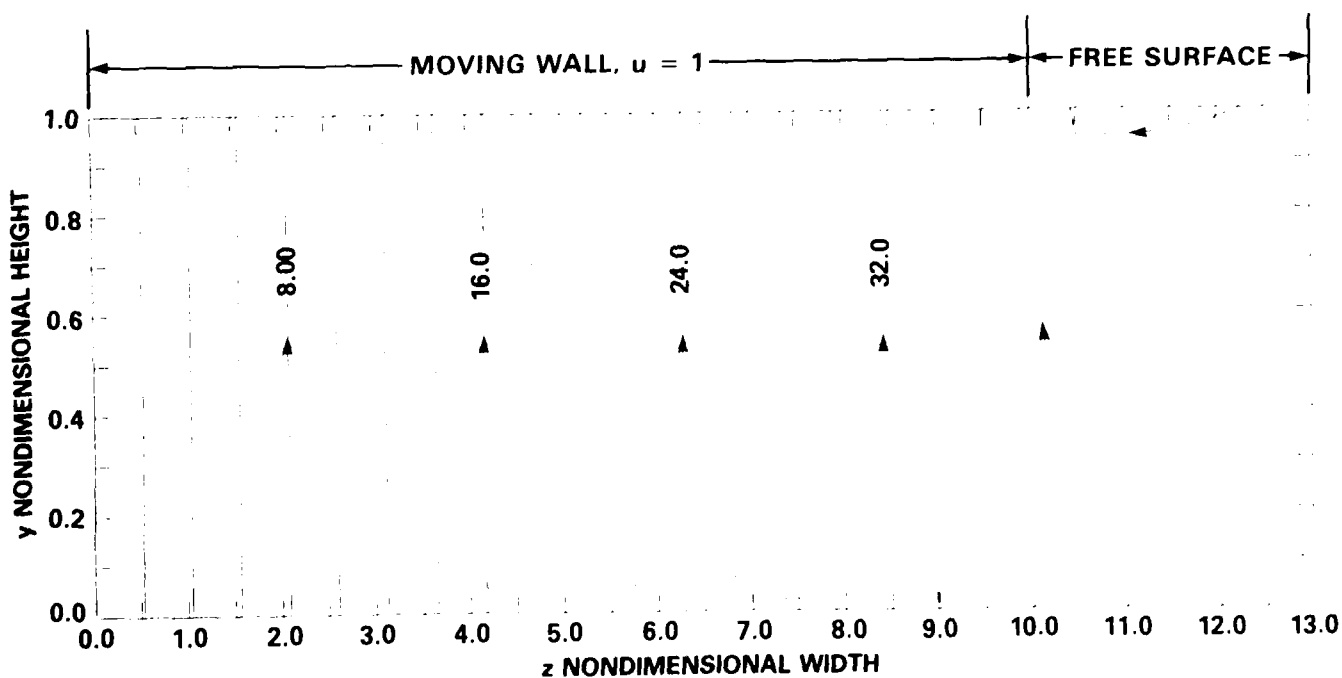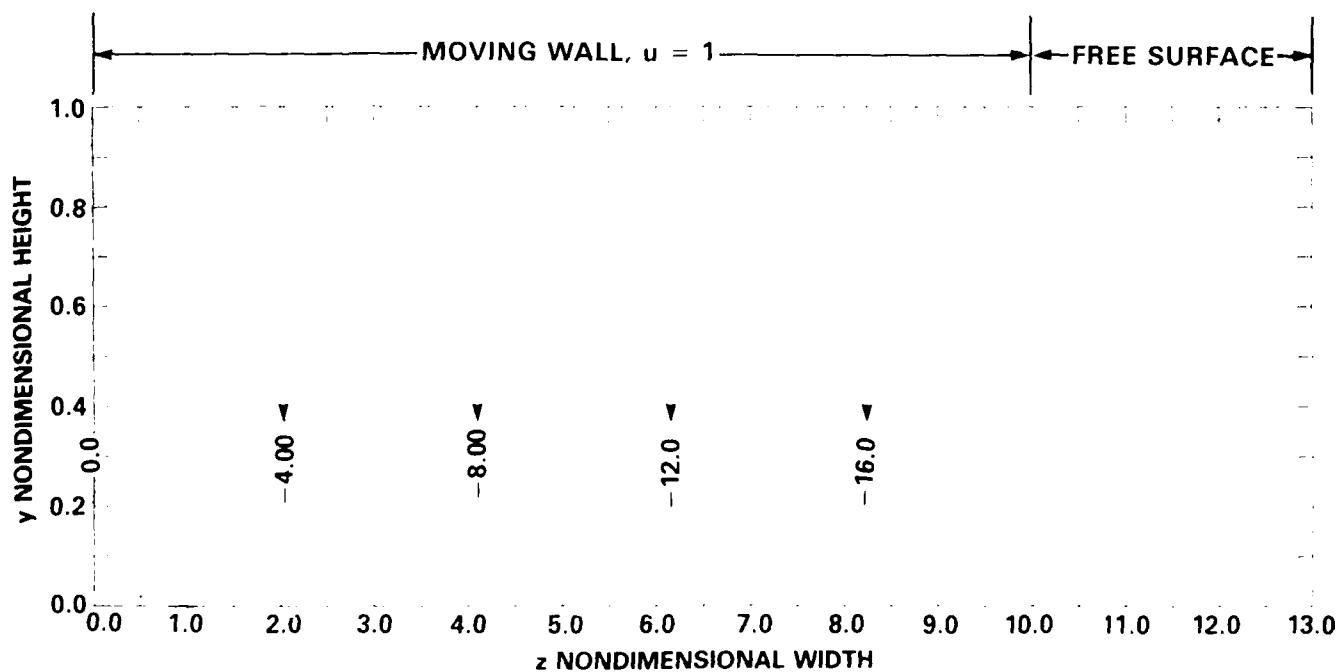

Fig. C-4b. Nondimensional current density stream function contours
$h(y,z)$ for Hartmann number $M = 2$ and $h_0 = 40$.
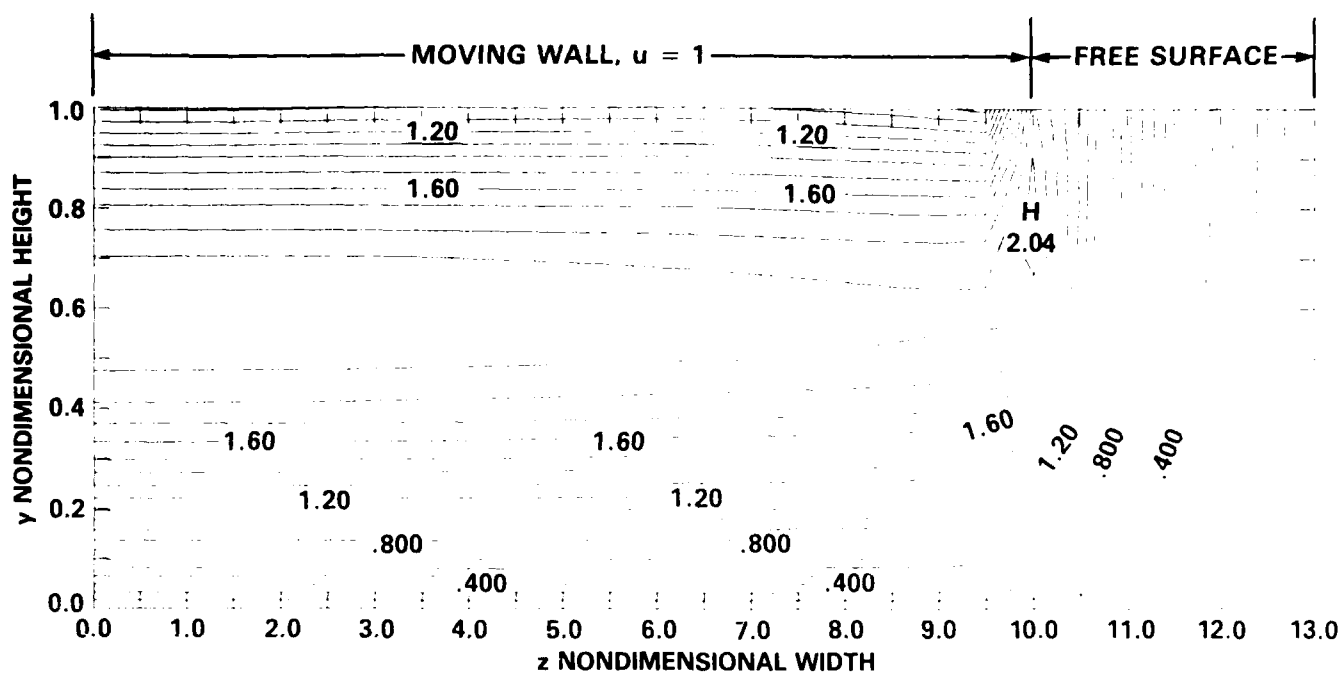
Fig. C-5a. Nondimensional velocity contours $u(y,z)$ for
Hartmann number $M = 2$ and $h_0 = 60$.
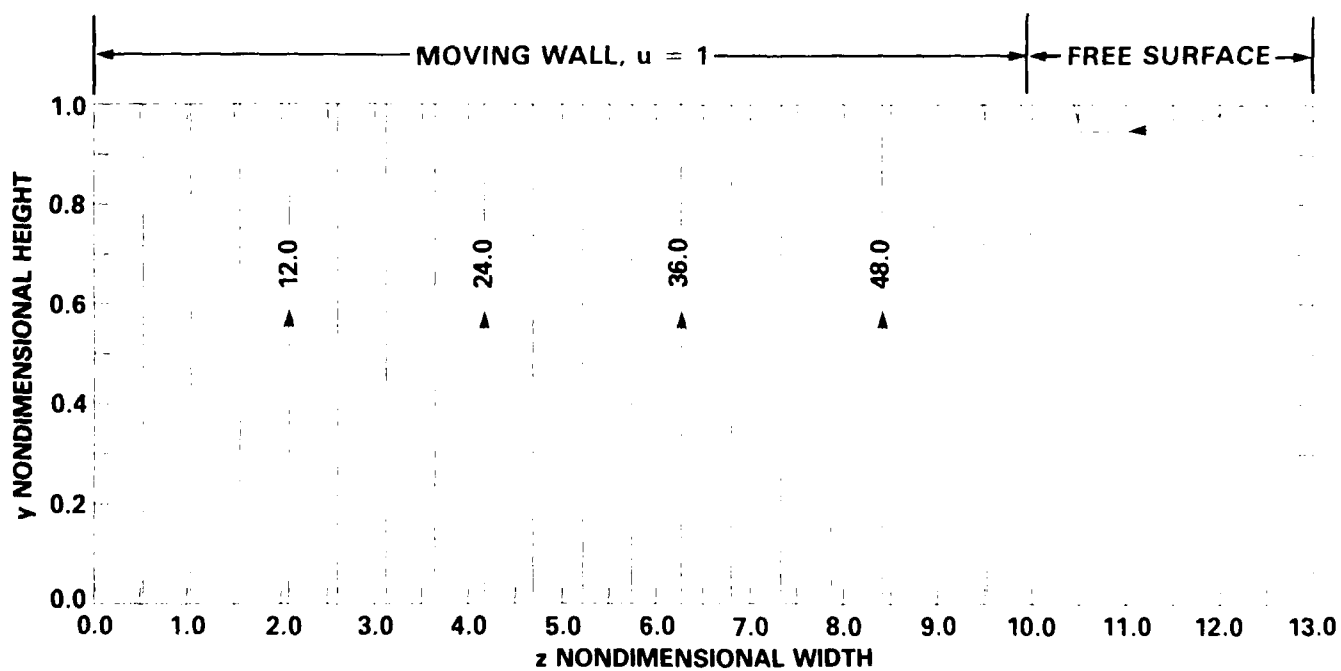
Fig. C-5b. Nondimensional current density stream function contours
$h(y,z)$ for Hartmann number $M = 2$ and $h_0 = 60$.
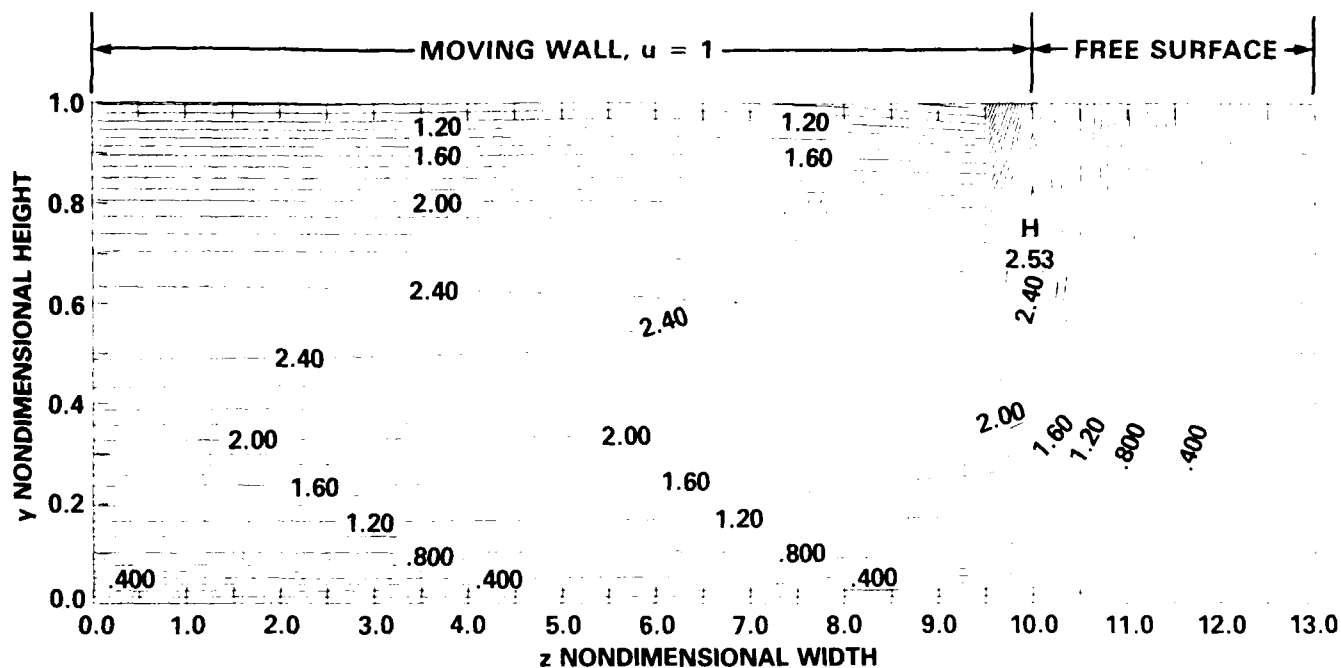
Fig. C-6a. Nondimensional velocity contours $u(y,z)$ for
Hartmann number $M = 2$ and $h_0 = 80$.
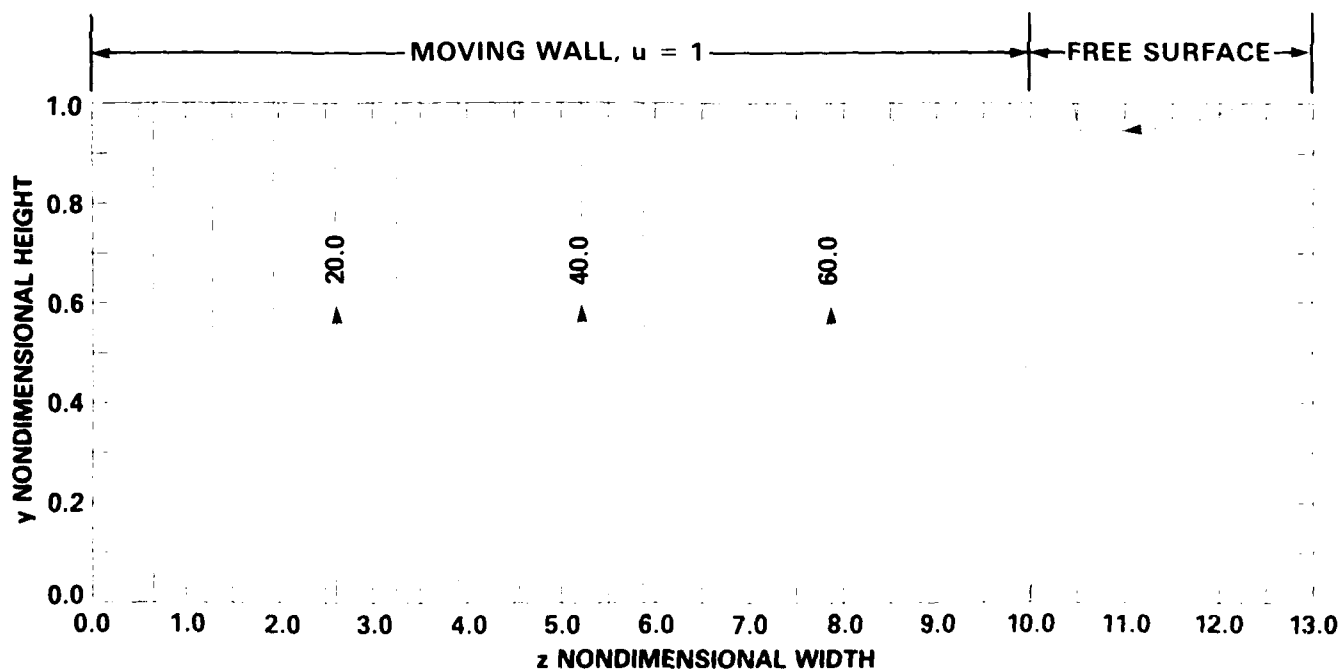
Fig. C-6b. Nondimensional current density stream function contours
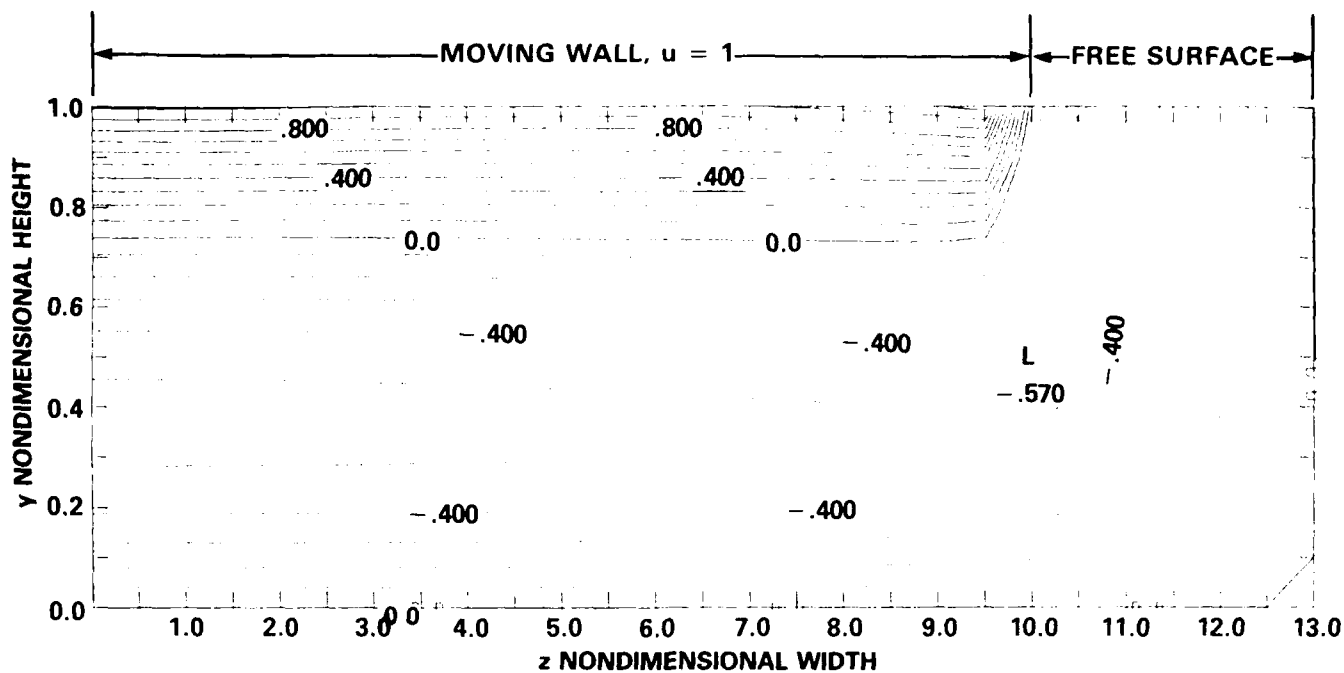$h(y,z)$ for Hartmann number $M = 2$ and $h_0 = 80$.
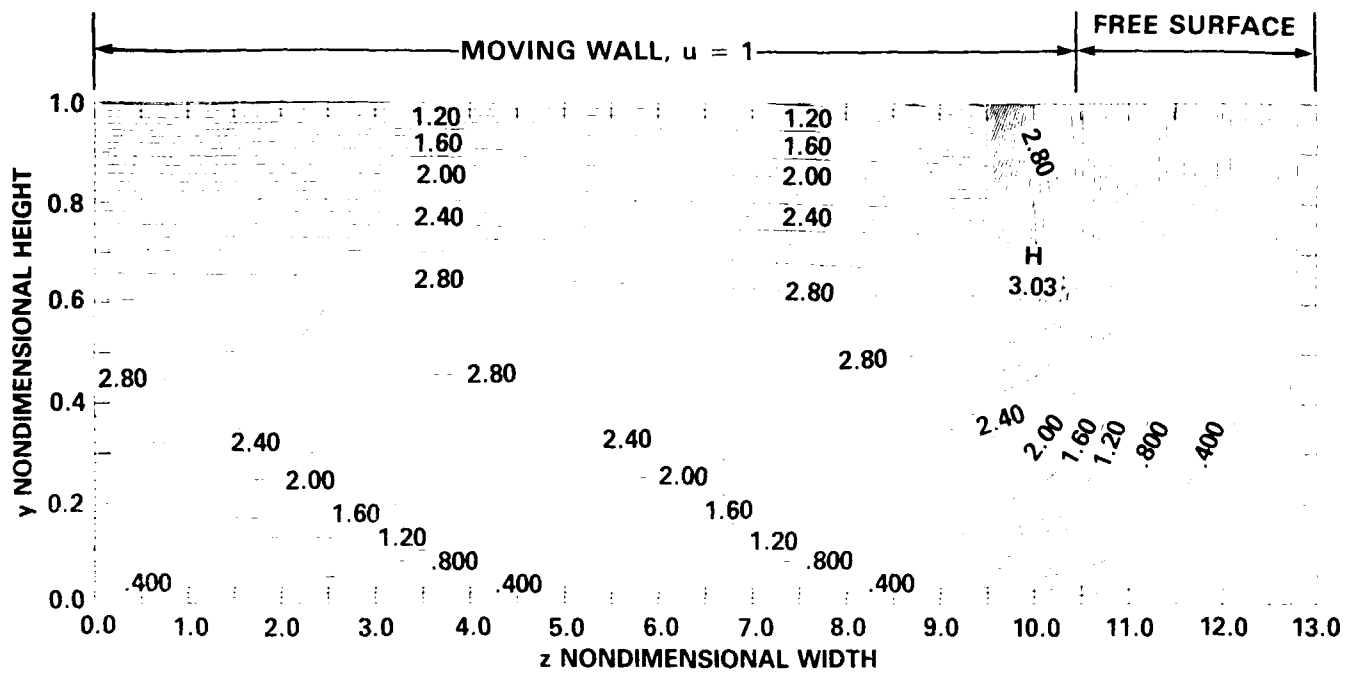
Fig. C-7a. Nondimensional velocity contours $u(y,z)$ for
Hartmann number $M = 2$ and $h_0 = 100$.
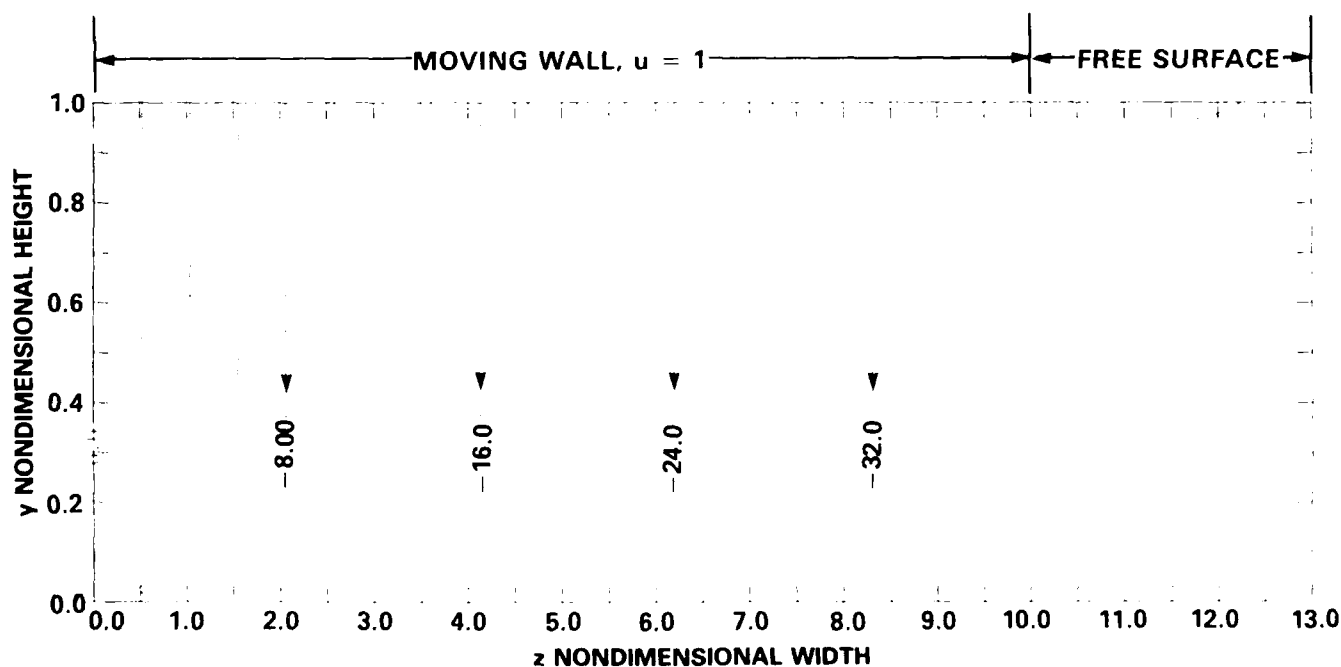

Fig. C-7b. Nondimensional current density stream function contours
$h(y,z)$ for Hartmann number $M = 2$ and $h_0 = 100$.

Fig. C-8a. Nondimensional velocity contours $u(y,z)$ for
Hartmann number $M = 10$ and $h_0 = 20$.

Fig. C-8b. Nondimensional current density stream function contours
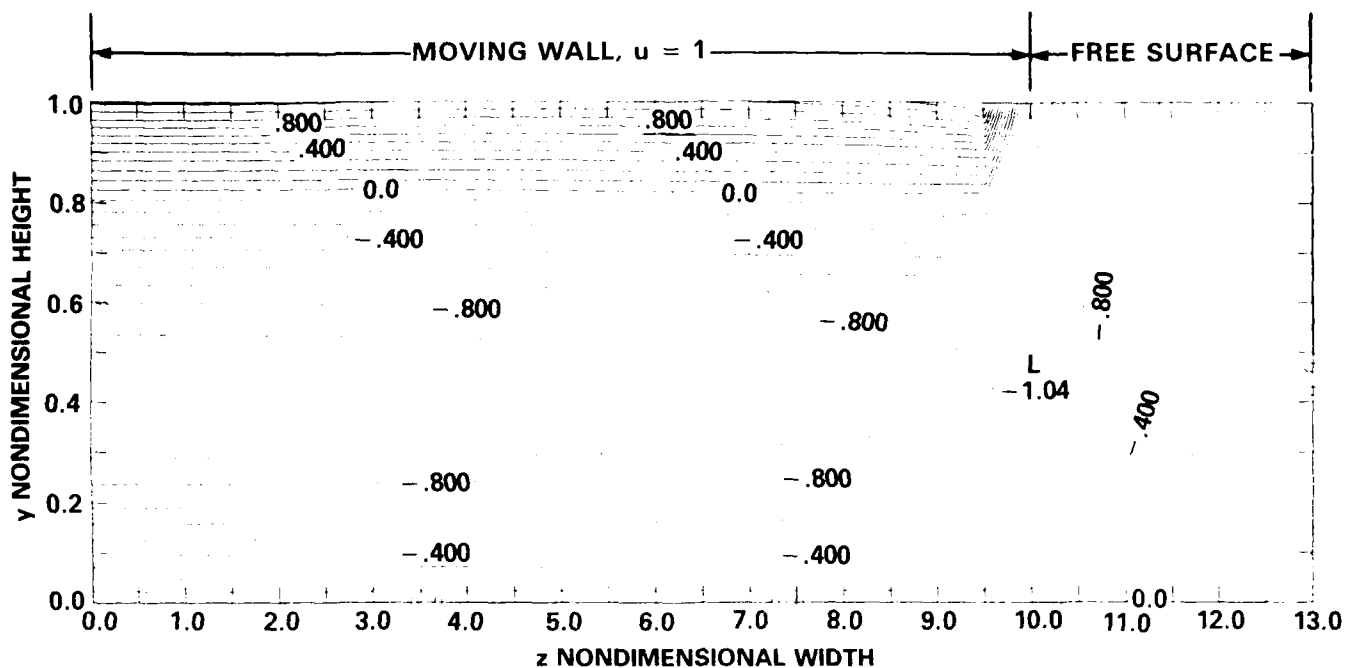$h(y,z)$ for Hartmann number $M = 10$ and $h_0 = 20$.

Fig. C-9a. Nondimensional velocity contours $u(y,z)$ for
Hartmann number $M = 10$ and $h_0 = 40$.

Fig. C-9b. Nondimensional current density stream function contours
$h(y,z)$ for Hartmann number $M = 10$ and $h_0 = 40$.

Fig. C-10a. Nondimensional velocity contours $u(y,z)$
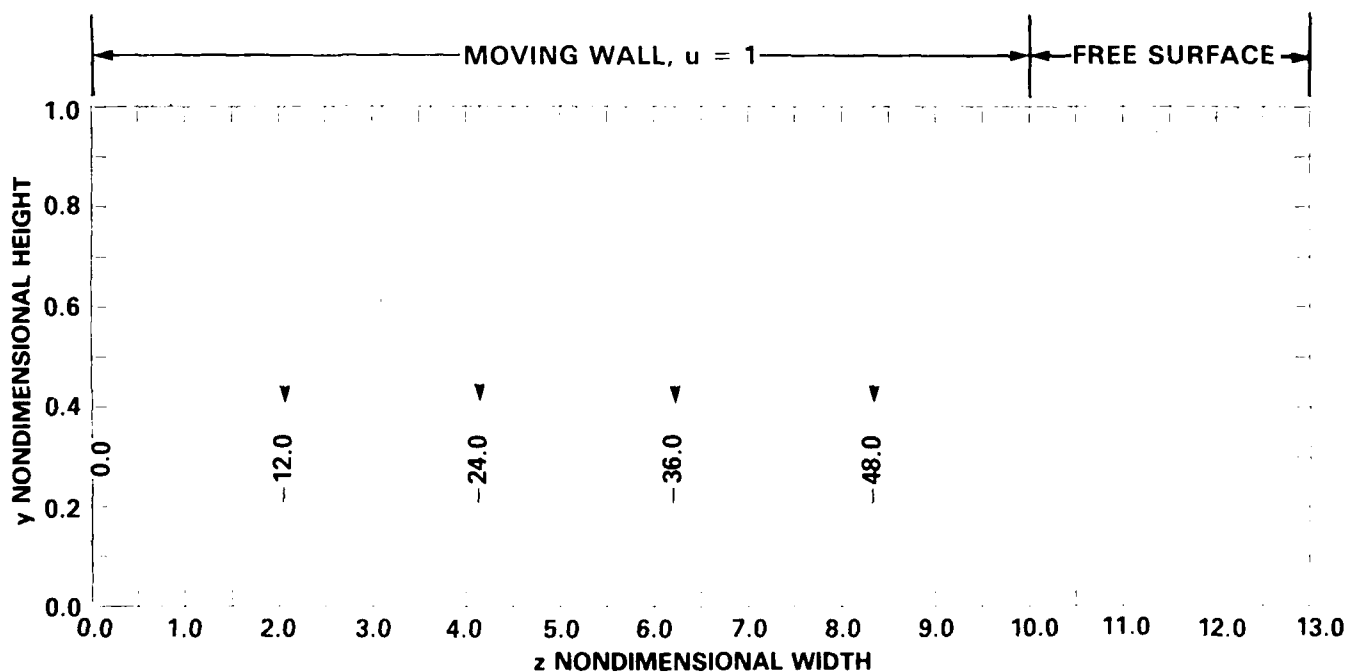for Hartmann number $M = 10$ and $h_0 = 60$.

Fig. C-10b. Nondimensional current density stream function contours
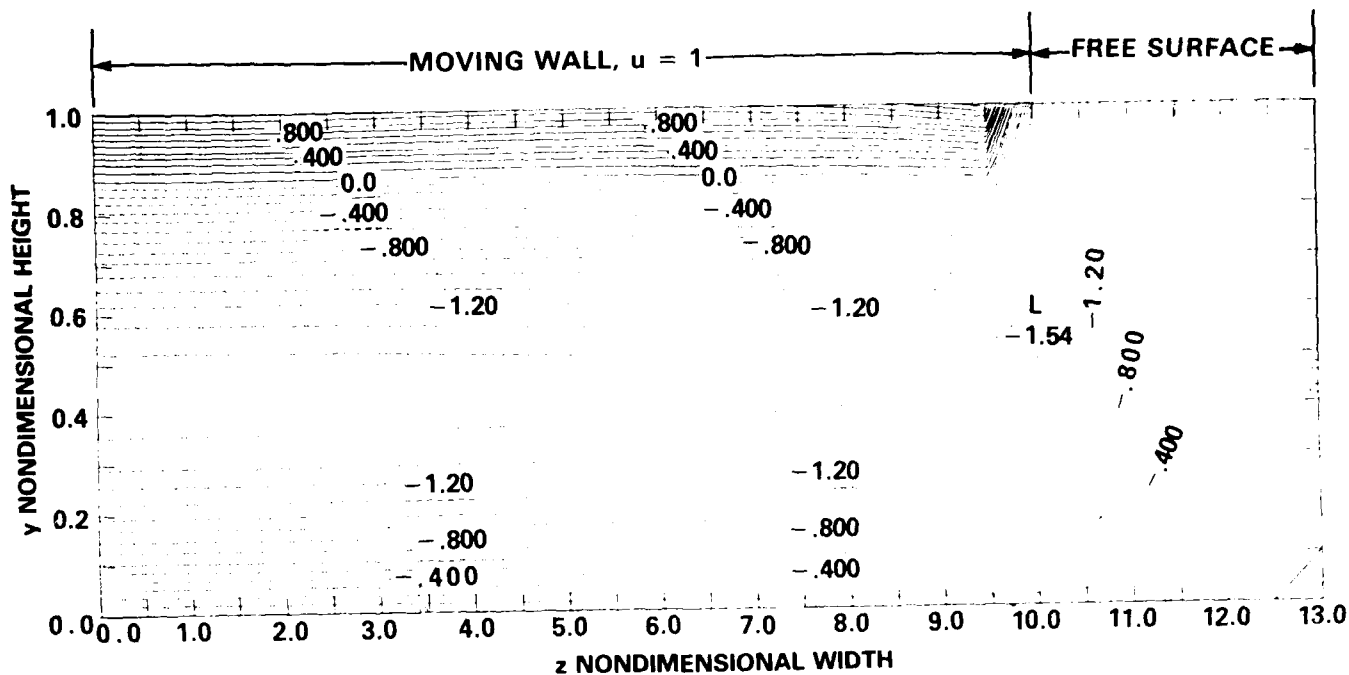$h(y,z)$ for Hartmann number $M = 10$ and $h_0 = 60$.

Fig. C-11a. Nondimensional velocity contours $u(y,z)$ for
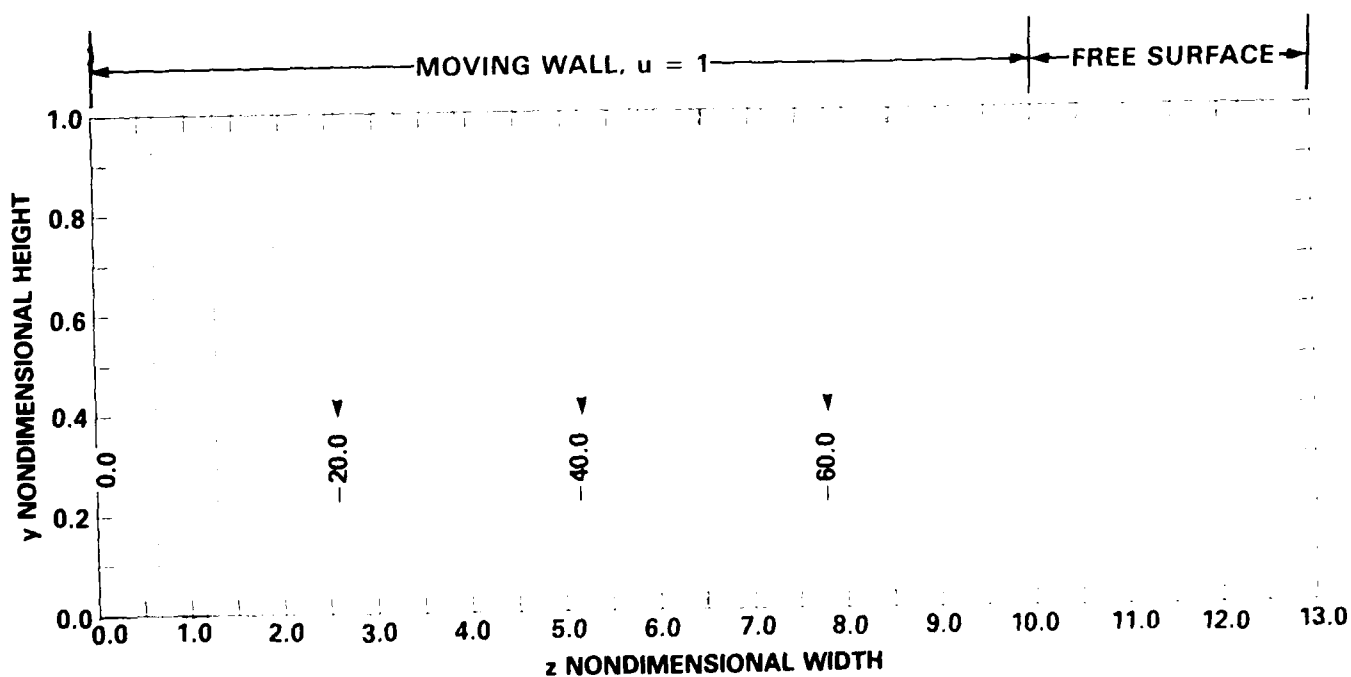Hartmann number $M = 10$ and $h_0 = 80$.

Fig. C-11b. Nondimensional current density stream function contours
$h(y,z)$ for Hartmann number $M = 10$ and $h_0 = 80$.

Fig. C-12a. Nondimensional velocity contours $u(y,z)$ for Hartmann number $M = 10$ and $h_0 = 100$.

Fig. C-12b. Nondimensional current density stream function contours $h(y,z)$ for Hartmann number $M = 10$ and $h_0 = 100$.

Fig. C-13a. Nondimensional velocity contours $u(y,z)$ for
Hartmann number $M = 2$ and $h_0 = -20$.

Fig. C-13b. Nondimensional current density stream function contours
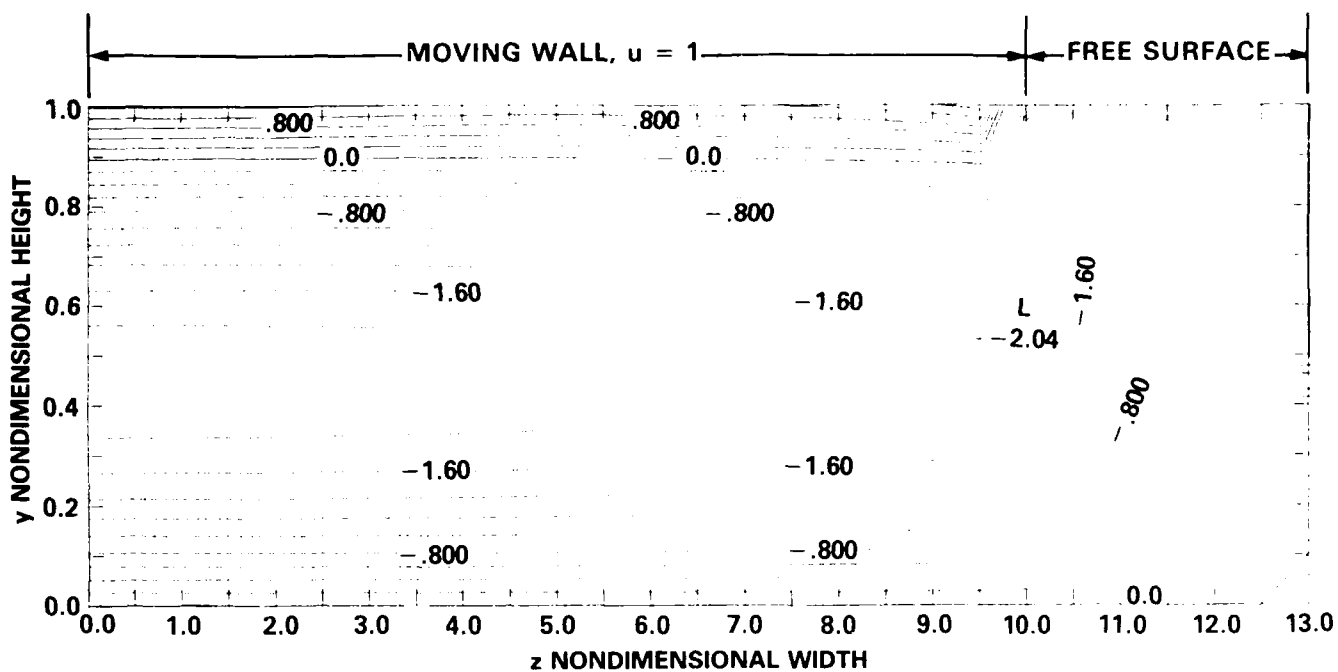$h(y,z)$ for Hartmann number $M = 2$ and $h_0 = -20$.

Fig. C-14a. Nondimensional velocity contours $u(y,z)$ for
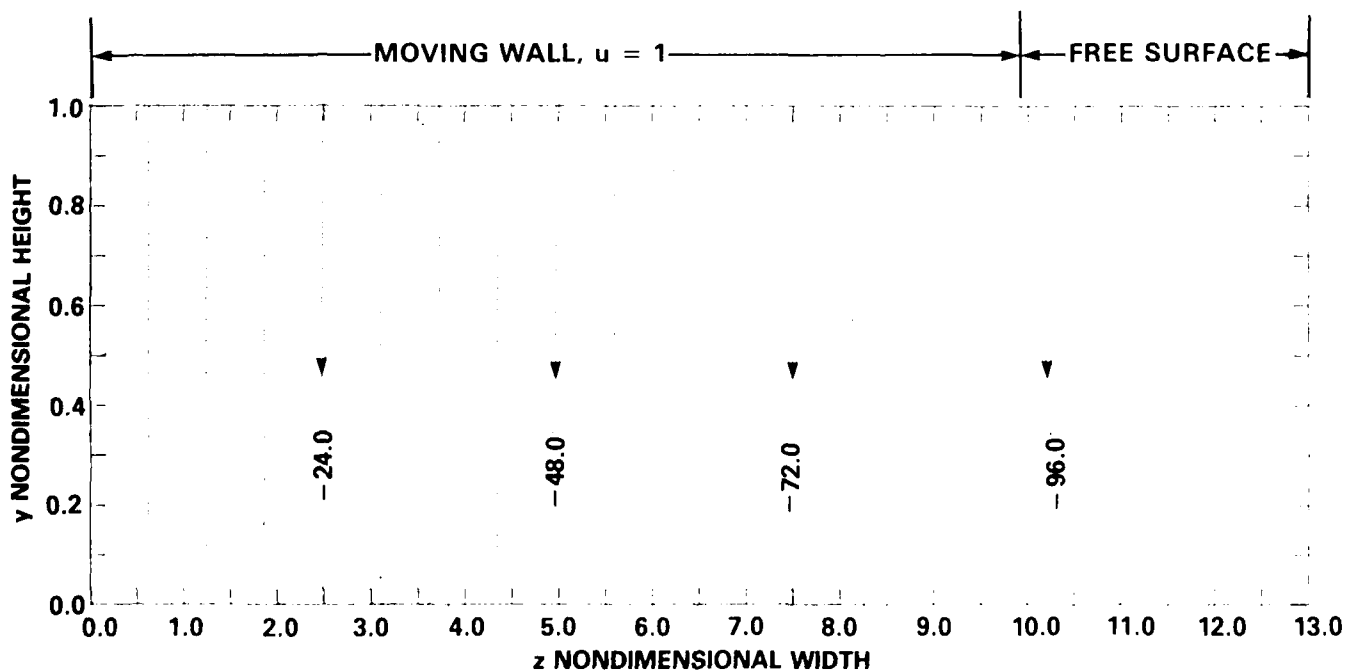Hartmann number $M = 2$ and $h_0 = -40$.

Fig. C-14b. Nondimensional current density stream function contours
$h(y,z)$ for Hartmann number $M = 2$ and $h_0 = -40$.

61

Fig. C-15a. Nondimensional velocity contours $u(y,z)$ for
Hartmann number $M = 2$ and $h_0 = -60$.

Fig. C-15b. Nondimensional current density stream function contours
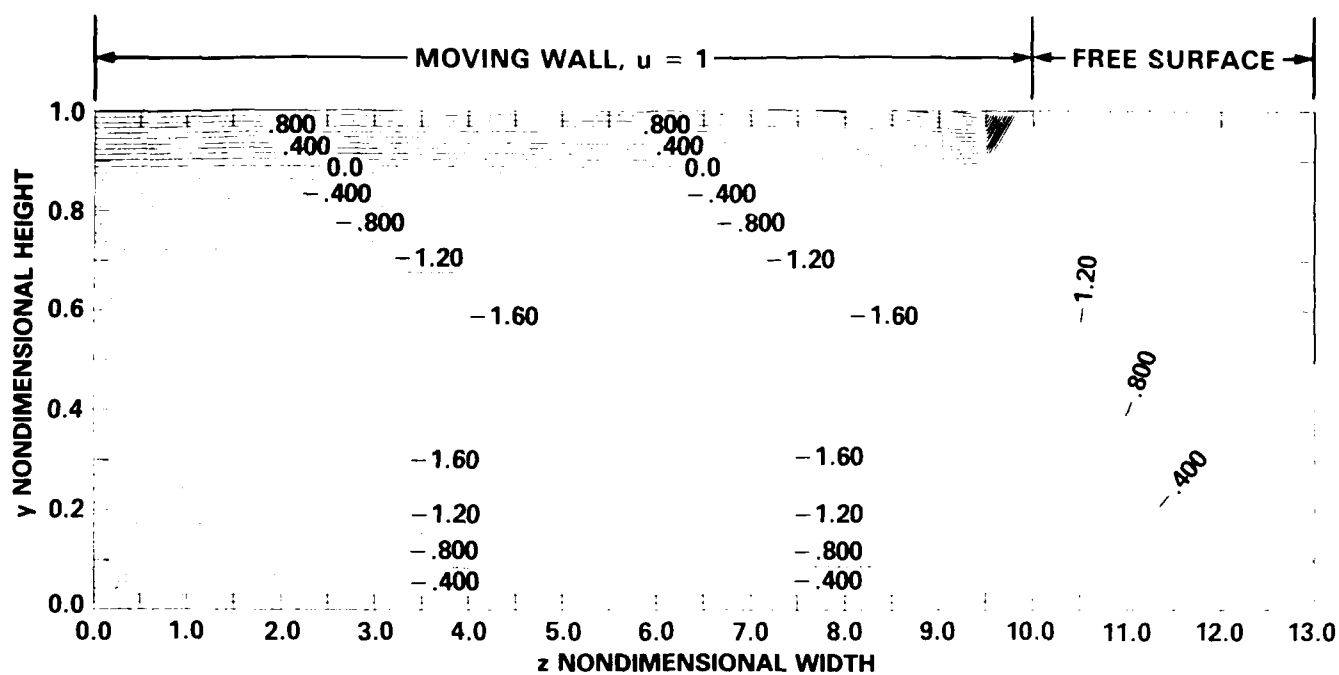$h(y,z)$ for Hartmann number $M = 2$ and $h_0 = -60$.

62

Fig. C-16a. Nondimensional velocity contours $u(y,z)$ for
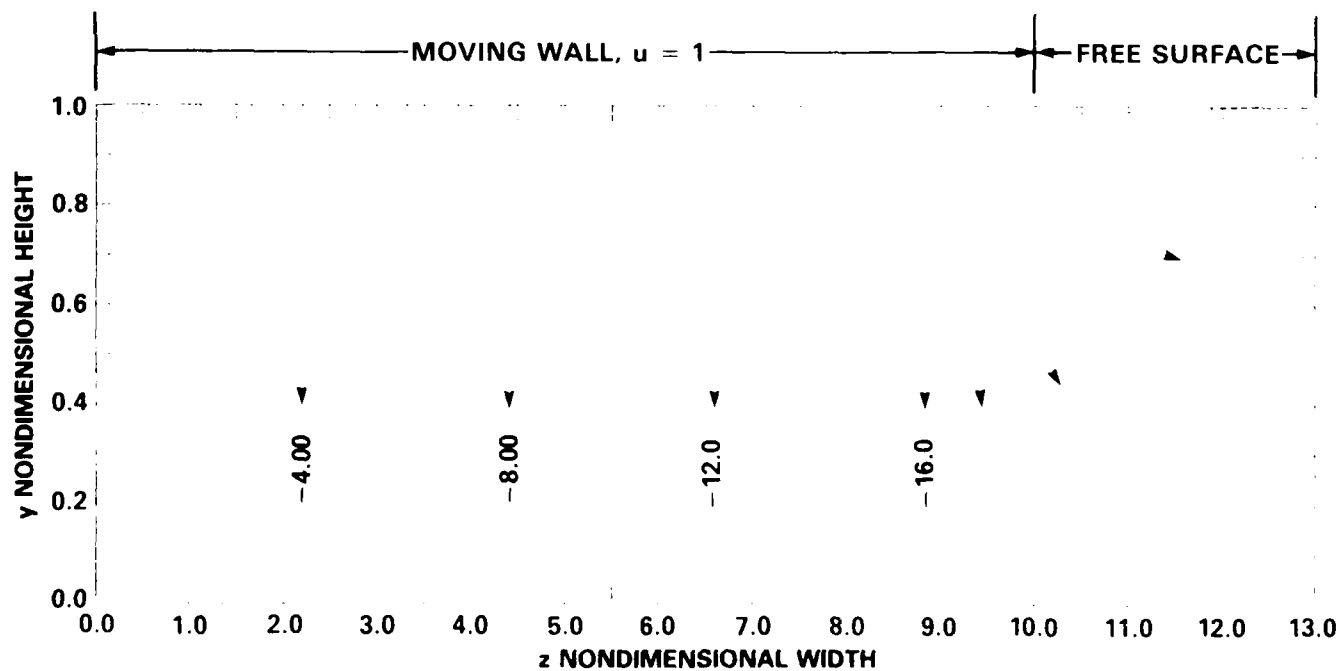Hartmann number $M = 2$ and $h_0 = -80$.

Fig. C-16b. Nondimensional current density stream function contours
$h(y,z)$ for Hartmann number $M = 2$ and $h_0 = -80$.

Fig. C-17a. Nondimensional velocity contours $u(y,z)$ for
Hartmann number $M = 2$ and $h_O = -100$.

Fig. C-17b. Nondimensional current density stream function contours
$h(y,z)$ for Hartmann number $M = 2$ and $h_O = -100$.

Fig. C-18a. Nondimensional velocity contours $u(y,z)$ for
Hartmann number $M = 10$ and $h_0 = -20$.

Fig. C-18b. Nondimensional current density stream function contours
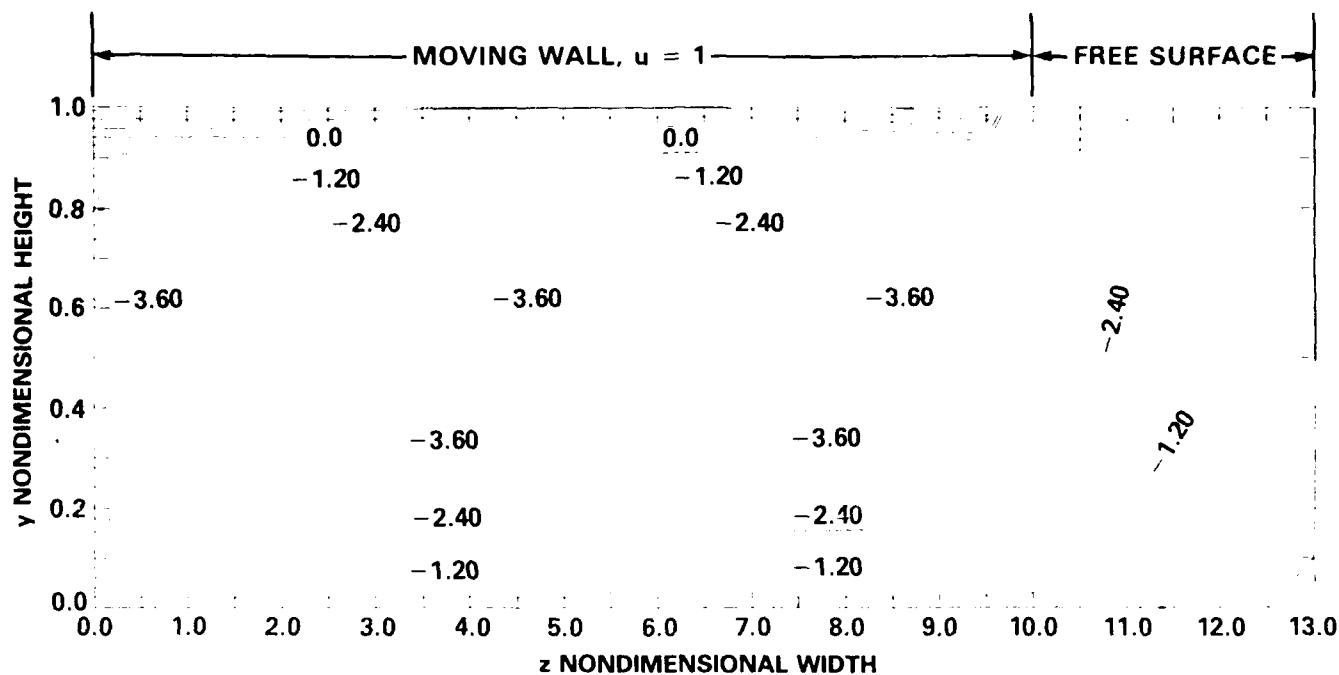$h(y,z)$ for Hartmann number $M = 10$ and $h_0 = -20$.

Fig. C-19a. Nondimensional velocity contours $u(y,z)$ for
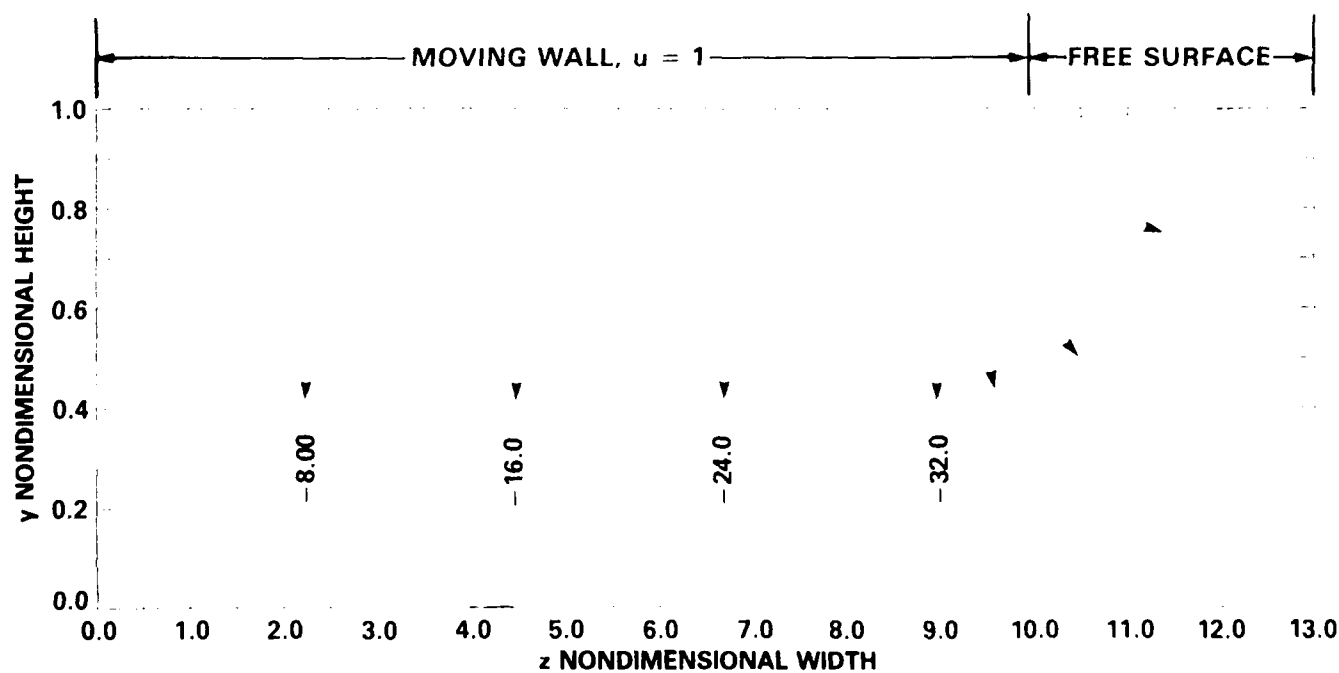Hartmann number $M = 10$ and $h_0 = -40$.

Fig. C-19b. Nondimensional current density stream function contours
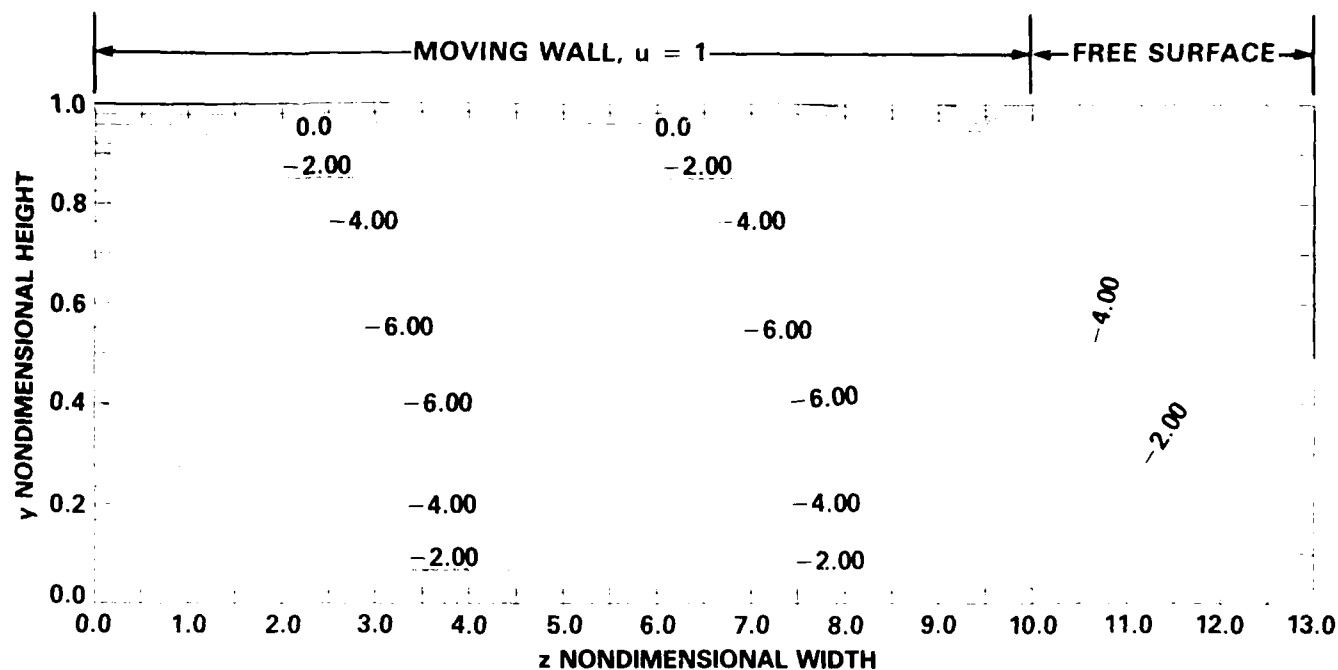$h(y,z)$ for Hartmann number $M = 10$ and $h_0 = -40$.

Fig. C-20a. Nondimensional velocity contours $u(y,z)$ for Hartmann number $M = 10$ and $h_0 = -60$.
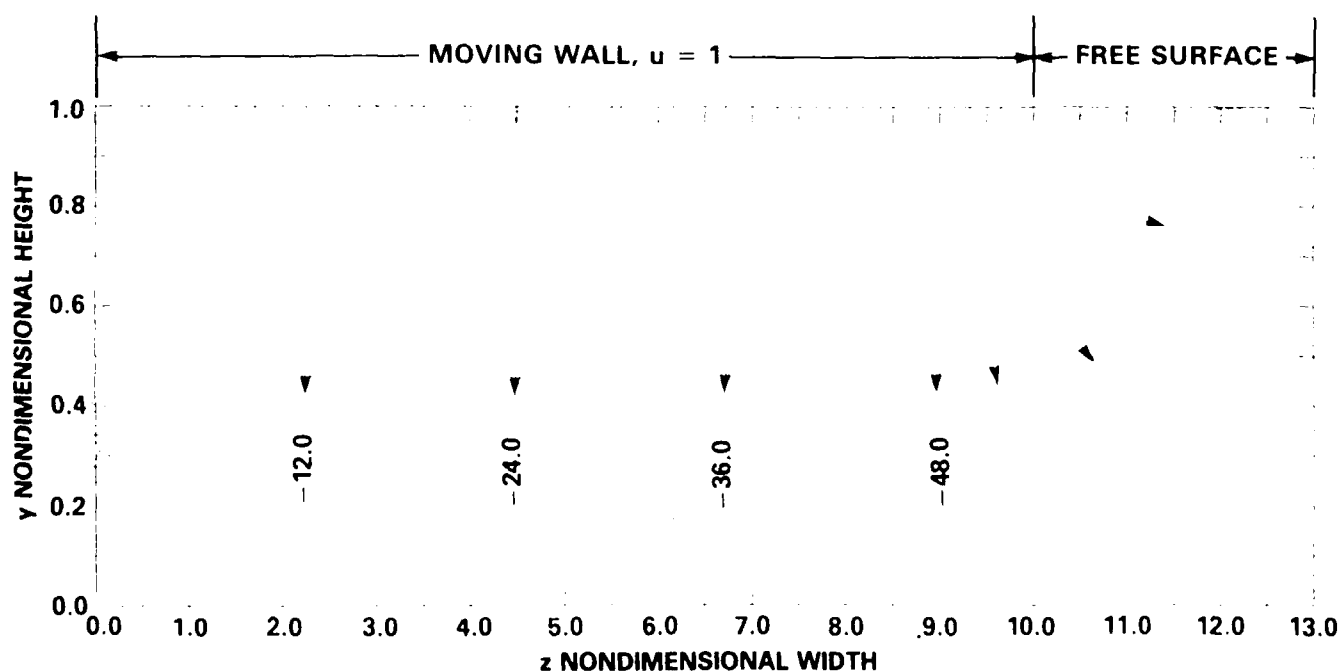

Fig. C-20b. Nondimensional current density stream function contours $h(y,z)$ for Hartmann number $M = 10$ and $h_0 = -60$.

Fig. C-21a. Nondimensional velocity contours $u(y,z)$ for
Hartmann number $M = 10$ and $h_0 = -80$.

Fig. C-21b. Nondimensional current density stream function contours
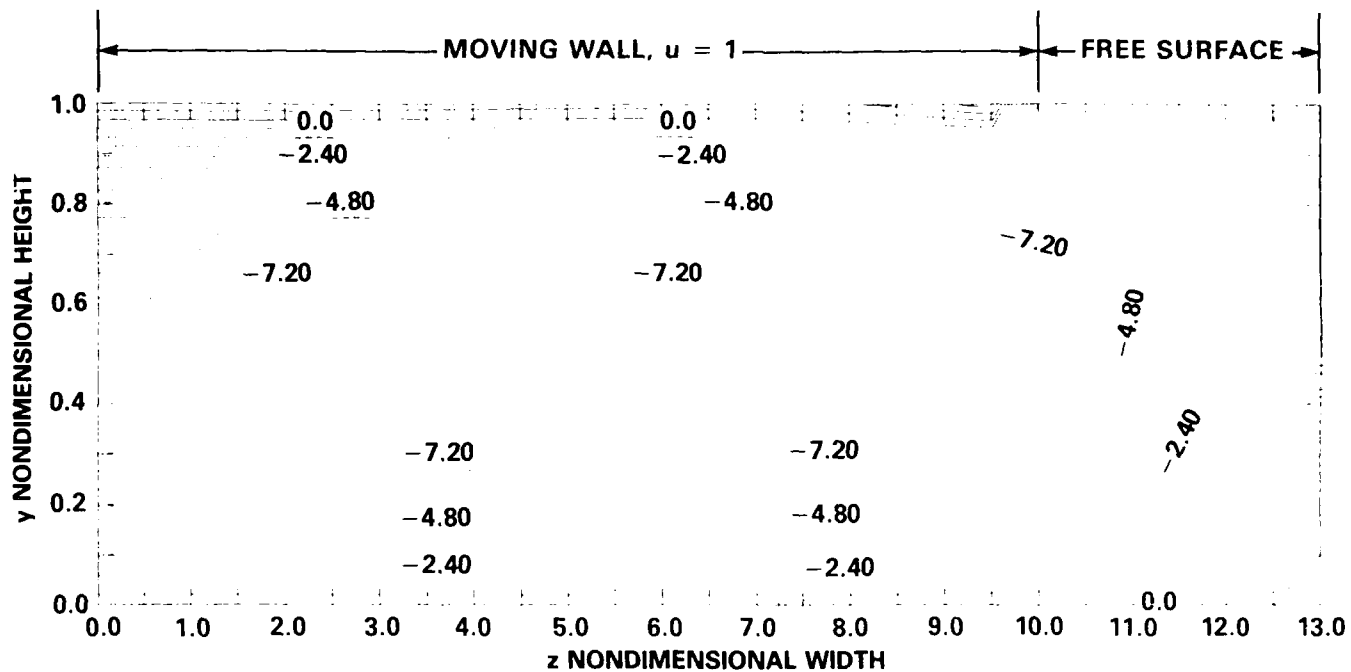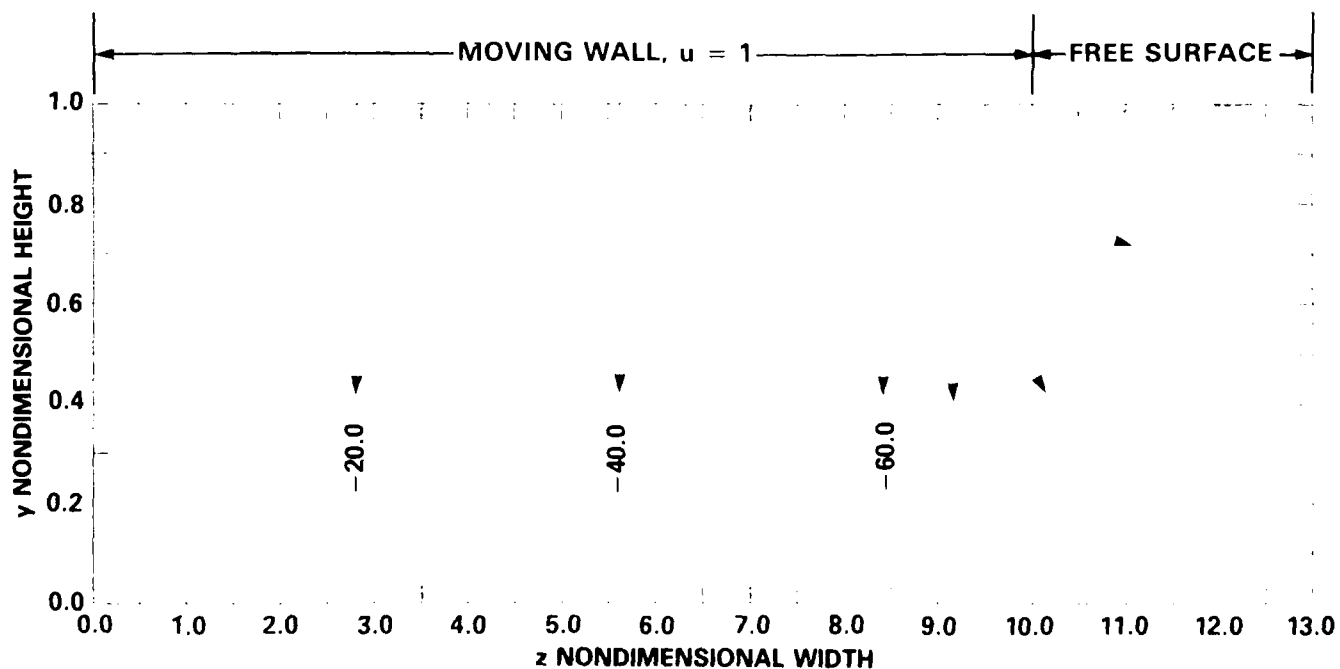$h(y,z)$ for Hartmann number $M = 10$ and $h_0 = -80$.
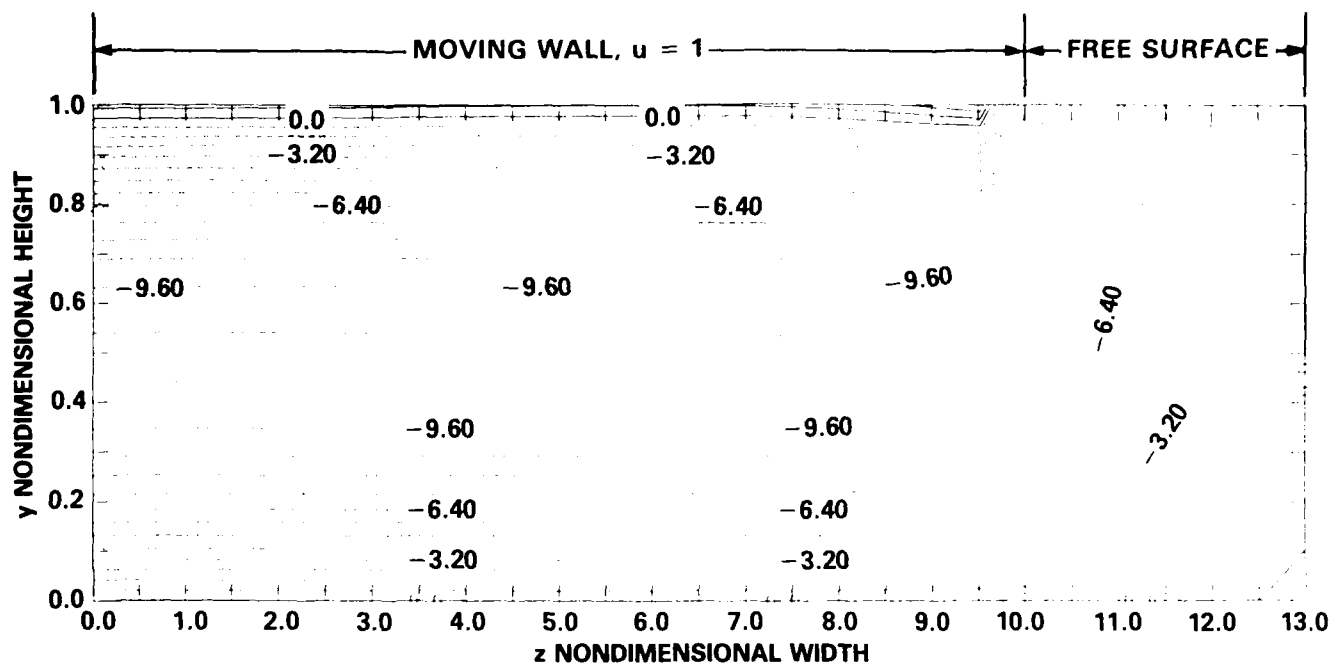
Fig. C-22a. Nondimensional velocity contours $u(y,z)$ for
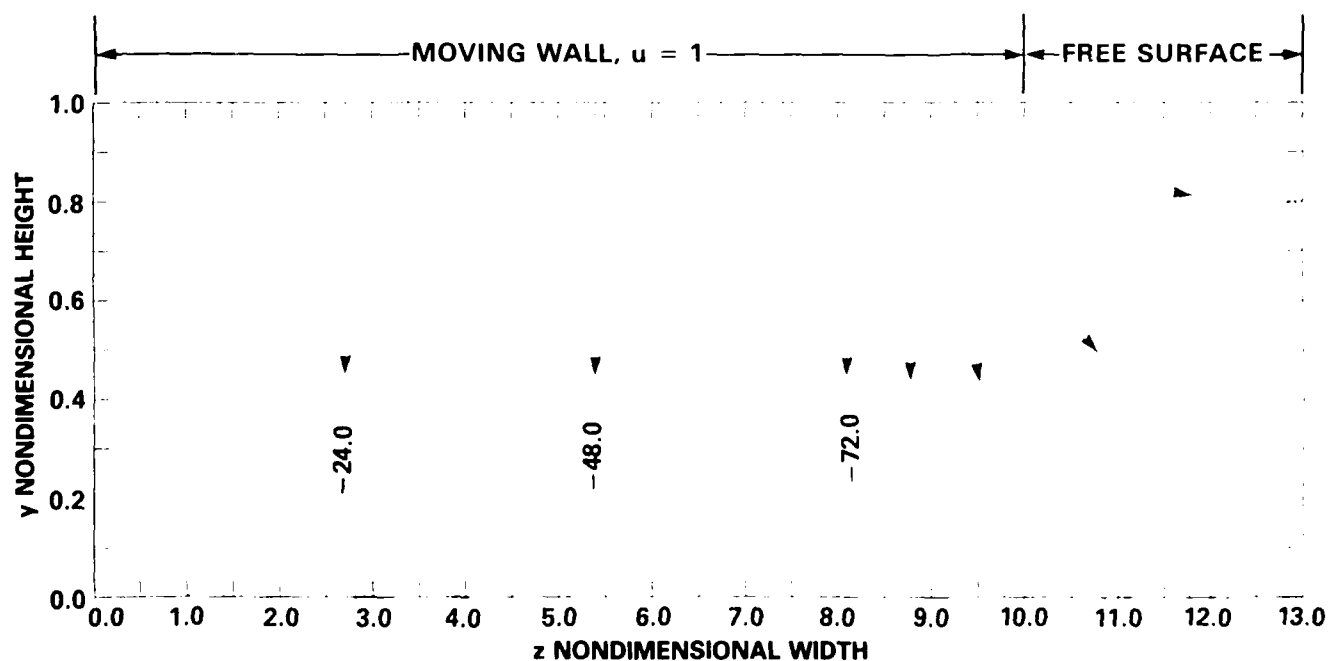Hartmann number $M = 10$ and $h_O = -100$.

Fig. C-22b. Nondimensional current density stream function contours
$h(y,z)$ for Hartmann number $M = 10$ and $h_O = -100$.

REFERENCES

1   H.O. Stevens, M.J. Superczynski, T.J. Doyle, J.H. Harrison, and H. Messinger, *IEEE Trans. Mag*, Vol. 13, p. 269 (1977).

2   T.J. Doyle, J.H. Harrison, and A. Chaikin, *in:* Star Symposium, Soc. Naval Architects and Marine Engineering Spring Meeting, New London, CT, 26-29 April 1978, *Society of Naval Architects and Marine Engineers*, New York, paper 20, pp. 1-7 (1978).

3   J.T. Eriksson, *Acta. Polytech. Scand. Electr. Eng.*, Ser. 48, 1 (1982)

4. H.O. Stevens and M.J. Cannell, David Taylor Naval Ship Research and Development Center, Bethesda, MD. Report DTNSRDC/PAS-81/14 (Oct. 1981).

5   R.L. Rhodenizer, Final Report, Task 4 and 5, General Electric Co., Contract no. N00024-68-C-5415, pp. 7-35 (30 Sept. 1971).

6   J.L. Johnson, G.T. Hummert, and A.R. Keeton, *IEEE Trans. Power Appar. Syst.* PAS-95, 1234 (1976).

7   G.S.S. Ludford and S. Walker, *in: MHD Flow and Turbulance II*, edited by M. Branover and Q.A. Yabhot , Israel Universities, Jerusalem, Israel, pp. 83-95 (1980).

8   H. Branover, *Magnetodydrodynamic Flows in Ducts*, Wiley, New York (1978).

9   J.C.R. Hunt and J.A. Shercliff, *Ann. Rev. Fluid. Mech.*, Vol. 3, p. 37 (1971).

10 W.F. Hughes and F.J. Young, *The Electromagnetodynamics of Fluids*, Wiley, New York (1966).

11 J.T. Woo, J.F. Pipkins, S.H. Brown, N.A. Sondergaard, J.S. Walker, *J. Appl. Phys.*, Vol. 63, No. 10 (15 May 1988).

12 J.S. Walker, S.H. Brown, N.A. Sondergaard, *J. Appl. Phys.*, Vol. 64, No. 1 (1 July 1988).

13 J.S. Walker, S.H. Brown, N.A. Sondergaard, *J. Appl. Phys.*, Vol. 64, No. 4 (15 Aug. 1988).

14 F.J. Young, S.H. Brown and N. A. Sondergaard, David W. Taylor Naval Ship Research and Development Center, Report DTRC 88/017, May 1988.

15 S.H. Brown, P.J. Reilly, N.A. Sondergaard, *J. Appl. Phys.*, Vol. 62, No. 2 (15 July 1987).

16 L.D. Landau and E.M. Lifshitz, *Fluid Mechanics*, Pergamon, Addison Welsey, Reading, MA (1959)

INITIAL DISTRIBUTION

		CENTER DISTRIBUTION	
Copies		Copies	Code
12	DTIC	10	012.3
1	Dr. Ralph A. Burton	1	2702
	Mr. Gaines Burton		
	Burton Technologies Incorporated	2	271
	4940 B. North Boulevard		
	Raleigh, North Carolina 27606	1	2710
20	Dr. John S. Walker	3	2711
	University of Illinois at		
	Urbana-Champaign	30	2712
	144 Mechanical Engineering Building		
	1206 West Green St.	1	5211 (Knox)
	Urbana, Illinois 61801		
		10	5211 (Rept Control)
20	Dr. Gita Talmage		
	University of Illinois at	1	522.1, TIC (C)
	Urbana-Champaign		
	144 Mechanical Engineering Building	1	522.2, TIC (A)
	206 West Green St.		
	Urbana, Illinois 61801	2	5231
20	Dr. Patricia E. Burt		
	United States Naval Academy		
	Annapolis, Maryland 21402		